UNIVERSITY OF OKLAHOMA

GRADUATE COLLEGE

GALAXY CLUSTERS ACROSS THE ELECTROMAGNETIC SPECTRUM

A DISSERTATION

SUBMITTED TO THE GRADUATE FACULTY

in partial fulfillment of the requirements for the

Degree of

DOCTOR OF PHILOSOPHY

By

RHIANNON GRIFFIN
Norman, Oklahoma
2016

Downloaded from SHAREOK. Persistent Handle URL: https://hdl.handle.net/11244/45408

GALAXY CLUSTERS ACROSS THE ELECTROMAGNETIC SPECTRUM

A DISSERTATION APPROVED FOR THE
DEPARTMENT OF PHYSICS & ASTRONOMY

BY

Dr. Xinyu Dai, Chair

Dr. Edward Baron

Dr. Ronald Kantowski

Dr. Mukremin Kilic

Dr. Trina Hope

© Copyright by RHIANNON GRIFFIN 2016
All Rights Reserved.

To Dad and Debbie, Mom and Brad.

Acknowledgements

Many people have been integral to my success as a graduate student, to whom I am grateful.

First and foremost, to Xinyu, thank you for including me on that first observing run to MDM several years ago, and for teaching me how to code, how to write, how to science. To Chris Kochanek and Todd Thompson, for the collaborations and lessons in technical writing.

To my committee and my department for allowing me the opportunity to achieve this work.

To Erin, Jenna, and all of my peers, for the company on sleepless nights, study parties and shoulders to lean on. To Elizabeth, my roommate for life.

To Ernie, for being there. Always.

To my family: Dad, for love of astronomy. Mom, for passion. Debbie, for nurture. Brad, for companionship. To my siblings, for being there for me, for providing that well needed laugh.

To my cat, Beeblebrox, my faithful, ever-fluffy, study companion.

Table of Contents

List of Tables vii

List of Figures viii

Abstract ix

1 An Overview of Galaxy Clusters 1
- 1.1 Introduction . . . 1
- 1.2 Observations Across the Electromagnetic Spectrum . . . 2
  - 1.2.1 Optical . . . 2
  - 1.2.2 Infrared . . . 6
  - 1.2.3 X-ray . . . 7
  - 1.2.4 Radio . . . 10
  - 1.2.5 Gamma-ray . . . 13
- 1.3 Constraining Cosmological Parameters with the Cluster Mass Function . 15
  - 1.3.1 A Few Definitions . . . 16
  - 1.3.2 A Brief Look into ΛCDM Cosmology . . . 17
  - 1.3.3 The Halo Model . . . 19
  - 1.3.4 Linking Models to Observations . . . 22
  - 1.3.5 Systematic Errors & Biases . . . 23
  - 1.3.6 Constraints on Cosmological Parameters . . . 24

2 The *Swift* AGN and Cluster Survey 28
- 2.1 Introduction . . . 30
- 2.2 *Swift* XRT Observations . . . 35
- 2.3 SDSS Data . . . 55
- 2.4 The Method . . . 55
- 2.5 Special Cases . . . 71
  - 2.5.1 Close Pairs of *Swift* Cluster Candidates . . . 71
  - 2.5.2 Incomplete SDSS Coverage . . . 76
- 2.6 Properties of the SDSS Confirmed *Swift* Clusters . . . 79
  - 2.6.1 Overall Redshift Distribution . . . 79
  - 2.6.2 X-ray Bolometric Luminosities . . . 82
  - 2.6.3 Optical Properties . . . 83
  - 2.6.4 Optical-to-X-ray Correlations . . . 84
  - 2.6.5 The Red Sequence . . . 89
  - 2.6.6 Matching with Other Catalogs . . . 95
- 2.7 Confirmed Clusters Not in Current Catalog . . . 102
- 2.8 Summary & Discussion . . . 104
- 2.9 Acknowledgements . . . 105

3 New Limits On Gamma-Ray Emission From Galaxy Clusters 107
- 3.1 Introduction . . . 107
- 3.2 Analysis . . . 113
- 3.3 Results and Discussion . . . 120
- 3.4 Acknowledgements . . . 127

References **129**

Appendices **140**

A Constraining Gamma-Ray Emission from Luminous Infrared Galaxies **140**

A.1 Introduction 140
A.2 Analysis 142
A.3 Results and Discussion 146
A.4 Acknowledgements 156

List of Tables

1.1 Assumed Values of ΛCDM Parameters 27

2.1 The *Swift* Extended Source Catalog 54
2.2 The *Swift* AGN and Cluster Survey: SDSS Confirmations 64
2.3 $2'$ and $3'$ Regions Confirmed, But Different Redshifts 70
2.4 Close Contamination Cases 73
2.5 Red Sequence Colors 89
2.6 Optical Catalogs vs. Our Catalog 98
2.7 SWXCS Catalog vs. Our Catalog 101
2.8 SDSS Confirmations of Lower Significance SACS Clusters 103

3.1 Galaxy Cluster Sample 117
3.2 Photon Flux Upper Limits From Stacking Analyses of Galaxy Clusters . 124

List of Figures

1.1 Simulation of the Cosmic Web 20
1.2 Cosmological Constraints from Galaxy Clusters 26

2.1 Flux Limit vs. Survey Area for X-ray Selected Surveys 29
2.2 Distribution of *Swift* XRT Fields 36
2.3 SACS Cluster Number Counts 39
2.4 SDSS identification of *Swift* clusters in the GRB060204b field 59
2.5 SDSS identification of *Swift* clusters in the GRB061110a field 60
2.6 BCG-to-X-ray-Center Offsets 65
2.7 Mass vs. BCG-to-X-ray-Center Offset 67
2.8 Example 1 of Nearby Contamination 74
2.9 Example 2 of Nearby Contamination 75
2.10 Plots of Incomplete Source Regions in SDSS 77
2.11 Examples of Incomplete Background Regions in SDSS 78
2.12 Observed Redshift Distribution 81
2.13 X-ray Luminosity vs. Optical Richness 85
2.14 X-ray Luminosity vs. BCG Magnitude 88
2.15 Color Distributions and Color Magnitude Diagrams 90
2.16 Mean Color vs. Redshift 93
2.17 Cluster Mass vs. Redshift 94

3.1 All-sky Gamma-ray Photon Count Map 111
3.2 Final Stacked Image of 78 Galaxy Clusters 112
3.3 Photon Flux Upper Limits vs Stack Size 121
3.4 *Fermi* Flux Upper Limits 125

A.1 All-sky Gamma-ray Photon Count Map 145
A.2 Final Stacked Photon Count Map of *IRAS* Galaxies 148
A.3 Photon Flux Upper Limits vs Stack Size 150
A.4 Gamma-ray Luminosities 155

Abstract

Galaxy clusters are the largest gravitationally bound objects in the Universe. From radio to X-ray, we have observed these objects across the electromagnetic spectrum. Formation theories suggest that clusters even emit gamma-rays via cosmic ray interactions with the hot intracluster gas. In this work, I will present a brief overview of these observationally rich objects and then discuss methods we have developed to observe galaxy clusters in the X-ray, optical and gamma-ray regimes.

First, I will discuss our X-ray-selected catalog: the *Swift* AGN and Cluster Survey. We use *Swift* X-ray Telescope data to locate extended X-ray sources as galaxy cluster candidates. *Swift* GRB observations provide an excellent serendipitous, medium-depth, medium-area survey for both AGN (active galactic nuclei) and galaxy clusters. In this work, I focus on the cluster source determination method as well as the initial optical follow-up of cluster candidates. 203 of the 442 extended sources are located in the SDSS footprint and we confirm 104 to be galaxy clusters. We report their redshifts and other cluster details. Additionally, we find that our catalog agrees well with similar studies in number counts, redshift, scaling relations and observed red sequences.

Furthermore, I discuss our search for the elusive gamma-ray signal from galaxy clusters theorized to be produced via neutral pion decay. Evidence suggests that galaxy clusters are massive reservoirs of relativistic particles known as cosmic rays. Cosmic ray protons interact with intracluster medium protons, resulting in

hadronic debris that includes gamma-rays. Although studies predict that with today's gamma-ray missions we should be able to observe this signal from clusters, as of 2016, it has yet to be discovered. To this end, we develop a method for stacking *Fermi* gamma-ray count maps and use this on a rich sample of 2MASS-selected galaxy clusters. Although we do not observe a significant signal from the final stack, we derive the lowest upper limits to date. We discuss the implications to cosmology and large scale structure formation theories.

We update the *Fermi* stacking method to observe luminous and ultraluminous infrared galaxies (LIRGs and ULIRGs) in the gamma-ray regime. The dense interstellar medium and high star formation rates of these galaxies make them ideal candidates for gamma-ray emission from neutral pion production. In the appendix of this work, I present the details of our updated method and discuss our results. Although, we do not observe a significant signal from the final stack of galaxies, we place constraints that agree well with expectations. Furthermore, we report the first gamma-ray detection of an ULIRG: a 4.3σ signal from Arp 220, the closest ULIRG to Earth. We discuss the implications to galaxy formation and compare our results to similar studies.

Chapter 1

An Overview of Galaxy Clusters

1.1 Introduction

Galaxy clusters are the largest gravitationally bound objects in the Universe, having masses of $\gtrsim 10^{14}\ M_{\odot}$ and volumes of ~ 10 Mpc^3 (assuming a virial radius of 2 Mpc). They trace the large scale structure of the Universe, mapping out the most massive density peaks of dark matter. Furthermore, galaxy clusters are observationally rich as we have observed them for decades in several bandpasses, from optical to X-ray to radio. Cluster observables are used to test formation theories, constrain cosmological parameters and map the large scale structure of the Universe. For these reasons and more, galaxy clusters are fundamental to the study of observational cosmology.

Clusters have three main mass components: dark matter, hot ionized plasma, and of course, the galaxy members themselves (listed in order of descending mass). Fritz Zwicky (1933) was the first to notice that the virial mass, measured using galaxy velocity dispersions, was much greater than the luminous mass of the stars in member galaxies. This implies that galaxy clusters are massive reservoirs of dark matter, typically making up $\sim 83 - 89\%$ of a cluster's total mass (Zwicky, 1933; Gonzalez et al., 2013; Dai et al., 2010). Another $\sim$9 – 13% of a cluster's mass is composed of the hot intracluster medium (ICM), 10^8 K ionized plasma with atomic density $n \sim 10^{-4}$ cm^{-3} (i.e., Kravtsov & Borgani 2012). The remaining

1% of a cluster's mass is comprised of the cluster's galaxies.

Galaxy clusters are observationally rich as they have been observed for decades across multiple wavelengths. They are interesting laboratories to study galaxy evolution and intergalactic interactions. Cluster ICM studies constrain dark matter searches as well as plasma physics. Because clusters are the largest objects in the Universe, their abundance probes the amount of large scale structure that exists and its growth over cosmic time. For these reasons and more, many galaxy cluster catalogs exist, with various methods of measuring mass and redshift, as will be discussed in this chapter. Mass measurements are observed directly (via lensing effects, the hydrostatic equation and galaxy velocity dispersions) or using mass proxies and scaling relations, taking advantage of the underlying physics.

1.2 Observations Across the Electromagnetic Spectrum

One great aspect of galaxy clusters is that they are observationally rich and can be studied throughout the electromagnetic spectrum. Here we will briefly discuss the various ways galaxy clusters are studied, starting with how galaxy clusters were first observed and proceeding in historical order.

1.2.1 Optical

Beginning in the 1950s, George Abell studied photographic plates from the Palomar Sky Survey and found over a thousand galaxy clusters, forming the first major galaxy cluster catalog. His catalog became the go-to catalog and was the foundation for the modern understanding of galaxy clusters (Abell, 1958; Abell

et al., 1989; Voit, 2005). He based the initial catalog on the following criteria (Abell, 1958): richness (number of member galaxies), compactness (defined within 1 Abell radius), redshift, and Galactic latitude (to avoid the Galactic plane).

The initial cluster catalogs were based on galaxy clustering only. Photographic plates were examined by eye to find local over-densities of galaxies that fit the above criteria. This has the major disadvantage of projection effects as galaxy clusters are three-dimensional objects and their galaxy members are projected into the two-dimensional plane of the sky (e.g., Gladders & Yee 2000). Obtaining the redshifts of the galaxies can de-project them, but this can be observationally expensive, particularly for spectroscopic redshifts. Today, galaxies are typically observed in several filters to obtain their colors (magnitude measured in one filter subtracted from another filter's magnitude). From this, astrophysicists determine the photometric redshifts of the galaxies as well as additional identifying information. Compared to field galaxies, galaxies that form in the chaotic cluster environment tend to be early-type ellipticals that are redder due to their lower star formation rates. The presence of the 4000 Å Balmer break, ubiquitous in early-type galaxies, means that cluster galaxies are self-similar in color and thus, group together in color-magnitude space and form a feature known as the red sequence (e.g., Hao et al. 2010; Gladders & Yee 2000; Voit 2005). Also, most galaxy clusters have a massive elliptical (typically a cD galaxy) towards the center of the potential well that is identified as the brightest cluster galaxy (BCG) (e.g., Sarazin 1986). The red sequence and BCG can be used in conjunction with local

galaxy over-densities to optically identify galaxy clusters (e.g., Hao et al. 2010; Gladders & Yee 2005; Koester et al. 2007).

With the modernization of astronomy, the entries of galaxy cluster catalogs have increased significantly, from 2,712 clusters in the original Abell catalog to today's optically selected catalogs of 50,000+ galaxy clusters. Modern astrophysicists design cluster templates based off of galaxy colors and magnitudes measured across several filters. These templates are then fit to the data to locate galaxy clusters and determine their redshifts. Where George Abell checked each photographic plate by eye, today's cluster catalogs are formed by searching digital optical data sets (SDSS for example) for local galaxy over-densities, red sequences and BCGs (e.g., Hao et al. 2010; Gladders & Yee 2005; Griffin et al. 2016). The results of which are statistically large catalogs of optically-selected galaxy clusters. These samples are used to identify, study and refine scaling relations based on distance and mass. Two widely used catalogs are the GMBCG catalog of 50,000+ (Gaussian Mixture Brightest Cluster Galaxy, Hao et al. 2010) and the Wen et al. (2012) catalog of 130,000+.

In Chapter 2, I discuss our optical follow-up of X-ray selected cluster candidates in our catalog: the *Swift* AGN and Cluster Survey (SACS). We develop a cluster determining method and use SDSS data as the optical counterpart. In future works, we will apply this method to our own data that extends to deeper magnitudes (Griffin 2016 - in prep, Bhatiani 2017 - in prep). Furthermore, our data will include the southern sky, reaching beyond the footprint of SDSS. In addition to introducing our optical follow-up method, we discuss optical properties

of the clusters, like richness, the red sequence and the BCG magnitude. We compare the optical and X-ray properties of our catalog in a side-by-side comparison. For example, we report the scaling relation of two cluster mass proxies for our survey: the X-ray luminosity and optical richness and compare to similar studies. These properties are independent mass proxies and probe different components of the cluster (X-ray: gas, optical: galaxies) so it is important to see how they compare as well as place constraints on their relation.

Another way of observing clusters takes advantage of their immense mass. Gravitational lensing is a powerful tool for determining a cluster's mass as it provides a direct measurement of the total cluster mass distribution. Einstein predicted the bending of light around massive objects as a consequence of his theory of relativity (see Weinberg et al. 2013 and references within) and Zwicky (1937) predicted that this effect could be used to measure cluster masses. Today, we observe strong lensing effects from galaxy clusters in the form of arcs and multiple images of background sources. Furthermore, we observe weak lensing effects as galaxy clusters distort and magnify background objects which changes the objects' apparent shape and brightness. These small distortions of background galaxies together is known as shear and the mapping of this effect is one of the methods of measuring the mass of a cluster directly (e.g., Bartelmann & Schneider 2001).

Galaxy cluster masses have been measured using both strong (e.g., Kawamata et al. 2016; Richard et al. 2010) and weak lensing techniques (e.g., Umetsu et al. 2014; Hoekstra 2007). Both techniques can be used in conjunction to better

constrain the cluster mass distribution (e.g., Umetsu et al. 2016; Bradač et al. 2006). Here, I have listed just a few examples of cluster gravitational lensing studies. This is a major field in modern astrophysics and these are just a small representative sample. Lensing is even being used to detect galaxy clusters. For example, Wittman et al. (2006) use shear effects to locate clusters in the Deep Lens Survey. The Sloan Giant Arc Survey uses strong lensing features to locate clusters and obtain mass measurements (Oguri et al., 2012; Hennawi et al., 2008).

Lensing provides an independent mass measurement that is observed directly and can be compared to masses obtained via proxies like the Sunyaev-Zel'dovich flux, X-ray luminosity, gas temperature, and optical richness. However, the mass measured via lensing is the two-dimensional projected mass and to compare to the halo mass function, these masses need to be de-projected by fitting to a density model (e.g., von der Linden et al. 2014; Bartelmann & Schneider 2001). Typically, an NFW (Navarro, Frenk, & White) profile is used with the assumption of spherical symmetry. This can lead to an intrinsic scatter in the mass measurement of $\sim 25\%$ (von der Linden et al., 2014). To better constrain this, more weak lensing studies are needed.

1.2.2 Infrared

Because of the expanding universe, the Balmer break (at 4000 Å) redshifts with increased distance. Thus as the look-back time increases, the red sequence feature shifts from optical to infrared. Initially, infrared data was used to confirm redshifts of X-ray extended sources without optical counterparts (e.g., Stanford

et al. 2002). With the advent of infrared satellites like *Spitzer* and *WISE*, more distant galaxy clusters with redshift $z \gtrsim 1$ have been confirmed.

Similar to the optical techniques discussed above, infrared colors are used to confirm SZ and X-ray-selected galaxy clusters and discover new clusters (e.g., Bleem et al. 2015; Zatloukal et al. 2007; van Breukelen et al. 2006). For example, two new infrared-selected catalogs are the IRAC Shallow Survey (*Spitzer* Infrared Array Camera, Eisenhardt et al. 2008) as well as the Massive and Distant Clusters of *WISE* Survey (MaDCoWS, Brodwin et al. 2015; Stanford et al. 2014).

Confirming galaxy clusters at large redshifts allows us to study clusters at large look-back time, observe their evolution, and test the evolution of scaling relations and luminosity functions. To better improve the cluster mass function and therefore improve constraints on cosmological parameters, well-defined cluster surveys across a variety of redshifts are needed (e.g., Bleem et al. 2015; Eisenhardt et al. 2008; Kravtsov & Borgani 2012). In our catalog discussed in Chapter 2, we use *griz* magnitudes for cluster identification. Although we confirm few red sequences for higher redshift clusters ($z < 0.6$), this is what we expect with the depth limits of SDSS. In our own, deeper observations using the Kitt Peak 4m and CTIO 4m, we use *griz* filters and expect to confirm more $z > 0.6$ targets and observe their red sequences.

1.2.3 X-ray

In December 1970, the *Uhuru* satellite became the first satellite launched specifically to observe X-ray astronomy (Giacconi et al., 1971). Within a year, *Uhuru*

observed X-rays originating from the hot intracluster gas as the Coma Cluster and the Virgo Cluster became the first clusters to be observed. It was immediately clear that the emission was bright (at least 10^{44} ergs s^{-1}) and extended, thus likely not originating from an individual galaxy (Gursky et al., 1971; Kellogg et al., 1971). Early studies showed that the most massive galaxy clusters emitted as bright, extended sources in the X-ray sky with luminosities of $10^{43} - 10^{45}$ erg s^{-1} (e.g., Piccinotti et al. 1982). Later studies showed that this emission extends to lower masses and lower X-ray luminosities. For example the MCXC catalog, a compilation of galaxy clusters with ROSAT exposures, extends to 10^{40} erg s^{-1} (Piffaretti et al., 2011).

The X-ray emission is primarily a result of thermal bremsstrahlung. The ICM gas is highly ionized plasma with temperature $\sim 10^8 K$ and atomic density $n \sim 10^{-4}$ cm^{-3} (e.g., Kravtsov & Borgani 2012). The gas is comprised of non-relativistic protons, nuclei and free electrons. When an ICM electron passes near the potential well of an ICM nucleus, the nucleus causes the less massive electron to alter direction and in so doing, emits an X-ray photon. Since the ICM gas is denser towards the center of the potential well, a relaxed galaxy cluster appears as a diffuse, extended X-ray source which falls off radially (e.g., Kravtsov & Borgani 2012; Sarazin 1986). The gas density is typically modeled using the so-called β-model:

$$\rho(r) = \rho(0)\left[1 + \left(\frac{r}{r_c}\right)^2\right]^{-\frac{3}{2}\beta} \tag{1.1}$$

where r_c is the core radius and β is the index parameter. Typical best-fit values

for r_c and β are $\sim$0.1 h^{-1}Mpc and $\sim 2/3$, respectively (Voit, 2005). This model assumes a relaxed cluster (hydrostatic equilibrium) as well as spherical symmetry to first order. It also assumes that the total matter density profile follows an isothermal distribution where the gas temperature, T_g, is radially independent and that the distribution of massive particles (i.e., galaxies or dark matter) are thermalized and follow a Maxwellian distribution (Sarazin, 1986). As discussed in Chapter 2, we use the β-model to fit the *Swift* extended sources in the SACS source determination process (Dai et al., 2015). We also use the β-model in estimating SACS X-ray luminosities (Griffin et al., 2016).

To date, we have observed thousands of galaxy clusters in the X-ray regime using pencil-thin, deep surveys from *Chandra* and *XMM-Newton* (recent surveys include Barkhouse et al. 2006; Finoguenov et al. 2015; Mehrtens et al. 2012; Finoguenov et al. 2007) as well as wide, shallow surveys using the *ROSAT* All Sky Survey (RASS, Voges et al. 1999). Surveys from RASS include NORAS, 400SD, REFLEX (Böhringer et al., 2000; Burenin et al., 2007; Guzzo et al., 2009). Figure 2.1 (Fig. 1 from Dai et al. 2015) shows the flux limit versus survey area for various surveys, including our study, SACS, which fills the gap as a medium depth, medium area survey that uses serendipitous data from the *Swift* X-ray Telescope. In Chapter 2, I discuss in detail our source determination method, the optical follow-up, comparisons to the literature and impact to cosmology.

1.2.4 Radio

There are two primary ways of observing galaxy clusters in the radio: the Sunyaev-Zel'dovich (SZ) effect and synchrotron radiation features. We will discuss both here, though the second one is more relevant to this work. The SZ effect was first proposed and observed by Sunyaev and Zel'dovich in the 1970s (Sunyaev & Zeldovich, 1972, 1970). It is observed as a spectral distortion along the line of sight of the cluster that occurs due to cosmic microwave background (CMB) photons interacting with the cluster ICM. The lower energy CMB photon absorbs energy from the hot plasma electrons (inverse Compton scattering) (e.g., Carlstrom et al. 2000; Sunyaev & Zeldovich 1970). In the Rayleigh-Jeans (RJ) limit, the spectral distortion is given by (Eq. 1 of Carlstrom et al. (2000))

$$\frac{\Delta T}{T_{CMB}} = -2 \int \frac{kT_e}{m_e c^2} \sigma_T n_e dl \tag{1.2}$$

where T_{CMB} is the radiation temperature of the CMB, T_e, m_e, and n_e is the electron temperature, mass and density, respectively, σ_T is the Thompson cross section, and k and c are the Boltzmann constant and speed of light, respectively. The integral is along the line of sight (dl). From this equation, it is clear that ΔT, the brightness of the SZ effect, is independent of redshift. Thus with this technique and sufficient angular resolution, large cluster samples with a wide redshift range are possible (Carlstrom et al., 2002). Because the SZ distortion is small and the signal is faint, today's instruments are the first to use the SZ

effect to obtain SZ-selected surveys. These instruments include *Planck*, the South Pole Telescope, and the Atacama Cosmology Telescope (Planck Collaboration et al., 2014a; Reichardt et al., 2013a; Hasselfield et al., 2013). With advances in technology, current and future instruments should probe clusters in the high redshift range, $z \sim 1-2$. Both SZ and X-ray observations probe the intracluster gas, and from comparing observables from both, we obtain important scaling relations to constrain the cluster mass function. Thus, the observed SZ flux, Y, is an important mass proxy. Current SZ samples are used to calibrate and improve this relation (i.e., Reichardt et al. 2013a).

Thus far this section we have discussed observations from the thermalized particles in the ICM plasma. We also observe non-thermal effects from synchrotron radiation that imply that some galaxy clusters house a population of relativistic particles and large-scale magnetic fields (e.g., Feretti et al. 2012 and others). Relativistic particles, specifically cosmic ray (CR) electrons and positrons, spiral around the cluster's magnetic field lines, causing a diffuse, extended radio emission in the form of relics, arcs and halos. The Coma Cluster was the first such radio, diffuse emission detected (Large et al. 1959). As of 2012, 80 galaxy clusters had been observed with diffuse radio features (Feretti et al., 2012). The emission varies: it can be found in merging and relaxed clusters, range in size from 100 kpc to > 1 Mpc, and vary in location in the cluster, whether it be in the center or periphery or somewhere in between.

Typically, cluster diffuse, radio emission is characterized into three categories: halos, relics and mini-halos. Radio halos are Megaparsec features located at

the center of merging clusters (as evidenced by X-ray and optical observations) (e.g., Feretti et al. 2012; Enßlin et al. 2011) . Radio relics are Megaparsec scale features on the periphery of merging/perturbed clusters, are typically highly polarized and are associated with shock fronts that are triggered by merger activity . Shocks can also be observed via sharp temperature gradients measured from X-ray observations (e.g., Vazza & Brüggen 2014; Hoeft & Brüggen 2007; Enßlin et al. 2011). Radio mini-halos are found in the cool cores of relaxed cool-core clusters (e.g., Feretti et al. 2012; Enßlin et al. 2011; Gitti et al. 2004), are smaller than the other features, up to $\sim$ 500 kpc, and surround a dominant radio galaxy.

Current formation theories state that galaxy clusters formed via the hierarchical merging of smaller systems. During the merging process, shocks form in the ICM and these shocks accelerate particles to relativistic speeds (e.g., Kravtsov & Borgani 2012; Vazza & Brüggen 2014). Studying this emission constrains cluster formation and evolution theories since non-thermal emission observed from clusters is associated with shocks from merger and accretion events. Merger activity continues today and can be observed in the X-ray and optical via substructure and temperature gradients in nearby clusters (Feretti et al., 2012).

Diffusive shock acceleration (DSA; Kang & Ryu 2013) is the leading theory on how cluster particles accelerate to relativistic speeds, resulting in synchrotron radiation and diffuse radio emission. Although DSA is expected to dominate the emission, there are secondary acceleration methods. For example, galaxies interacting with the cluster ICM can introduce CR electrons. These interactions include AGN activity as well as wind stripping (Enßlin et al., 2011). Also,

turbulence from massive merger events can re-accelerate electrons in the ICM (Cassano et al. 2007 and references within). Finally, CR electrons are produced from hadronic interactions, i.e. CR protons interacting with ICM protons.

This radio emission is important to this work as the same mechanisms that accelerate CR electrons should accelerate protons as well. Furthermore, CR protons have a much longer cooling time than CR electrons as CR electrons lose energy not only from synchrotron radiation but non-thermal bremsstrahlung and Inverse Compton interactions. CR protons have a long cooling time, on the order of 10^{10} years, and should stay within the cluster potential well (e.g., Kravtsov & Borgani 2012; Berrington & Dermer 2003; Enßlin et al. 2011). These CR protons interact with the ICM protons and with enough energy, result in particle showers. These so-called p-p interactions produce neutral and charged pions (π^0, π^+, π^-), which result in gamma-rays. In Chapter 3, we discuss our search for this elusive gamma-ray emission from galaxy clusters.

1.2.5 Gamma-ray

As discussed above, there is evidence that galaxy clusters house a population of CR protons that interact with ICM protons. When these so-called p-p interactions occur, one of the bi-products is neutral pions, which immediately decay into two gamma-rays ($\pi^0 \rightarrow 2\gamma$) with a probability of 0.98798 (Brunetti & Jones, 2014; Amsler et al., 2008). Thus we should observe galaxy clusters in the highest of energies!

This neutral pion decay should be the primary source for gamma-ray emission

in galaxy clusters. It would appear as faint, diffuse gamma-ray emission and should be observable with today's gamma-ray missions. Several searches have been conducted, the most recent of which use data from the *Fermi* Gamma-Ray Space Telescope, although there has been no significant detection of this neutral pion emission (Vazza et al., 2016; Ackermann et al., 2014; Griffin et al., 2014; Prokhorov & Churazov, 2014; Zandanel & Ando, 2014; Huber et al., 2013). Point-like gamma-ray observations have been observed in the centers of the Virgo and Perseus clusters, but this is more likely from the radio galaxies located in the clusters, not neutral pion decay (Abdo et al., 2009b,a).

Other expected contributions to the gamma-ray emission are from CR electrons: relativistic bremsstrahlung and Inverse Compton scattering (e.g., Brunetti & Jones 2014; Jeltema et al. 2009). Furthermore, other bi-products of p-p interactions are charged pions, which have the following decay channel:

$$\pi^{\pm} \rightarrow \mu^{\pm} + \frac{\nu_{\mu}}{\bar{\nu_{\mu}}} \rightarrow e^{\pm} + \frac{\nu_{e}}{\bar{\nu_{e}}} + \nu_{\mu} + \nu_{\mu} \tag{1.3}$$

producing secondary electrons and neutrinos (Amsler et al., 2008; Pfrommer et al., 2007). These electrons can produce gamma-rays as well, however the gamma-ray emission should be dominated by neutral pion decay contributions (e.g., Pfrommer et al. 2007).

In Chapter 3, I present our own independent stacking analysis of rich 2MASS galaxy clusters. We use *Fermi* photon count maps to derive upper limits on the gamma-ray emission (Griffin et al., 2014). I discuss our stacking method in detail,

compare to other analyses, and discuss implications to cluster formation theories.

1.3 Constraining Cosmological Parameters with the Cluster Mass Function

Galaxy clusters are great cosmological laboratories for studying the formation of the Universe. They are tracers of large scale structure and catalogs of galaxy clusters provide masses and redshifts of the highest density peaks in the Universe. Because of this, cluster observables can test cosmological theories and constrain cosmological parameters, providing us with a map of what our Universe looks like and how it formed (e.g., Allen et al. 2011).

In Chapter 2, I discuss our catalog, the *Swift* AGN and Cluster Survey, in detail. Catalogs of galaxy clusters are fundamental to the study of cosmology and LSS formation. Cosmological parameters can be constrained from galaxy cluster observables, independent of other measurements (i.e., CMB, type Ia supernovae, baryon acoustic oscillations - BAO). These parameters are the power spectrum normalization (related to σ_8), the matter content of the Universe (Ω_m), and the dark energy equation of state (w) (e.g., Mantz et al. 2010; Tinker et al. 2008). In this section, I will describe one method of obtaining constraints on these parameters.

1.3.1 A Few Definitions

Before delving in to how galaxy clusters can constrain cosmological parameters, I will define some terms that will arise in the following discussion. Observations show us that the Universe is expanding at an accelerated rate (e.g., Voit 2005). Thus cosmic distances between objects change over time so in cosmology, there are two ways to think about distances. The coordinate distance, also known as the proper distance, is the distance between two objects at a certain time, t. The comoving distance (coordinate) takes into account the expansion of the Universe and is thus constant in time (e.g., Melia 2012; Voit 2005). It is useful to define the coordinate distance (the proper distance) in terms of the comoving coordinate (d_0) and the scale factor

$$d(t) = a(t)d_0 \tag{1.4}$$

where the scale factor $a(t)$ describes the relative expansion rate at a time t and is dimensionless. By definition, t_0 is the age of the Universe and from the above equation it is clear that $a(t_0) = 1$. The scale factor is related to redshift via $a(t) = 1/(1 + z)$. It is common to think about cosmic time in terms of the scale factor, $a(t)$, or redshift $z(t)$.

The current cosmological model states that the Universe is comprised of $\sim$70% dark energy, $\sim$ 25% dark matter and the remaining is baryonic in nature (Allen et al., 2011). It is dark energy and its negative pressure that is causing the universe to expand at an accelerated rate. Modeling the Universe as a perfect fluid, the dark energy equation of state describes the pressure in terms of its

energy density: $p = w\rho c^2$. Simple dark energy models call for a dark energy equation of state with constant w (e.g., Voit 2005; Allen et al. 2011) and more complicated models include an evolving dark energy of state ($w(a)$). The total energy density of today's universe is defined to be $\Omega \equiv \frac{\rho}{\rho_c} = \Omega_m + \Omega_{rad} + \Omega_\Lambda$, where the energy densities are that of matter, radiation, and dark energy, respectively. Ω_{rad} is negligible in today's universe and Ω_m includes the matter contributions from both baryons and DM (e.g., Allen et al. 2011).

1.3.2 A Brief Look into ΛCDM Cosmology

In the current paradigm, the formation of DM halos is a result of the clumping of cold dark matter, a key component of ΛCDM cosmology where the other component is the dark energy equation of state, Λ (e.g., Allen et al. 2011). In the early universe, the matter distribution was very smooth with initially small density fluctuations described by

$$\delta(\mathbf{x}) = \frac{\rho - \bar{\rho}}{\bar{\rho}} \tag{1.5}$$

where $\bar{\rho}$ describes the comoving background density. In time, these fluctuations grew as gravity caused the matter to coalesce. The variance of the linearly evolved, CDM fluctuations on mass scale M is a key cosmological parameter with the form (Equation 2 from Allen et al. (2011))

$$\sigma^2(M, a) = \int \frac{d^3k}{(2\pi)^3 W^2(kR) P_m(k, a)} \tag{1.6}$$

where W describes the window function of the Fourier transform within a radius R and P_m is the primordial power spectrum that describes fluctuations in the post-recombination matter (includes dark and baryonic matter). This parameter is typically described as σ_8 in observational cosmology studies (for example, see Mantz et al. (2010) and references within) and is found by evaluating Equation 1.6 for today's universe ($a(t_0) = 1$) and on the typical scale $R_8 = 8$ h^{-1} Mpc. σ_8 is known as the matter power spectrum normalization parameter and has a large influence over the growth of fluctuations in models simulating the early universe. To visualize σ_8, consider the mass contained in randomly distributed spheres of radius R_8 in today's universe and compare the masses contained to the mean mass found in R_8. Assuming the distribution of masses is Gaussian in nature, the variance would be σ_8^2.

From Equation 1.6, it is clear that the above variance depends on mass and redshift (recall that $a = 1/(1 + z)$). Simulations and observations probing the number density n of halos in a volume for a given mass range and redshift range are all that is needed to constrain this important cosmological parameter. This is the basic idea behind the importance of the halo mass function, n(M,z). And since galaxy clusters trace the massive DM halos of the Universe, catalogs of galaxy clusters that are both complete and pure constrain the halo mass function and in turn constrain σ_8 (e.g., Tinker et al. 2008; Allen et al. 2011; Voit 2005).

1.3.3 The Halo Model

The LSS of our Universe is organized in a cosmic web on the Megaparsec (Mpc) scale, with filaments and massive overdensities of matter, both baryonic and dark, along with large, basically empty voids (e.g., Cooray & Sheth 2002). This web-like structure formed from initial quantum fluctuations in the early universe. Over time, locally bound regions emerged from the initially slight matter over densities, forming the beginnings of DM halos. The more massive DM halos are traced by galaxy clusters (e.g., Kravtsov & Borgani 2012; Allen et al. 2011). Simulations, like the one shown in Figure 1.1 (Fig. 1 from Cooray & Sheth (2002)), show the LSS that we see today can be produced from an initially smooth matter distribution. The knots in the cosmic web are associated with the DM halos. Complete and pure catalogs of galaxy clusters provide mass and redshift distributions of these massive DM halos to compute the cluster mass function.

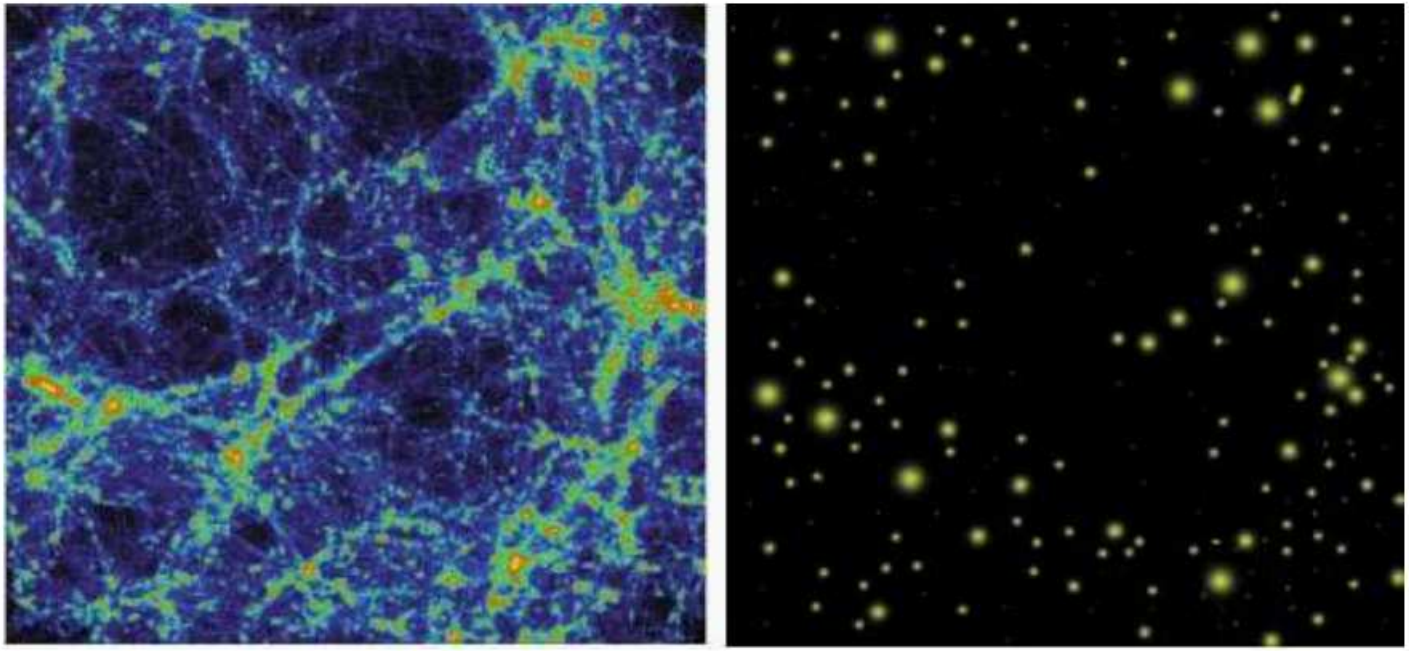


Figure 1.1: Figure 1 from Cooray & Sheth (2002). Left: a simulation of the cosmic web, showing the filaments and matter overdensities that make up the structure of the Universe. Right: a simulation where the complex structure of the cosmic web is replaced by halos representing the matter overdensities.

To see the impact of galaxy clusters on cosmological parameters, we must first discuss the model that we compare cluster observables to in more detail. Instead of modeling the whole cosmic web, we assume to first order that the DM halos are spherical and isolated from their surroundings (Allen et al., 2011). Thus the halo model replaces the complex web structure with a relatively simple distribution of DM halos, described by the halo mass function (defined below), and DM profiles describing the halos themselves. The halo mass function, the distribution of halo masses as a function of redshift, and the halo DM profiles describe the halo model. The right panel of Figure 1.1 shows the DM halo distribution for the LSS web in the left panel of Figure 1.1.

The halo mass function is typically described differentially:

$$\frac{dn}{dlnM} = \frac{\bar{\rho}_m}{M}\frac{dln\sigma}{dlnM}f(\sigma) \tag{1.7}$$

The mass function has units of count per unit comoving volume and $f(\sigma)$ is a fitting function dependent on the model used. A typical mass function for $z \lesssim 2$ is from the work of Tinker et al. (2008), based off of explicit cosmological simulations. They assume a fitting function that is universal to changes across redshift and cosmology and is defined to be

$$f(\sigma) = A\left[\left(\frac{\sigma}{b}\right)^{-a} + 1\right]e^{-c/\sigma^2} \tag{1.8}$$

where A, b, a and c are functions of redshift and contain parameters one can vary

to fit the mass function from N-body simulations to observations (Tinker et al., 2008). In Chapter 2, we compare and discuss our redshift results to the Tinker et al. (2008) halo model to show that our catalog is complete to $z \sim 0.3$ and that we should use deeper *griz* magnitudes to confirm higher redshifts.

1.3.4 Linking Models to Observations

Using the halo model of DM distribution and the associated mass function described above, galaxy clusters contain the observables needed to constrain cosmological parameters. This is important because the main component of the halos, dark matter, is aptly named and is dark, i.e. emits no electromagnetic radiation directly and is neutrally charged. Galaxy clusters are the tracers of the most massive halos and as discussed in the previous section, they have been detected and studied throughout the electromagnetic spectrum and follow certain empirical scaling relations, which are used to determine cluster masses.

The basic idea begins with a cluster survey that is assumed to be both complete and pure as well as contain accurate mass and redshift measurements. Scaling relations and a model of the selection process are used to expand beyond the cluster survey's reach to the full solid angle of the sky, assuming a given redshift range. Certain biases and known systematic errors (described below) are taken into account. Then, the observed data are fit to the halo model, assuming a specified dark energy equation of state (i.e., constant or evolving) and allowing certain cosmological parameters to vary freely. Then, we compare the results to other independent studies and use any overlapping parameter spaces to constrain the

cosmological parameters of interest (e.g., Mantz et al. 2010). This is summarized neatly by the following equation:

$$\bar{N}(M_a, z_i) = \frac{\Delta\Omega}{4\pi} \int_{z_i}^{z_{i+1}} dz \frac{dV}{dz} \int_{lnM_a}^{lnM_{a+1}} dlnM \frac{dn}{dlnM} \tag{1.9}$$

where $\bar{N}(M_a, z_i)$ is the number of expected halos in a given redshift bin $[z_i, z_{i+1}]$ and a given mass bin $[M_a, M_{a+1}]$ covering a solid angle $\Delta\Omega$, and V is the comoving volume. The final integral integrates over the mass function discussed above, $\frac{dn}{dlnM}$ (Allen et al., 2011).

1.3.5 Systematic Errors & Biases

Equation 1.9 assumes a complete and pure catalog of clusters. In reality, observational surveys are neither complete nor pure. To account for this, counting errors are included in the calculation of $\bar{N}(M_a, z_i)$ (Allen et al., 2011). There are a number of issues that arise from using galaxy cluster surveys. First, large cluster catalogs depend on photometric redshifts which can have significant errors. Spectroscopic follow-up observations have been performed and can be included to reduce error, but these are too observationally-intensive to do on larger scales (e.g., Hao et al. 2010). Second, scaling relations used to link cluster observables to cluster mass tend to have a large spread, depending on the relation (i.e., Mass-Temperature is tighter than Mass-X_L which is tighter than Mass-richness - e.g., Voit 2005). Also, scaling relations from X-ray and SZ measurements are tighter than those from optical. Furthermore, there is a bias in any astronomical survey

(the Malmquist bias) that implies that brighter, more massive targets are more likely to be detected. This adds complications when fitting cosmological parameters in Equation 1.9. According to LSS formation theory, there should be faint clusters below the luminosity limits of current catalogs but how many and of what mass depends on the model of the mass function. Projection effects have to be considered as well, particularly for optical surveys where the contamination of foreground and background galaxies can affect richness estimates. X-ray emission from galaxy clusters suffers less from projection effects as the emissivity depends on the number density of electrons squared ($\epsilon \propto n_e^2$).

1.3.6 Constraints on Cosmological Parameters

Using the method discussed above on a catalog of X-ray selected galaxy clusters, Mantz et al. (2010) found the following constraints of cosmological parameters: $\Omega_m = 0.23 \pm 0.04$, $\sigma_8 = 0.82 \pm 0.05$ and -1.01 ± 0.20, assuming a constant w. Their results agree well with other independent measurements of these parameters and combined together yield constraints of $\Omega_m = 0.27 \pm 0.02$, $\sigma_8 = 0.79 \pm 0.03$ and -0.96 ± 0.06. Contours of their results and those of other independent studies are shown in Figure 1.2 (Fig. 1 and 3 from Mantz et al. (2010)). Figure 1.2 shows agreement of their constraints with those found using other cosmological observables. Throughout this work, we assume values for certain cosmological values, like Ω_m, and these are listed in Table 1.1.

Thus catalogs of galaxy clusters with accurate redshift and mass measurements are fundamental to independently constrain these cosmological parame-

ters and better understand the Universe we live in. In Chapter 2, I will discuss SACS, our own galaxy cluster catalog (Dai et al., 2015; Griffin et al., 2016), which contains 104 galaxy clusters with measured masses and redshifts. We used the measured X-ray luminosities to estimate the cluster mass using a scaling relation (Vikhlinin et al., 2009). We found optical confirmations using SDSS galaxy photometric redshifts to calculate the cluster distances.

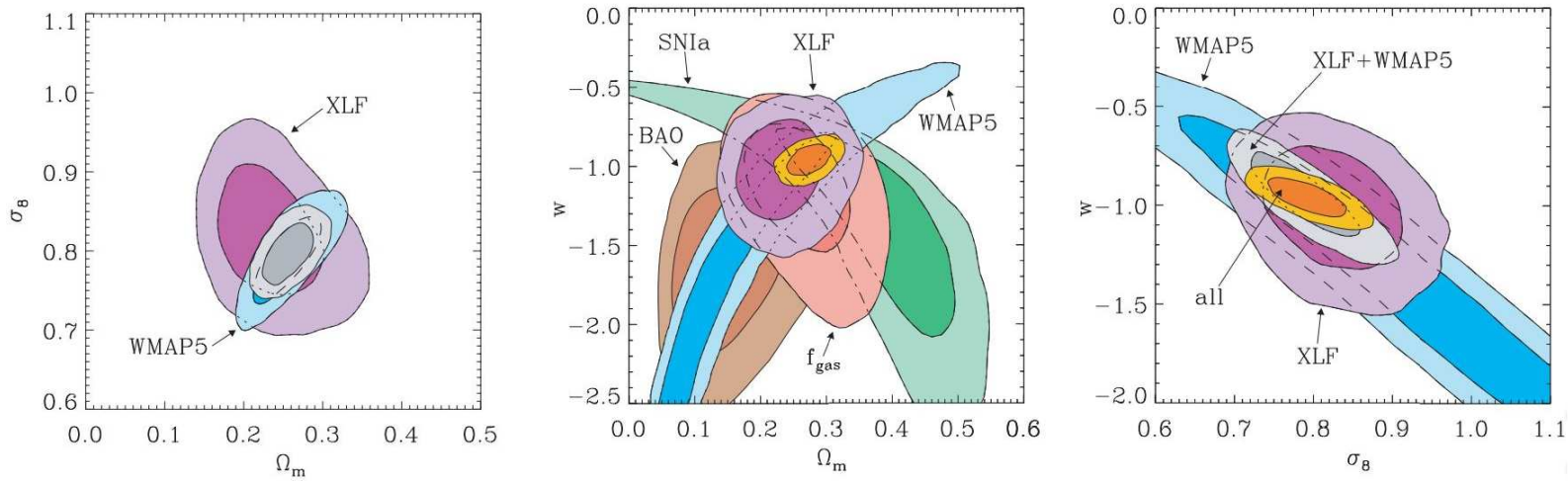


Figure 1.2: Figures 1 & 3 from Mantz et al. (2010). Contour plots indicating parameter space from cosmological constraints from X-ray selected galaxy clusters. The plots show good agreement among the various constraining methods: WMAP, XLF (X-ray Luminosity Function - X-ray selected galaxy cluster sample), Type Ia supernovae, baryon acoustic oscillations, and gas mass fraction of galaxy clusters. See the works of Mantz et al. (2010) for full details.

Variable Name	Full Name	Assumed Value
k	curvature of the Universe	0 (flat)
H_o	Hubble constant	70 km s^{-1} Mpc^{-1}
Ω_m	matter density of the Universe	0.3
Ω_Λ	dark matter density of the Universe	0.7

Table 1.1: These are assume values for certain cosmological parameters used throughout this work (unless otherwise stated).

Chapter 2

The *Swift* AGN and Cluster Survey

The *Swift* AGN and Cluster Survey (SACS) is an X-ray selected catalog of 22,563 point sources and 442 extended sources observed in 125 deg^2 of *Swift* X-ray Telescope (XRT) serendipitous fields. This is a medium depth and area survey that fills the gap between deep, pencil-thin X-ray surveys and shallow, wide field surveys (see Figure 2.1). In this chapter, I will discuss the extended source analysis including detection, number counts and comparison to similar studies. I will then delve into the optical confirmation of the extended X-ray sources using SDSS publicly available data. We find that this catalog agrees well with other studies in number counts, completeness (to $z \lesssim 0.3$), and redshift. This catalog has produced two papers thus far: Dai et al. (2015) and Griffin et al. (2016). Here, I will present the second paper in it's entirety with additional details from the first paper and other relevant sources.

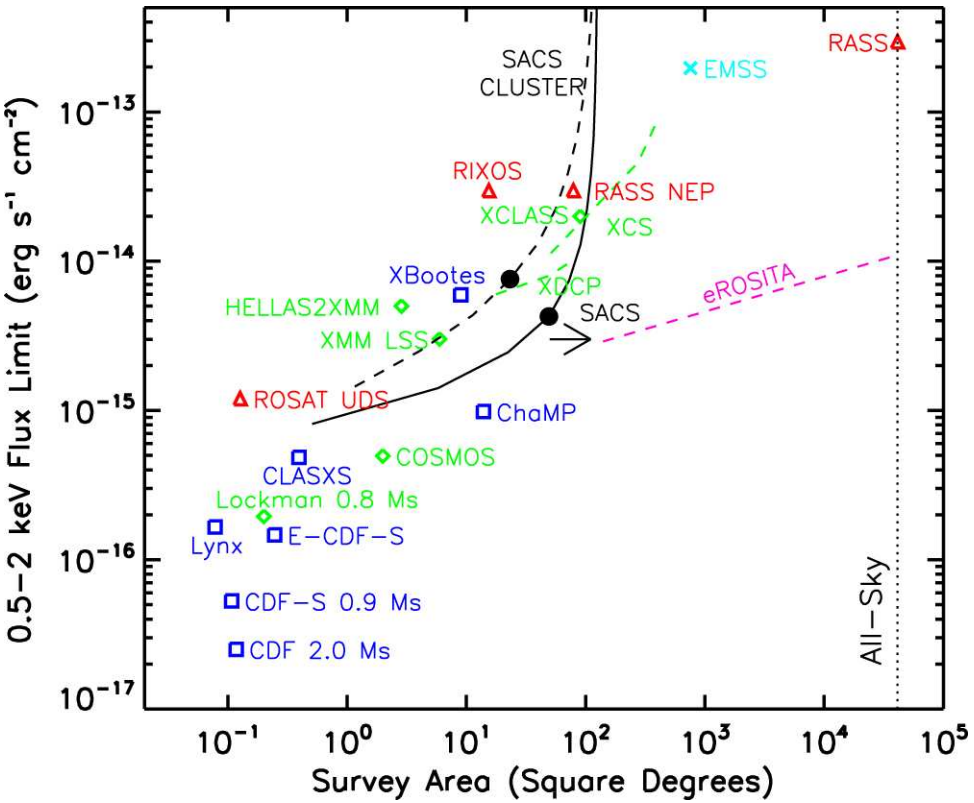


Figure 2.1: Flux limit vs. survey area for various soft X-ray selected surveys. Figure 1 from Dai et al. (2015). Surveys shown are from Brandt & Hasinger (2005), including more recent *XMM-Newton* surveys, as well as future *eROSITA* surveys. This plot indicates that SACS covers more area and achieves deeper exposures than other similar surveys.

2.1 Introduction

Our universe is organized in a cosmic web on megaparsec (Mpc) scales, with filaments, voids and massive over-densities of matter. These most massive peaks in the large scale matter density are traced by galaxy clusters, the largest gravitationally bound structures in the universe (e.g., Bahcall 1988; Kravtsov & Borgani 2012). As discussed in Chapter 1, large samples of clusters together with subsequent mass and redshift estimates, allow us to constrain the cluster mass function and thus place improved constraints on important cosmological parameters such as σ_8, Ω_m, and w (see Allen et al. 2011 for a recent review) as well as studying cluster evolution across cosmic time.

Several methods are employed to discover galaxy clusters. Optical identification produces the largest cluster catalogs by far, and different algorithms focus on different aspects of optical properties, such as spatial galaxy over-densities (e.g., Abell et al. 1989; Gal et al. 2003; Kochanek et al. 2003), the red sequence (e.g., Nilo Castellón et al. 2014; Gladders & Yee 2005; Valentinuzzi et al. 2011), or the brightest cluster galaxy (BCG) (e.g., Koester et al. 2007). Optical identification schemes usually suffer from projection effects created by observing a three-dimensional object in a two-dimensional plane. However, optical surveys play a crucial role in measuring cluster redshifts (e.g. Adami et al., 2011). More recent methods include the Sunyaev-Zel'dovich (SZ) effect and gravitational lensing. The SZ effect is caused by cosmic microwave background (CMB) photons inverse Compton scattering off the high energy electrons of the intracluster medium

(ICM) (e.g., Sunyaev & Zeldovich 1972; Carlstrom et al. 2002). This can be seen as a distortion in the shape of the CMB spectrum and is used to follow-up known clusters as well as for new cluster surveys (e.g., Carlstrom et al. 2002; Planck Collaboration et al. 2011; Marriage et al. 2011; Hasselfield et al. 2013; Planck Collaboration et al. 2014b; Reichardt et al. 2013b). Gravitational lensing provides a direct measure of the mass of a cluster and is observable through the deflection, shearing, and magnification of background sources (e.g., Hoekstra & Jain 2008; Umetsu et al. 2014). Lensing and cosmic shear surveys (e.g., Oguri et al. 2012; Hoekstra 2007; Richard et al. 2010; Oguri et al. 2010; Umetsu et al. 2014) trace the large scale structure (LSS), provide independent cluster mass estimates, map the dark matter within, and place independent constraints with improved calibration on cosmological parameters (e.g. Hoekstra & Jain 2008; Weinberg et al. 2013) and potentially could be a useful detection method in future surveys (e.g., Refregier 2003), as demonstrated by the Deep Lens Survey (Wittman et al., 2006).

Galaxy clusters also appear as extended sources in the X-ray sky. Hot electrons in the ICM interact with protons and atomic nuclei to cause plasma emission in the X-ray regime (e.g., Kravtsov & Borgani 2012). X-ray selected cluster surveys have been performed with many different combinations of survey depth and area, such as NORAS (Northern ROSAT All-Sky Survey, Böhringer et al. 2000), 400SD (400 Square Degree Survey, Burenin et al. 2007), and REFLEX (ROSAT-ESO Flux-Limited X-Ray Survey, Guzzo et al. 2009). These studies and more are

included in the MCXC catalog[1] (Piffaretti et al., 2011), a compilation of X-ray selected galaxy clusters and their characteristics. The MCXC catalog includes catalogs based on publicly available ROSAT All Sky Survey and serendipitous observations. Recent examples of *XMM-Newton* and/or *Chandra* selected cluster and group surveys include the ChaMP (*Chandra* Multiwavelength Project) Serendipitous Galaxy Cluster Survey (Barkhouse et al., 2006), galaxy groups in the Extended *Chandra* Deep Field South (Finoguenov et al., 2015), the *XMM* Cluster Survey (Mehrtens et al., 2012), and the *XMM-Newton* Wide-Field Survey in the COSMOS Field (Finoguenov et al., 2007).

X-ray identification has several advantages over optical. First, X-ray observations of clusters suffer less from the projection effects that limit most optical surveys. Because the X-ray emissivity is proportional to the square of the electron density, it provides good contrast over any background (e.g., Voit 2005). Furthermore, there are several scaling relations based on X-ray data that galaxy clusters are known to follow. For example, the X-ray luminosity versus mass ($L_X - M$) relation is much tighter than the optical richness to mass relation and is a more accurate mass determination method (e.g., Böhringer et al. 2000; Voit 2005). One disadvantage to the X-ray identification of galaxy clusters is that it is difficult to detect high redshift clusters because of the $(1 + z)^{-4}$ dependence of surface brightness on redshift. Thus, shallow X-ray surveys only detect the core region of high redshift clusters, which increasingly resemble point-like sources. Also, low

[1]Meta-Catalog of X-ray detected Clusters of galaxies: `http://heasarc.gsfc.nasa.gov/W3Browse/all/mcxc.html`

redshift galaxies can be extended X-ray sources and may appear as false positives in X-ray cluster surveys (e.g., Adami et al. 2011). Unfortunately, it is also difficult to get accurate measurements of redshifts from X-ray data alone.

Therefore using X-ray and optical data in a combined program, like the one presented in this paper, is ideal for determining cluster characteristics. Since the mass of a galaxy cluster is dominated by dark matter, their total masses are difficult to measure directly. Thus, mass estimates are obtained by correlating cluster mass with easily observable quantities that include X-ray luminosity, richness (number of member galaxies), temperature and velocity dispersions (e.g., Voit 2005; Lopes et al. 2006). Proving good correlations between independent mass estimates and further constraining them is imperative so that reliable measurements of the cluster mass function can be obtained. This allows us to investigate its evolution in time and thus better study the formation and evolution of structures and improve constraints on cosmological parameters (e.g., Kravtsov & Borgani 2012; Lopes et al. 2006). For example, in this combined program we correlate the X-ray bolometric luminosity and the optical richness (N_{opt}), comparing our results with other studies (see Section 2.6.4).

The *Swift* gamma-ray burst (GRB) fields provide 125 deg^2 of serendipitous soft X-ray observations. Several other groups are working with this dataset but with different focuses than this study (Tundo et al., 2012; Puccetti et al., 2011; D'Elia et al., 2013; Evans et al., 2014; Liu et al., 2015), and we made comparisons to most of these works in Dai et al. (2015). In this paper, we compare our results to the more recent *Swift* XRT Cluster Survey (SWXCS) (Liu et al., 2015). In

Dai et al. (2015), we detected 442 extended sources in these GRB fields. Details are listed in Table 4 of Dai et al. (2015) and also is reported here in Table 2.1

Of these 442, 209 lie in the footprint of the SDSS DR8 (Aihara et al., 2011). We can use this SDSS data to look for over-densities in the photometric redshift distribution of the galaxies near the X-ray source. Using the galaxy over-density detection method described in this paper, we confirm 104 of these candidates as galaxy clusters. Our own optical observational data, extending to deeper magnitudes, will be presented in future works. The structure of this paper is as follows. Sections 2.2 and 2.3 introduce the *Swift* and SDSS data, respectively. Section 2.4 describes the method employed to detect clusters. Special cases are discussed in detail in Section 2.5. We discuss the properties of the cluster candidates with confirmed SDSS galaxy over-densities in Section 2.6, including the overall redshift distribution (§ 2.6.1), a comparison of the X-ray luminosity to the optical properties (§ 2.6.2 – 2.6.4), and the red sequence feature common amongst galaxy clusters (§ 2.6.5). We also compare our results to the literature. In Section 2.6.6, we match our catalog to other cluster surveys with large footprints on the sky. We briefly discuss cases found in a previous iteration of our X-ray source selection algorithm that are not in our current catalog (§ 2.7). In Section 2.8, we conclude with a summary and discussion of our results. We assume a cosmological model with $H_0 = 70$ kms^{-1}Mpc^{-1}, $\Omega_M = 0.3$, and $\Omega_\Lambda = 0.7$.

2.2 *Swift* XRT Observations

The *Swift* Gamma-Ray Burst Mission was launched in 2004 with three onboard instruments: the Burst Alert Telescope, the X-ray Telescope, and the Ultraviolet/Optical Telescope. As it's name suggests, the main purpose of *Swift* is to observe GRBs and their afterglows through multiple instruments to obtain multiwavelength data simultaneously (Gehrels et al., 2004). GRBs are observed all over the sky and are not known to be correlated with other X-ray sources. Therefore there should not be a selection bias when considering this dataset for galaxy clusters and these XRT fields constitute serendipitous observations for an X-ray selected galaxy cluster survey. Figure 2.2 shows the all-sky distribution and relative exposure depth of the XRT fields used in this study (Fig. 2 from Dai et al. (2015)).

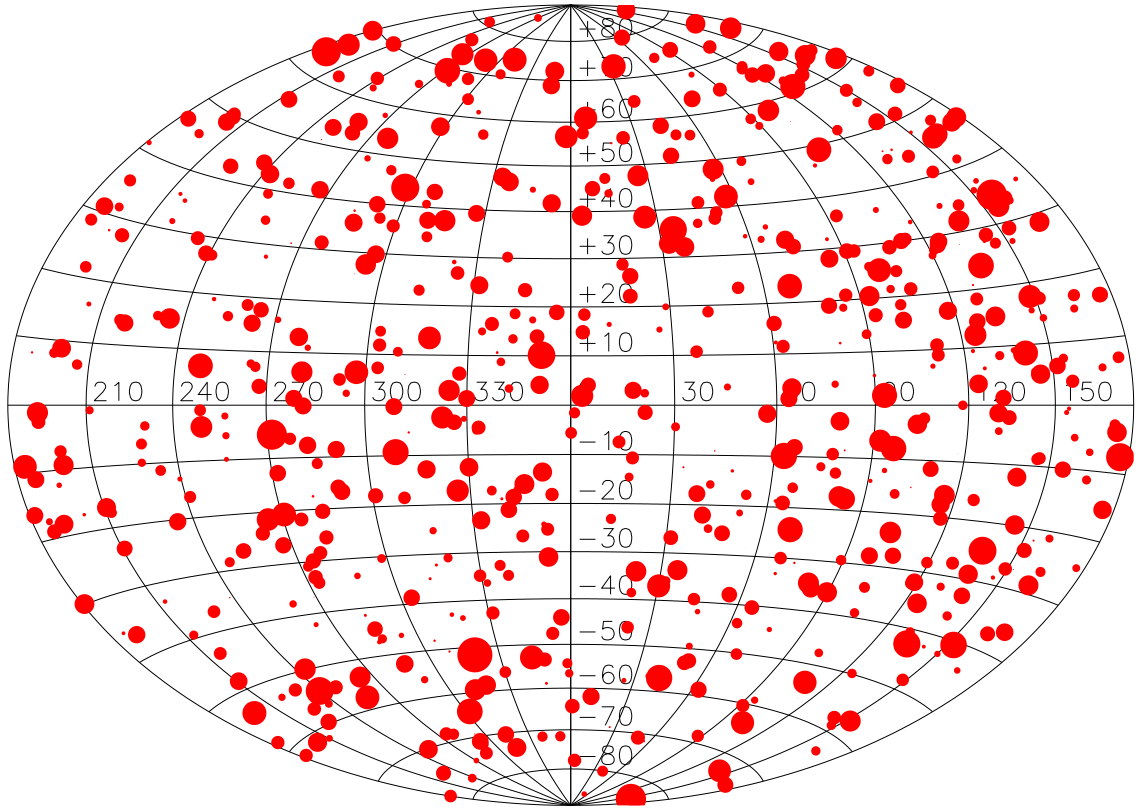


Figure 2.2: Distribution of *Swift* XRT Fields (Figure 2 from Dai et al. (2015)). Circle size corresponds to the comparative flux depth.

In Dai et al. (2015), we describe in detail the data reduction and methods used in producing the X-ray cluster catalog. Here, we briefly describe the reduction process and source extraction procedures. The *Swift* XRT has a relatively large field of view (23.4×23.4 arcmin^2) and is sensitive in the energy range of 0.2–10 keV. These GRB observations are of medium-depth, and randomly distributed on the sky for a total area of ~ 125 deg^2 with a median flux limit of 4×10^{-15} erg cm^{-2} s^{-1}. These data are ideal for finding galaxy clusters.

We downloaded all XRT "GRB" observations[2] before 2013-07-27, and reprocessed the data as described in Dai et al. (2015). From this, we made images and corresponding exposure maps in different energy ranges: total (0.2–10 keV), soft (0.5–2 keV), and hard (2–10 keV). Sources were detected in the images using the CIAO tool `wavdetect` using a significance of detection threshold of 10^{-6}. We excluded GRBs by matching the known GRB positions. To distinguish clusters from AGNs, we modeled the surface brightness profiles and compared to β-models with surface brightness $S \propto \left(1 + (R/R_c)^2\right)^{-3\beta+1/2}$ representing a range of cluster masses and redshifts. For the β-model parameters, we assume $\beta = 0.6$ and a core radius of $R_c = 0.1$ for a typical cluster redshift of $z = 0.5$, assuming a 2 Mpc physical radius (for more details on this, see Dai et al. (2015)). We defined an extended source to be a cluster candidate if it had a S/N ratio ≥ 4, a minimum net photon count of 20, and a size that is at least 3σ above the mean size of corresponding point sources at the same off axis angle. Since our cluster detection criteria require a minimum of 20 photons, all the cluster candidates should be

[2]from the HEASARC website: `http://heasarc.gsfc.nasa.gov`.

real astrophysical sources. False positives should arise only from confusing point AGN with extended sources. The catalog of these 442 cluster candidates is given in Table 2.1.

We compared the number counts of these extended sources/ cluster candidates to those from Rosati et al. (2002), a survey combining data from *ROSAT, Chandra*, and *XMM-Newton*, shown in Figure 2.3 (Fig. 18 from Dai et al. (2015)). Figure 2.3 shows good agreement between the studies, suggesting that the cluster candidates are in fact real clusters.

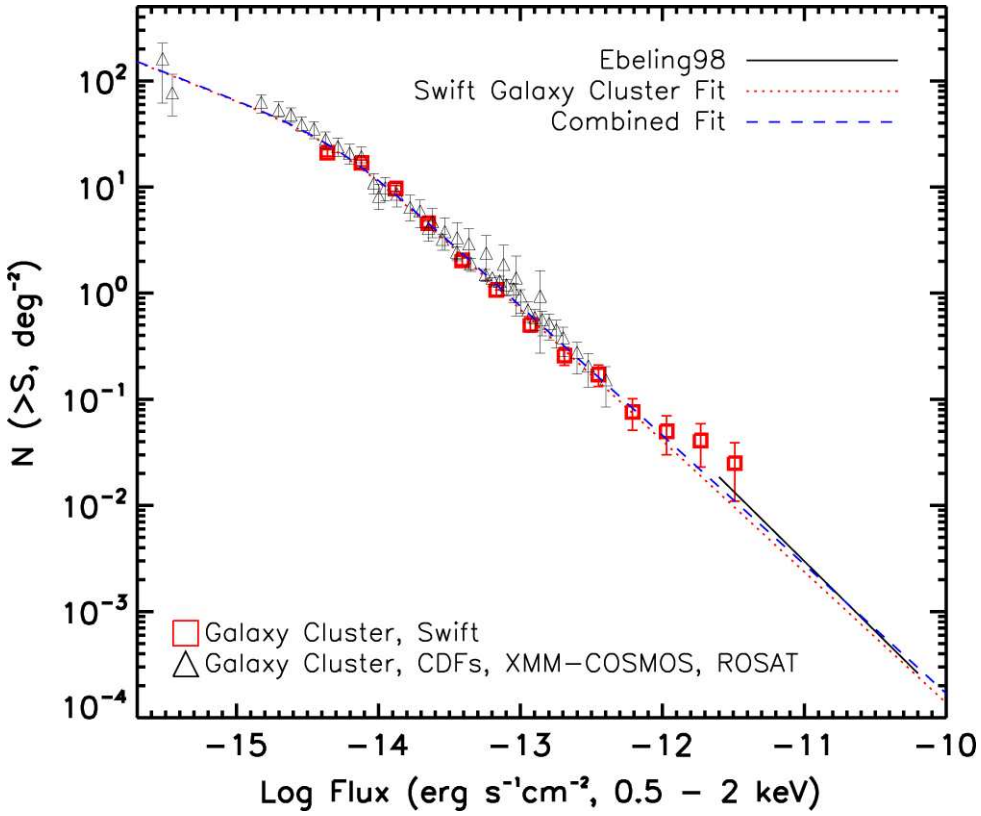


Figure 2.3: SACS cluster number counts (Fig. 18 from Dai et al. (2015)). The results from SACS agrees with similar studies, for more details see Dai et al. (2015).

Swift Extended Source Name	Core Size (arcsec)	Extent (arcsec)	CR (ct/ks)	CR error (ct/ks)	Flux (10^{-17} W/m^2)	Bkg Flux (0.36/s/deg^2)	Off (arcmin)	Exp (s)	GRB Date
SWCL J000131.7+444414	15.4	50.7	1.068	0.159	2.67	1.97	11.3	42004	101225a
SWCL J000251.5−525825	13.1	22.4	0.211	0.026	0.41	2.32	6.6	304365	070110
SWCL J000314.3−525514	32.5	83.7	2.420	0.088	4.69	2.22	5.6	314164	070110
SWCL J000323.8−525355	45.4	104.9	3.868	0.113	7.49	2.23	6.2	302754	070110
SWCL J000344.2−530152	41.1	62.5	1.034	0.058	2.00	2.23	2.5	310255	070110
SWCL J000755.7−295503	13.9	46.0	0.426	0.087	0.81	1.57	8.6	56789	070611
SWCL J001004.8+475139	12.5	31.8	0.408	0.059	1.05	1.88	8.1	115977	100802a
SWCL J001011.0+475353	18.6	36.5	0.467	0.066	1.21	1.84	10.5	105736	100802a
SWCL J001100.4+474827	11.9	31.8	0.320	0.064	0.83	1.82	12.1	78166	100802a
SWCL J001338.0−282923	18.5	48.3	0.935	0.196	1.81	2.19	14.9	24303	070721a
SWCL J001823.4+484350	16.7	76.6	2.605	0.471	6.76	1.66	12.1	11741	080602b
SWCL J002111.4+210438	13.5	34.2	0.503	0.073	1.08	1.66	8.8	94190	060912a
SWCL J002114.5+205943	19.2	43.6	0.580	0.077	1.25	1.61	3.8	98381	060912a
SWCL J002234.5−053949	18.1	55.4	0.481	0.088	1.00	1.86	9.6	62465	050922b
SWCL J002438.1−580354	46.2	152.0	5.283	0.263	9.98	1.63	7.3	76153	071031
SWCL J002626.3−711614	16.5	46.0	0.615	0.126	1.35	2.04	10.1	38770	050326
SWCL J002711.5−232201	29.5	76.6	1.020	0.166	1.99	1.48	7.4	37151	090123
SWCL J002716.4+092220	12.9	41.2	1.005	0.217	2.17	2.74	12.1	21294	100522a
SWCL J002729.2−232626	27.7	107.2	3.750	0.313	7.32	1.35	5.4	38294	090123
SWCL J002823.6+092705	25.1	76.6	2.371	0.260	5.13	2.93	5.8	35150	100522a
SWCL J002845.0−712112	20.4	50.7	0.578	0.111	1.27	2.12	7.2	46661	050326
SWCL J003317.8+193925	24.1	81.3	2.499	0.222	5.41	2.24	11.3	50724	080710
SWCL J003730.7−402756	11.0	60.1	1.362	0.190	2.81	1.66	3.1	37816	051105b
SWCL J003737.0−403820	11.9	46.0	0.717	0.144	1.48	1.54	7.9	34397	051105b
SWCL J004423.0+615210	13.2	41.2	0.336	0.062	2.05	1.45	3.8	87872	090621a
SWCL J004520.6−013744	17.3	41.2	0.526	0.084	1.08	1.67	5.2	73696	100117a
SWCL J005136.8+074351	17.7	69.5	0.804	0.162	1.82	1.60	7.2	30762	110210a
SWCL J005233.8+495407	38.9	149.7	10.210	0.497	30.07	2.04	3.9	41326	120729a
SWCL J005500.1−385229	47.5	90.7	2.737	0.255	5.71	1.49	5.1	42140	050911
SWCL J005657.1−465826	33.0	55.4	0.906	0.103	1.75	2.05	10.4	84854	111209a
SWCL J005724.1−463537	12.8	34.2	0.515	0.068	0.99	2.01	13.1	111638	111209a

Swift Extended Source Name	Core Size (arcsec)	Extent (arcsec)	CR (ct/ks)	CR error (ct/ks)	Flux (10^{-17} W/m^2)	Bkg Flux (0.36/s/deg^2)	Off (arcmin)	Exp (s)	GRB Date
SWCL J010655.6−412724	23.0	74.2	1.360	0.216	2.70	2.01	4.2	29086	060728
SWCL J012210.3+054733	15.4	64.8	2.014	0.327	4.30	1.30	9.8	18884	100823a
SWCL J012210.6−130420	76.6	149.7	4.481	0.260	8.93	1.56	6.7	66124	050908
SWCL J012303.8+375609	17.1	60.1	1.293	0.128	3.01	1.70	10.9	79192	081128
SWCL J012310.5+375549	12.3	38.9	0.390	0.075	0.91	1.68	11.3	68659	081128
SWCL J012946.9−180929	39.5	50.7	0.529	0.046	1.02	1.75	7.5	248938	100814a
SWCL J014148.5−473622	12.5	55.4	4.202	0.835	8.22	1.72	10.5	6024	081226b
SWCL J014806.5+474723	41.2	137.9	3.621	0.307	9.93	1.87	7.3	38384	051028
SWCL J014824.2+475208	17.0	55.4	0.663	0.118	1.82	2.10	7.0	47248	051028
SWCL J015021.6+612507	22.1	130.8	44.833	1.774	352.59	2.09	9.4	14251	081024a
SWCL J015132.8−182605	15.5	41.2	0.479	0.080	0.90	1.11	11.6	74375	070724a
SWCL J015656.5+164930	13.9	50.7	0.275	0.056	0.62	1.46	8.0	86603	091208b
SWCL J015703.4+164837	11.4	41.2	0.614	0.084	1.37	1.46	6.9	87696	091208b
SWCL J015751.5+170139	12.9	43.6	0.416	0.074	0.93	1.40	10.9	76640	091208b
SWCL J015752.9+165933	33.7	102.5	2.357	0.168	5.28	1.28	9.4	83074	091208b
SWCL J015803.5+165005	13.7	53.0	0.895	0.105	2.00	1.42	8.8	81918	091208b
SWCL J020003.8+084024	25.2	185.0	20.274	0.694	46.13	1.40	8.2	42121	120215a
SWCL J020006.4+084454	14.8	46.0	0.599	0.113	1.36	1.80	3.9	46518	120215a
SWCL J020258.9−165415	20.7	67.2	1.246	0.223	2.51	1.30	11.7	24982	091117
SWCL J020312.6−165321	19.3	62.5	0.743	0.148	1.50	1.67	9.1	33711	091117
SWCL J020719.1+332926	12.6	50.7	1.046	0.208	2.49	1.93	11.1	24195	090113
SWCL J020745.0+002053	20.6	71.9	1.857	0.147	3.72	1.66	4.7	85911	060908
SWCL J020934.7+641718	14.1	57.7	1.443	0.274	10.06	1.68	10.2	19231	080727c
SWCL J021007.7−270414	23.5	48.3	0.572	0.045	1.11	1.81	4.3	281159	110918a
SWCL J021044.7−271338	28.8	53.0	0.644	0.065	1.25	1.69	11.2	151325	110918a
SWCL J021220.4−020826	23.6	71.9	1.098	0.138	2.20	1.89	7.5	57282	070721b
SWCL J021250.0−021424	14.4	46.0	0.429	0.085	0.86	1.97	2.0	59123	070721b
SWCL J021644.4−501030	13.2	38.9	0.377	0.071	0.74	1.61	10.4	75068	050406
SWCL J021705.4−501409	43.6	154.4	7.280	0.232	14.31	1.50	7.3	135222	050406
SWCL J021747.3−500352	63.7	137.9	3.672	0.159	7.22	1.41	8.1	145356	050406
SWCL J022409.4+382635	12.5	38.9	0.828	0.163	1.83	2.78	10.3	31209	060202

Swift Extended Source Name	Core Size (arcsec)	Extent (arcsec)	CR (ct/ks)	CR error (ct/ks)	Flux (10^{-17} W/m^2)	Bkg Flux (0.36/s/deg^2)	Off (arcmin)	Exp (s)	GRB Date
SWCL J022546.1−185553	48.5	116.7	2.493	0.077	5.11	1.31	8.6	421687	091127
SWCL J022856.8−250618	12.2	29.5	0.324	0.058	0.63	1.43	4.6	97202	081230
SWCL J023301.8−711636	38.1	97.8	3.743	0.107	8.57	3.30	6.4	328278	080411
SWCL J024346.7−175421	13.4	36.5	0.446	0.094	0.90	1.57	7.8	50490	120224a
SWCL J025244.8−175405	13.1	46.0	0.520	0.103	1.07	1.51	10.1	48870	120212a
SWCL J025247.4−180613	17.4	60.1	0.649	0.119	1.34	1.54	9.7	45918	120212a
SWCL J025547.9+000902	12.5	53.0	1.315	0.233	3.08	1.31	9.5	24235	100728b
SWCL J025630.7+000601	83.7	116.7	1.539	0.262	3.61	1.59	10.8	22466	100728b
SWCL J030406.7−472930	14.8	53.0	0.788	0.125	1.50	1.04	11.0	50439	070209
SWCL J030414.7−502951	13.6	27.1	0.257	0.042	0.50	1.55	10.2	143291	061007
SWCL J030509.9−504359	19.1	67.2	0.772	0.120	1.51	1.53	11.1	53279	061007
SWCL J031314.0−430237	17.5	38.9	0.442	0.066	0.84	1.54	11.2	101240	070318
SWCL J031430.6+305035	11.9	34.2	0.577	0.079	1.58	1.86	4.3	91623	100902a
SWCL J032102.3+164257	11.5	36.5	0.378	0.065	0.98	1.15	10.5	89174	060218
SWCL J032216.0+164554	11.9	22.4	0.119	0.023	0.31	1.28	9.4	230784	060218
SWCL J032216.9+165331	15.2	24.7	0.169	0.028	0.44	1.35	10.3	208417	060218
SWCL J032336.0−460013	12.4	20.0	0.137	0.028	0.26	1.86	11.2	176004	050822
SWCL J035130.3+281517	15.8	48.3	0.714	0.116	1.69	1.99	3.3	53165	070714b
SWCL J035259.4−004338	21.5	147.3	13.982	0.355	38.56	1.85	2.3	110916	060904b
SWCL J035312.2+213345	41.0	81.3	1.804	0.144	4.95	2.06	5.7	86617	060211a
SWCL J041459.2−584345	28.1	79.0	2.481	0.117	4.77	1.90	7.9	180046	121027a
SWCL J042024.0−341003	10.7	36.5	0.493	0.068	1.00	1.39	5.0	106264	070328
SWCL J042253.7−245944	13.4	29.5	0.190	0.033	0.40	1.31	9.8	174164	080913
SWCL J042338.6−251617	19.1	46.0	0.296	0.055	0.62	1.23	10.5	98832	080913
SWCL J042422.3+640633	16.1	55.4	0.400	0.082	1.51	1.29	5.2	59174	120106a
SWCL J044120.9−112134	13.5	41.2	0.773	0.108	1.72	2.02	7.3	65781	081210
SWCL J044123.7−111550	19.9	38.9	0.558	0.091	1.24	1.99	6.7	66789	081210
SWCL J044140.3−110653	23.1	81.3	2.125	0.192	4.73	1.46	12.0	57766	081210
SWCL J044144.6−111534	34.0	112.0	4.905	0.259	10.93	1.93	3.3	73359	081210
SWCL J044149.3−112801	12.6	46.0	1.066	0.142	2.38	1.91	9.3	52946	081210
SWCL J044237.2−122251	14.4	46.0	0.616	0.128	1.41	1.77	12.3	37732	121024a

Swift Extended Source Name	Core Size (arcsec)	Extent (arcsec)	CR (ct/ks)	CR error (ct/ks)	Flux (10^{-17} W/m^2)	Bkg Flux (0.36/s/deg^2)	Off (arcmin)	Exp (s)	GRB Date
SWCL J045832.6−091111	22.2	86.0	5.208	0.342	11.84	2.22	10.0	44633	120907a
SWCL J050455.6−205015	15.6	48.3	0.598	0.116	1.21	1.74	7.8	44578	100508a
SWCL J050943.1+645512	17.9	79.0	2.778	0.119	7.81	1.32	8.6	195478	050712
SWCL J051046.0+644429	23.7	57.7	0.610	0.057	1.72	1.26	8.3	186586	050712
SWCL J051229.4+645453	16.9	53.0	0.886	0.081	2.49	1.19	9.7	133433	050712
SWCL J051236.8+645606	15.5	48.3	0.578	0.084	1.62	1.53	10.8	81866	050712
SWCL J052658.3−281126	14.5	55.4	0.886	0.153	1.75	2.19	7.2	37937	050915a
SWCL J053127.9−432104	21.5	60.1	1.174	0.163	2.47	1.69	11.5	44048	081118
SWCL J053810.3−265709	11.8	43.6	0.821	0.124	1.62	1.94	6.8	53721	100619a
SWCL J053818.5−265256	16.4	46.0	0.602	0.110	1.19	1.94	9.7	50003	100619a
SWCL J054643.7+511930	19.3	62.5	1.566	0.203	4.92	2.18	5.8	37828	080903
SWCL J054645.2+510920	15.1	50.7	0.883	0.170	2.77	2.06	7.6	30537	080903
SWCL J054653.1+510908	13.5	53.0	0.872	0.166	2.74	1.86	7.2	31679	080903
SWCL J054716.7+641156	20.3	27.1	0.165	0.026	0.44	1.60	3.7	250988	061126
SWCL J055023.7+032944	12.8	43.6	0.542	0.091	1.97	1.09	9.4	65896	070311
SWCL J055024.4+031613	15.6	46.0	0.458	0.083	1.66	1.25	6.8	66488	070311
SWCL J055114.1−023948	23.7	60.1	0.533	0.095	1.76	1.55	6.5	59599	050826
SWCL J055114.7−243615	29.5	79.0	1.135	0.218	2.21	1.66	10.8	23814	120211a
SWCL J055459.8−150820	16.0	55.4	0.978	0.146	2.62	2.19	9.6	46176	100728a
SWCL J055805.0−602920	17.1	38.9	0.463	0.075	1.00	1.58	12.8	82195	081121
SWCL J060133.8−521007	32.5	62.5	0.742	0.116	1.64	1.02	14.8	55436	090429a
SWCL J060208.4−522413	12.4	41.2	0.279	0.056	0.62	1.22	1.3	90549	090429a
SWCL J060740.1−464426	15.7	24.7	0.260	0.047	0.58	1.98	9.2	116203	090201
SWCL J060911.4−463808	11.9	24.7	0.271	0.053	0.60	2.00	11.0	96767	090201
SWCL J061951.6−090204	22.2	64.8	0.341	0.066	1.23	1.10	6.6	77463	090401b
SWCL J061955.7−084447	13.1	48.3	2.303	0.430	8.28	1.93	13.9	12428	090401b
SWCL J061958.9−084619	15.5	48.3	0.476	0.088	1.71	0.85	12.2	60754	090401b
SWCL J062041.4−090235	37.3	83.7	1.618	0.146	5.82	1.06	8.4	76217	090401b
SWCL J062155.7−622840	13.6	31.8	0.296	0.017	0.65	1.97	4.8	1058699	060729
SWCL J062330.3−010605	26.0	64.8	0.718	0.116	3.25	1.70	5.2	53597	060510a
SWCL J062830.8+461013	17.9	62.5	0.963	0.155	2.78	1.31	5.8	40052	061028

Swift Extended Source Name	Core Size (arcsec)	Extent (arcsec)	CR (ct/ks)	CR error (ct/ks)	Flux (10^{-17} W/m^2)	Bkg Flux (0.36/s/deg^2)	Off (arcmin)	Exp (s)	GRB Date
SWCL J062915.2+460619	41.4	128.5	50.274	1.760	145.02	2.48	10.4	16227	061028
SWCL J063009.1−455546	12.1	55.4	1.137	0.198	2.53	1.87	11.0	29095	061004
SWCL J063010.3−455815	35.7	114.3	3.561	0.297	7.92	1.27	11.4	40407	061004
SWCL J063159.7+624118	22.3	57.7	0.529	0.083	1.29	1.55	6.6	76241	080205
SWCL J063339.8+625038	33.8	62.5	0.590	0.086	1.44	1.55	8.3	80227	080205
SWCL J065407.9+715844	34.2	83.7	0.880	0.135	2.06	1.17	10.3	47982	060203
SWCL J070252.8−745158	26.8	62.5	1.372	0.131	3.84	1.38	7.5	80102	061202
SWCL J071501.5+493026	20.3	69.5	2.762	0.447	6.75	2.81	10.8	13815	111022b
SWCL J073204.4−540103	15.2	62.5	1.092	0.227	2.82	1.95	12.7	21217	091109b
SWCL J074755.5+515852	13.8	64.8	2.623	0.451	5.90	1.61	8.1	12872	130305a
SWCL J075036.6−003838	44.8	86.0	2.690	0.190	6.12	2.87	6.1	74510	090929b
SWCL J075043.2+310400	44.7	86.0	1.547	0.121	3.39	1.39	10.6	105169	070125
SWCL J075816.0+324542	16.1	50.7	0.423	0.081	0.95	1.99	7.7	63972	071020
SWCL J075900.8+324449	15.0	50.7	1.290	0.133	2.90	1.92	6.7	73317	071020
SWCL J075908.5+324237	14.3	41.2	0.438	0.086	0.98	1.61	9.4	59240	071020
SWCL J075912.7+325451	13.4	60.1	1.850	0.156	4.15	1.93	7.3	75565	071020
SWCL J075955.2−563224	12.8	36.5	0.376	0.053	1.13	1.41	7.6	132642	080916c
SWCL J080022.5−085931	12.2	36.5	0.606	0.121	1.50	2.05	7.0	41182	120119a
SWCL J080205.6−461432	11.0	34.2	0.675	0.088	2.49	1.90	7.1	86739	070227
SWCL J080211.2−463126	13.6	62.5	1.450	0.182	5.35	1.58	10.0	43780	070227
SWCL J081420.1−370807	13.1	22.4	0.174	0.021	1.40	1.87	3.4	379050	060428a
SWCL J081459.9−371137	13.9	22.4	0.122	0.019	0.99	1.72	7.9	334224	060428a
SWCL J082113.9+320018	34.4	128.5	6.664	0.236	14.04	1.51	7.6	119250	051227
SWCL J082708.2+255805	24.5	83.7	6.224	1.061	13.11	1.76	12.5	5527	090916
SWCL J083323.9+325722	14.2	48.3	0.639	0.089	1.38	1.25	7.1	79944	090102
SWCL J083340.9+331118	43.3	175.6	4.792	0.241	10.33	1.23	12.7	82570	090102
SWCL J083802.8−663858	10.8	48.3	1.086	0.169	2.77	2.95	8.2	38042	111107a
SWCL J083904.3−663918	13.5	50.7	0.802	0.155	2.05	2.45	11.1	33356	111107a
SWCL J083911.0+505229	12.4	46.0	0.695	0.140	1.47	1.65	8.6	35668	120219a
SWCL J083944.8+505413	12.7	48.3	0.719	0.143	1.52	1.58	9.2	34910	120219a
SWCL J084443.1+883723	21.5	83.7	1.086	0.184	2.61	1.23	9.8	32010	110201a

Swift Extended Source Name	Core Size (arcsec)	Extent (arcsec)	CR (ct/ks)	CR error (ct/ks)	Flux (10^{-17} W/m^2)	Bkg Flux (0.36/s/deg^2)	Off (arcmin)	Exp (s)	GRB Date
SWCL J084749.4+133142	22.4	211.0	55.333	0.799	115.55	2.50	13.2	86577	051016b
SWCL J084858.1+133047	13.2	29.5	0.295	0.056	0.62	2.02	6.9	95115	051016b
SWCL J084959.1+521711	12.4	38.9	0.636	0.080	1.30	1.92	9.8	99768	110503a
SWCL J085416.4−240703	33.8	163.8	16.962	0.316	45.35	1.87	7.3	170051	100704a
SWCL J085420.5−241439	26.8	46.0	0.629	0.061	1.68	2.17	3.1	169063	100704a
SWCL J085513.2−241544	15.9	43.6	0.865	0.078	2.31	2.06	9.5	142278	100704a
SWCL J085523.8+110202	45.7	145.0	3.436	0.194	7.29	1.03	7.9	91109	050416b
SWCL J085552.1+465925	15.8	50.7	0.595	0.105	1.19	1.63	11.6	54020	110106b
SWCL J085619.7+470018	16.5	64.8	0.466	0.089	0.93	1.74	7.7	58960	110106b
SWCL J090422.0−511837	63.1	100.2	1.677	0.140	14.48	1.43	8.9	85543	050916
SWCL J090611.0+350124	12.0	34.2	0.485	0.048	0.97	1.41	6.3	206347	080307
SWCL J090627.7+350621	39.7	57.7	0.535	0.047	1.07	1.36	1.8	247199	080307
SWCL J090714.8+351020	44.6	74.2	0.963	0.083	1.93	1.16	11.4	141506	080307
SWCL J091032.1+453015	20.3	60.1	0.699	0.119	1.33	1.49	8.4	49283	060121
SWCL J091215.7−115406	29.7	76.6	0.756	0.099	1.67	1.37	9.3	77845	090516
SWCL J091251.4−120045	11.4	38.9	0.441	0.081	0.98	1.57	9.9	66907	090516
SWCL J091258.0−120012	16.6	53.0	0.640	0.091	1.41	1.57	9.4	77681	090516
SWCL J091336.4−114305	18.8	53.0	0.533	0.107	1.18	1.44	13.5	46434	090516
SWCL J091606.3+871121	12.9	53.0	0.927	0.195	2.13	3.58	6.1	24289	130528a
SWCL J092607.0+314854	21.9	64.8	0.964	0.161	1.87	1.48	9.9	37286	100205a
SWCL J092642.2+300835	19.3	36.5	0.460	0.074	0.90	1.80	6.9	84598	050505
SWCL J092649.8+301346	21.8	74.2	2.221	0.116	4.33	1.59	2.4	164805	050505
SWCL J092719.6+301348	41.1	128.5	4.304	0.165	8.38	1.55	4.0	158461	050505
SWCL J092730.1+301046	23.6	149.7	11.455	0.290	22.30	1.27	7.1	136130	050505
SWCL J092852.3+002137	16.7	53.0	0.694	0.145	1.44	1.57	10.6	33101	090519
SWCL J093041.3+170400	12.5	31.8	0.226	0.039	0.48	1.09	9.3	144980	050502b
SWCL J093045.4+165930	113.3	173.2	3.751	0.165	7.94	0.98	8.6	137011	050502b
SWCL J094015.6−215352	14.4	22.4	0.113	0.014	0.25	1.69	4.9	563286	061021
SWCL J094722.3+315650	28.4	67.2	0.732	0.113	1.43	1.30	9.0	57447	060108
SWCL J094817.0−131646	18.5	67.2	1.614	0.093	3.49	1.52	11.6	185730	061121
SWCL J094822.7+320018	14.9	53.0	0.478	0.089	0.93	1.31	10.4	60456	060108

Swift Extended Source Name	Core Size (arcsec)	Extent (arcsec)	CR (ct/ks)	CR error (ct/ks)	Flux (10^{-17} W/m^2)	Bkg Flux (0.36/s/deg^2)	Off (arcmin)	Exp (s)	GRB Date
SWCL J094959.1−421753	12.0	38.9	0.417	0.079	1.44	1.84	2.6	66315	130211a
SWCL J095206.7+102137	21.6	53.0	0.758	0.080	1.56	1.36	7.9	117114	070306
SWCL J095257.1+102440	16.0	41.2	0.719	0.126	1.48	1.73	10.2	45279	070306
SWCL J095327.3−170122	12.6	62.5	1.070	0.186	2.36	1.85	6.7	30886	061102
SWCL J095513.4+181215	32.2	90.7	1.671	0.134	3.45	1.34	5.4	93560	090423
SWCL J095515.5+180357	34.3	93.1	1.823	0.150	3.76	1.43	5.5	80710	090423
SWCL J095542.0+180007	15.6	38.9	0.365	0.071	0.75	1.29	8.8	72084	090423
SWCL J095543.4+133021	15.6	64.8	1.338	0.263	2.74	2.18	9.1	19344	130418a
SWCL J100055.8−681440	12.0	50.7	0.991	0.127	2.80	1.74	6.7	61771	110223b
SWCL J101341.5+430651	20.5	62.5	1.294	0.098	2.46	1.63	2.9	135539	070223
SWCL J101438.6+431350	13.3	46.0	0.868	0.093	1.65	1.55	9.9	100538	070223
SWCL J101548.9+273122	12.8	31.8	0.479	0.084	0.97	2.06	8.2	68538	111016a
SWCL J102036.8+413227	11.9	43.6	0.894	0.160	1.67	1.21	10.9	34706	080315
SWCL J104143.8−205946	25.3	62.5	1.307	0.137	2.77	1.83	9.6	70068	061217
SWCL J104158.8−211124	15.6	41.2	0.823	0.103	1.74	1.87	3.1	77448	061217
SWCL J105314.1−451821	21.4	67.2	0.939	0.157	2.48	1.29	13.6	38118	100316b
SWCL J110932.9−202209	17.3	50.7	0.876	0.126	1.84	1.68	10.8	55407	101204a
SWCL J111343.9+421409	12.4	55.4	1.044	0.137	2.07	1.45	7.2	55521	100305a
SWCL J111736.0+033711	45.6	234.5	10.164	0.457	22.20	1.55	9.1	48610	100513a
SWCL J111745.7+034055	16.8	46.0	0.562	0.102	1.23	1.82	8.3	53843	100513a
SWCL J112509.0+481026	25.9	74.2	1.485	0.190	2.84	1.59	11.2	41229	130131a
SWCL J113147.1+274816	20.4	34.2	0.295	0.034	0.58	1.66	13.1	257682	130427a
SWCL J113309.5+274516	16.7	27.1	0.179	0.025	0.35	1.80	9.9	276603	130427a
SWCL J113427.6−070208	26.0	107.2	4.579	0.382	9.57	1.16	10.6	31382	080613b
SWCL J114232.3+505623	28.8	48.3	0.621	0.072	1.19	1.93	3.9	119448	091020
SWCL J114332.8+504856	15.1	41.2	0.467	0.087	0.89	1.68	11.6	61242	091020
SWCL J114444.2+595514	28.5	29.5	0.143	0.017	0.28	1.36	6.8	471040	060319
SWCL J114503.1+600811	33.3	67.2	0.756	0.042	1.46	1.15	10.1	428562	060319
SWCL J114553.0+595320	26.7	55.4	0.692	0.037	1.33	1.36	6.0	516215	060319
SWCL J114556.9+595807	10.8	20.0	0.087	0.012	0.17	1.36	3.3	598948	060319
SWCL J115621.5−132242	14.7	31.8	0.418	0.067	0.90	1.88	4.6	94105	070224

Swift Extended Source Name	Core Size (arcsec)	Extent (arcsec)	CR (ct/ks)	CR error (ct/ks)	Flux (10^{-17} W/m^2)	Bkg Flux (0.36/s/deg^2)	Off (arcmin)	Exp (s)	GRB Date
SWCL J115811.3+452903	61.1	104.9	1.928	0.131	3.65	1.21	5.4	113135	060123
SWCL J115909.6+453322	12.3	29.5	0.281	0.047	0.53	1.42	6.4	126589	060123
SWCL J120137.8+104936	11.5	34.2	0.590	0.059	1.15	1.71	10.4	169381	050408
SWCL J120156.1+110003	16.0	36.5	0.493	0.070	0.96	1.62	10.9	101402	050408
SWCL J120200.0+105842	11.2	27.1	0.244	0.036	0.47	1.72	9.2	189944	050408
SWCL J120529.6+395734	16.2	41.2	0.487	0.104	0.98	1.61	10.2	45010	070412
SWCL J121012.4+395904	35.6	95.5	1.524	0.137	3.07	1.22	10.0	81051	070419a
SWCL J121137.4+395219	15.0	43.6	0.343	0.067	0.69	1.59	8.3	76098	070419a
SWCL J121412.5−490118	11.5	43.6	0.698	0.117	1.78	1.76	10.1	51114	090308
SWCL J121628.2+353820	20.4	34.2	0.335	0.048	0.64	1.84	8.0	144405	060712
SWCL J121711.8+353745	25.4	60.1	1.437	0.157	2.76	1.99	12.1	58486	060712
SWCL J122327.6+153927	13.4	46.0	0.865	0.153	1.71	2.15	6.4	36769	110407a
SWCL J122340.2+154539	16.9	41.2	0.534	0.112	1.06	2.16	5.2	42535	110407a
SWCL J122445.4+154903	21.6	79.0	2.504	0.382	4.96	2.04	14.8	17160	110407a
SWCL J123313.9+210217	47.7	100.2	2.317	0.102	4.68	1.45	7.8	220532	050416a
SWCL J123533.0+325558	13.0	46.0	0.596	0.118	1.15	1.51	10.0	42998	090426
SWCL J123612.4+290222	16.1	46.0	0.763	0.150	1.47	1.77	3.0	34025	050509b
SWCL J123717.7+164353	20.5	71.9	2.348	0.108	4.60	1.64	11.0	200275	090424
SWCL J123801.7+164234	18.9	24.7	0.167	0.026	0.33	2.14	5.7	248808	090424
SWCL J124308.5+170639	13.2	31.8	0.325	0.058	0.63	1.72	10.0	96828	090323
SWCL J124312.1+170454	20.8	64.8	1.753	0.134	3.41	1.65	9.5	97539	090323
SWCL J125814.0−111333	13.7	38.9	0.545	0.104	1.15	2.52	7.9	50364	100724a
SWCL J125840.3−110230	12.9	36.5	0.503	0.104	1.06	2.61	10.2	46381	100724a
SWCL J125842.9−110032	18.9	60.1	1.642	0.198	3.46	2.23	11.6	41849	100724a
SWCL J125957.2+155717	11.6	46.0	0.588	0.092	1.15	1.85	3.6	69352	080607
SWCL J130332.1+591556	13.1	24.7	0.265	0.052	0.50	1.84	7.3	96353	130420a
SWCL J130345.6+593437	17.4	38.9	0.466	0.076	0.88	1.71	14.0	80235	130420a
SWCL J130911.8+611521	13.9	60.1	0.879	0.183	1.70	1.70	3.9	26346	110402a
SWCL J130959.1+612530	22.5	95.5	3.518	0.399	6.82	1.50	11.2	22044	110402a
SWCL J131521.9+164155	23.1	133.2	19.300	0.812	37.48	3.34	13.1	29293	070406
SWCL J131616.9−650339	33.1	43.6	1.401	0.224	13.15	4.74	11.8	28035	080229b

Swift Extended Source Name	Core Size (arcsec)	Extent (arcsec)	CR (ct/ks)	CR error (ct/ks)	Flux (10^{-17} W/m^2)	Bkg Flux (0.36/s/deg^2)	Off (arcmin)	Exp (s)	GRB Date
SWCL J131951.6−315317	20.5	62.5	1.924	0.246	4.31	1.63	12.4	31753	050726
SWCL J132012.6−320718	25.0	74.2	1.582	0.182	3.55	2.37	2.5	47853	050726
SWCL J132024.8−320244	12.5	50.7	1.371	0.170	3.07	2.46	4.9	47492	050726
SWCL J132048.4−320602	12.2	41.2	0.819	0.140	1.84	2.18	9.1	41600	050726
SWCL J132959.5+422839	21.2	67.2	0.815	0.147	1.53	1.14	8.2	37588	050502a
SWCL J133051.0+420641	39.9	83.7	1.242	0.086	2.31	1.39	7.1	167527	051008
SWCL J133055.8+420015	16.1	79.0	3.776	0.150	7.03	1.50	7.2	168789	051008
SWCL J133437.4−100927	59.2	161.5	7.320	0.628	15.22	1.71	10.5	18569	090720a
SWCL J134938.9+072258	13.3	38.9	0.751	0.150	1.48	2.97	10.0	33336	080207
SWCL J135816.3+465638	12.6	41.2	0.367	0.073	0.71	1.57	6.5	69388	090417b
SWCL J135914.0+470528	17.0	46.0	0.372	0.071	0.72	1.56	6.8	73318	090417b
SWCL J140331.0+321214	20.5	62.5	0.957	0.172	1.81	1.34	9.7	32445	090429b
SWCL J140637.3+274348	23.9	166.2	14.777	0.421	28.57	1.30	7.8	83393	060204b
SWCL J140639.0+273546	47.8	180.3	9.585	0.345	18.53	1.28	7.7	80757	060204b
SWCL J140659.6+274137	12.8	31.8	0.249	0.050	0.48	1.58	2.5	97839	060204b
SWCL J140726.4+274738	19.7	46.0	0.785	0.095	1.52	1.45	8.6	86436	060204b
SWCL J140907.4+242406	18.1	43.6	0.354	0.067	0.68	1.49	10.3	78467	090529a
SWCL J141031.4+242854	20.2	53.0	0.512	0.087	0.99	1.26	9.4	68104	090529a
SWCL J141221.8+165216	12.4	34.2	0.426	0.082	0.81	2.46	6.0	63949	060801
SWCL J141242.9+165408	15.5	53.0	0.756	0.122	1.44	2.26	8.6	50652	060801
SWCL J141342.2+050814	15.7	81.3	4.846	0.822	9.58	2.35	11.8	7169	080613a
SWCL J143101.1+362235	12.7	31.8	0.224	0.026	0.42	1.21	9.0	341434	080319b
SWCL J143211.6+362225	27.2	46.0	0.375	0.030	0.70	1.25	7.6	415150	080319b
SWCL J143223.3+361752	15.2	64.8	1.412	0.064	2.65	1.06	8.7	341152	080319b
SWCL J143945.7−000733	26.0	69.5	1.898	0.146	3.98	1.76	8.6	89139	080310
SWCL J144045.0−000320	17.4	50.7	0.451	0.084	0.95	1.73	10.9	63688	080310
SWCL J144209.2+333414	13.4	55.4	1.223	0.211	2.29	1.58	10.4	27459	081011
SWCL J144604.5+203334	12.3	31.8	0.326	0.047	0.65	2.45	8.5	146551	060814
SWCL J151508.0+441837	45.4	93.1	1.766	0.177	3.48	1.83	6.3	56277	081203b
SWCL J151550.9+442056	11.6	46.0	1.159	0.148	2.28	1.83	7.8	52752	081203b
SWCL J152252.9+253527	28.7	128.5	7.722	0.384	16.52	1.78	2.4	52369	100526a

Swift Extended Source Name	Core Size (arcsec)	Extent (arcsec)	CR (ct/ks)	CR error (ct/ks)	Flux (10^{-17} W/m^2)	Bkg Flux (0.36/s/deg^2)	Off (arcmin)	Exp (s)	GRB Date
SWCL J152253.9+252610	17.2	50.7	1.127	0.175	2.41	1.55	10.0	36805	100526a
SWCL J152316.4+254754	14.4	46.0	0.613	0.129	1.31	1.61	12.4	37075	100526a
SWCL J154003.5+615843	14.0	43.6	0.385	0.065	0.73	1.32	9.4	92482	060428b
SWCL J154536.9−034754	20.2	27.1	0.370	0.068	0.94	2.42	6.3	81110	060418
SWCL J155059.9−783337	13.2	48.3	1.852	0.395	4.61	2.08	8.2	11849	070509
SWCL J155117.4+445118	24.7	81.3	1.915	0.114	3.63	1.35	4.1	146326	060904a
SWCL J155159.8+445748	20.2	46.0	0.626	0.084	1.19	1.45	9.4	89260	060904a
SWCL J155517.5+405121	13.6	55.4	0.978	0.171	1.88	2.03	3.0	33571	110709a
SWCL J155555.3+410548	17.3	67.2	3.228	0.398	6.21	1.78	13.3	20390	110709a
SWCL J155644.8+782352	13.4	38.9	0.383	0.074	0.83	1.68	9.1	69610	060510b
SWCL J155708.6+354100	22.4	34.2	0.303	0.045	0.60	1.77	12.3	151832	090404
SWCL J155743.3+353020	47.6	234.5	102.713	0.809	202.76	1.29	7.4	156904	090404
SWCL J160205.9+663015	19.5	50.7	0.505	0.092	1.06	1.30	11.0	60168	060502a
SWCL J160637.5+321351	18.8	53.0	0.982	0.097	1.97	1.83	8.1	103707	060219
SWCL J160756.6+112414	15.2	41.2	0.889	0.160	1.95	3.23	9.7	34691	050813
SWCL J160956.9+301052	21.7	81.3	1.563	0.190	3.23	1.28	9.6	43432	070521
SWCL J162315.0+074021	14.3	20.0	0.283	0.046	0.63	4.70	5.9	135507	110102a
SWCL J162448.5−273919	35.7	50.7	0.941	0.107	2.78	2.94	6.6	82867	050724
SWCL J163054.8+015924	24.2	74.2	4.575	0.641	10.07	7.09	11.0	11143	050401
SWCL J163712.2+294638	12.6	50.7	1.202	0.197	2.38	2.08	8.4	30855	130606a
SWCL J163741.6+295700	14.8	48.3	0.860	0.180	1.70	1.99	12.2	26419	130606a
SWCL J164552.1+364057	10.9	34.2	0.377	0.053	0.73	1.36	6.2	135327	091003
SWCL J164633.7+000328	20.4	50.7	1.298	0.256	3.06	4.97	2.0	19825	090111
SWCL J164637.4+363021	15.7	43.6	0.270	0.053	0.53	1.22	12.6	94809	091003
SWCL J164649.1+364007	13.5	31.8	0.269	0.048	0.52	1.36	14.8	115233	091003
SWCL J164956.4+313021	14.1	53.0	1.145	0.104	2.31	1.56	5.7	106653	060807
SWCL J165354.9−281552	32.1	41.2	1.811	0.217	5.37	6.94	8.1	38584	050721
SWCL J165742.5+552458	18.7	41.2	0.464	0.063	0.89	1.59	11.7	115922	070518
SWCL J165807.1+121138	16.8	24.7	0.296	0.047	0.66	4.02	10.8	136273	060923a
SWCL J170542.2+112451	13.0	22.4	0.370	0.042	0.83	4.88	4.8	204825	100418a
SWCL J170708.5+240835	17.7	50.7	0.839	0.170	1.82	2.04	10.3	28881	121202a

Swift Extended Source Name	Core Size (arcsec)	Extent (arcsec)	CR (ct/ks)	CR error (ct/ks)	Flux (10^{-17} W/m^2)	Bkg Flux (0.36/s/deg^2)	Off (arcmin)	Exp (s)	GRB Date
SWCL J170716.1+235208	14.1	55.4	0.941	0.171	2.04	2.26	6.2	32160	121202a
SWCL J170757.1+235135	15.7	60.1	3.195	0.487	6.94	2.36	11.7	13479	121202a
SWCL J172011.1+692315	15.8	64.8	0.837	0.145	1.80	1.85	4.3	39673	070219
SWCL J173302.3+490920	14.9	36.5	0.481	0.087	0.96	1.66	9.6	63234	100614a
SWCL J173316.3+492211	20.9	57.7	0.705	0.106	1.41	1.39	12.2	63333	100614a
SWCL J173719.2+461253	41.3	79.0	1.543	0.108	3.09	1.46	7.8	132783	050814
SWCL J173721.7+461832	40.8	109.6	3.896	0.167	7.80	1.69	5.1	139534	050814
SWCL J173932.8+272051	25.3	86.0	2.738	0.141	5.95	1.69	5.1	137679	090902b
SWCL J174131.4−421714	18.5	27.1	0.605	0.115	2.26	5.11	8.6	45904	080919
SWCL J175640.7+332929	11.8	69.5	3.842	0.329	8.17	2.35	7.5	35510	090418a
SWCL J180104.4−525307	13.5	36.5	1.075	0.220	2.82	4.90	11.3	22204	051012
SWCL J180228.7−523651	16.9	126.1	119.018	3.235	311.98	11.17	12.3	11370	051012
SWCL J180541.4−623827	18.5	62.5	1.671	0.323	4.05	3.12	8.8	16013	050223
SWCL J181053.5+581524	33.9	97.8	7.615	0.790	15.90	2.65	11.5	12207	060805b
SWCL J181230.1+141634	21.1	64.8	1.494	0.300	4.01	3.20	2.7	16593	120311a
SWCL J181508.9+690612	14.9	48.3	0.866	0.158	1.97	2.30	8.4	34609	120326a
SWCL J181619.2−364811	11.7	48.3	1.601	0.295	4.36	4.00	8.8	18450	060322
SWCL J181628.8+691131	68.2	135.5	6.245	0.347	14.22	2.35	5.8	51929	120326a
SWCL J181709.6−681255	14.1	57.7	2.516	0.390	6.24	4.22	10.2	16576	130615a
SWCL J182024.2−681540	13.4	36.5	0.921	0.174	2.29	3.84	9.0	30411	130615a
SWCL J182227.0−591546	18.9	55.4	1.658	0.313	3.95	3.79	11.4	16928	120909a
SWCL J182443.5+373204	13.8	38.9	0.534	0.062	1.10	1.86	3.0	137104	060111a
SWCL J182509.1+373132	15.6	27.1	0.265	0.045	0.55	1.87	5.2	133629	060111a
SWCL J183129.0+363503	12.1	50.7	0.711	0.135	1.52	1.96	4.5	39305	080325
SWCL J183606.8+173201	26.0	57.7	0.728	0.124	2.37	2.39	10.2	47092	110315a
SWCL J183744.0+624135	12.4	48.3	1.815	0.363	4.06	2.54	0.9	13775	080603a
SWCL J184037.6−550441	11.1	46.0	1.929	0.309	4.64	3.92	3.8	20172	080520
SWCL J184929.4−091328	19.7	53.0	1.458	0.232	5.70	4.15	3.2	27179	050306
SWCL J190614.5+555534	40.9	163.8	9.979	0.518	22.86	1.43	8.7	37259	110726a
SWCL J190617.8+685323	12.4	48.3	0.814	0.124	1.87	1.45	8.9	53175	080503
SWCL J190620.9+555237	12.0	79.0	3.658	0.394	8.38	1.62	10.9	23608	110726a

Swift Extended Source Name	Core Size (arcsec)	Extent (arcsec)	CR (ct/ks)	CR error (ct/ks)	Flux (10^{-17} W/m^2)	Bkg Flux (0.36/s/deg^2)	Off (arcmin)	Exp (s)	GRB Date
SWCL J190633.0+701200	14.7	50.7	0.590	0.119	1.45	1.56	9.2	41640	060111b
SWCL J190633.9+560146	16.7	50.7	0.528	0.111	1.21	1.86	2.3	42967	110726a
SWCL J190634.7+065312	22.5	81.3	2.154	0.396	34.06	1.46	12.8	13740	110625a
SWCL J191020.9−184932	24.1	67.2	2.578	0.454	6.58	4.34	6.8	12533	080905a
SWCL J191858.7+020641	20.0	57.7	1.443	0.265	5.41	2.43	9.7	20565	071109
SWCL J191923.2+765324	11.2	36.5	0.588	0.082	1.34	1.75	1.5	87560	100725b
SWCL J193500.7+781406	10.7	31.8	0.393	0.037	0.91	1.69	5.2	291104	090618
SWCL J193640.1+361913	16.5	38.9	0.561	0.115	1.67	2.99	5.0	42518	110921a
SWCL J194004.2+782415	42.3	71.9	1.410	0.113	3.26	1.89	13.9	110341	090618
SWCL J194530.3−080149	20.2	57.7	0.782	0.153	1.94	2.43	4.2	33582	130514a
SWCL J194548.1−080741	13.5	69.5	3.937	0.627	9.74	2.91	11.4	10014	130514a
SWCL J194911.9+462330	11.7	34.2	0.427	0.064	1.30	1.62	9.2	103931	060105
SWCL J194916.9+461618	65.3	187.4	9.059	0.280	27.63	1.41	8.1	115923	060105
SWCL J200005.7+524438	13.2	31.8	0.362	0.078	1.13	1.89	10.7	59398	100805a
SWCL J200031.1+085259	11.5	38.9	1.260	0.177	3.57	3.16	11.5	40432	050607
SWCL J200129.8+090720	14.1	43.6	1.565	0.210	4.44	2.98	13.6	35430	050607
SWCL J200414.4+651738	25.6	69.5	0.882	0.161	2.33	3.22	7.4	34224	120213a
SWCL J200516.9−623046	12.1	29.5	0.314	0.067	0.67	1.83	11.4	71019	080905b
SWCL J201441.5+060518	18.6	62.5	1.087	0.205	2.86	2.05	8.1	25886	120923a
SWCL J201523.9+152950	60.2	175.6	12.332	0.269	35.05	1.79	3.1	169888	061122
SWCL J201549.0+153231	11.4	31.8	0.448	0.057	1.27	1.91	9.6	139361	061122
SWCL J202855.7−524106	17.9	50.7	0.720	0.120	1.51	2.35	8.6	49924	111129a
SWCL J202908.6−524651	14.3	34.2	0.553	0.108	1.16	2.35	8.2	47352	111129a
SWCL J203050.8+605628	13.4	43.6	0.360	0.076	1.18	1.44	4.0	62692	050713b
SWCL J203557.3−440228	13.7	34.2	0.441	0.086	0.91	2.16	14.6	59680	091109
SWCL J203723.2−440423	12.9	27.1	0.362	0.066	0.75	2.21	6.7	83148	091109
SWCL J203724.0−440153	45.4	69.5	1.309	0.129	2.71	2.16	9.1	78317	091109
SWCL J204129.7+540605	16.2	29.5	0.232	0.045	0.97	1.59	6.7	116902	050509a
SWCL J204158.7+541209	12.2	29.5	0.285	0.052	1.19	1.38	8.9	106936	050509a
SWCL J204202.0+535417	24.2	62.5	0.815	0.091	3.41	1.17	9.3	97943	050509a
SWCL J204744.1−782318	12.5	34.2	0.497	0.107	1.23	1.40	8.3	43405	070508

Swift Extended Source Name	Core Size (arcsec)	Extent (arcsec)	CR (ct/ks)	CR error (ct/ks)	Flux (10^{-17} W/m^2)	Bkg Flux (0.36/s/deg^2)	Off (arcmin)	Exp (s)	GRB Date
SWCL J210019.6−223639	12.2	55.4	1.312	0.270	2.91	2.81	10.8	17959	130427b
SWCL J210332.8+650200	12.2	36.5	0.499	0.043	1.87	1.29	10.0	268572	090727
SWCL J210348.0+650247	22.8	34.2	0.206	0.028	0.77	1.29	10.7	263726	090727
SWCL J210442.9+644555	11.9	29.5	0.245	0.032	0.92	1.26	8.9	235161	090727
SWCL J212057.2−411307	28.4	100.2	5.428	0.515	11.45	3.86	9.3	20488	110420b
SWCL J212442.0−530405	30.8	43.6	0.436	0.037	0.86	2.19	11.2	320179	060614
SWCL J213130.8+211616	33.8	81.3	2.186	0.219	5.08	2.17	6.3	45429	081024b
SWCL J213512.8+065810	14.9	43.6	0.885	0.181	1.89	1.97	6.4	26932	061110b
SWCL J213752.0+554406	12.4	27.1	0.123	0.020	1.17	1.04	3.8	300940	050422
SWCL J214359.4−563725	35.5	234.5	192.959	4.995	392.09	2.93	9.8	7735	110319b
SWCL J214405.7−195813	13.2	29.5	0.595	0.084	1.24	3.64	7.6	84455	080413b
SWCL J214409.9−195600	16.4	119.0	25.187	0.554	52.30	3.34	7.1	82110	080413b
SWCL J214515.6−195944	102.5	234.5	23.615	0.537	49.03	2.57	8.9	81884	080413b
SWCL J214550.6−564451	22.6	86.0	15.207	1.891	30.90	3.66	12.0	4254	110319b
SWCL J215206.3−334026	29.3	93.1	1.674	0.239	3.29	1.81	10.0	29289	081211a
SWCL J215357.0+165313	45.3	88.4	2.828	0.126	6.51	2.17	13.5	179308	051221a
SWCL J215411.4−001127	17.7	38.9	0.686	0.129	1.60	1.59	8.6	41493	090809a
SWCL J215411.6−000654	12.0	50.7	0.561	0.115	1.31	1.66	7.6	42189	090809a
SWCL J215413.2+000413	23.7	83.7	4.197	0.505	9.81	2.16	13.7	16471	090809a
SWCL J215423.1+000526	16.4	62.5	2.778	0.400	6.49	2.05	13.7	17403	090809a
SWCL J215453.5−530953	11.6	41.2	0.441	0.085	0.86	2.07	3.7	60859	080804
SWCL J215507.7+164725	20.6	34.2	0.404	0.035	0.93	2.52	5.3	329824	051221a
SWCL J215510.7+165038	11.9	17.7	0.100	0.016	0.23	2.50	4.3	378417	051221a
SWCL J215520.0−001115	18.2	57.7	0.900	0.154	2.10	1.35	10.3	37818	090809a
SWCL J215827.8+385338	20.0	69.5	1.254	0.251	3.86	1.70	10.4	19848	080506
SWCL J215831.9−222439	11.9	36.5	0.398	0.078	0.80	1.95	6.9	64857	060607a
SWCL J215945.5−573952	14.3	43.6	1.432	0.218	2.83	2.50	8.7	30121	051210
SWCL J215952.8+262539	15.6	38.9	0.441	0.093	1.02	1.85	4.9	51400	110112a
SWCL J220026.5+405625	54.9	107.2	1.790	0.096	5.51	1.15	11.6	195601	051109a
SWCL J221447.9−384030	14.7	43.6	3.910	0.805	7.39	18.03	4.5	6038	110721a
SWCL J222432.9−021216	25.7	38.9	0.304	0.039	0.67	1.72	9.1	196888	061110a

Swift Extended Source Name	Core Size (arcsec)	Extent (arcsec)	CR (ct/ks)	CR error (ct/ks)	Flux (10^{-17} W/m^2)	Bkg Flux (0.36/s/deg^2)	Off (arcmin)	Exp (s)	GRB Date
SWCL J222438.0−022231	24.9	62.5	1.218	0.080	2.68	1.60	7.9	189989	061110a
SWCL J222439.0−021111	34.5	43.6	0.340	0.041	0.75	1.62	8.7	200843	061110a
SWCL J222444.0−022034	25.1	53.0	0.732	0.058	1.61	1.76	5.6	219622	061110a
SWCL J222506.2−020611	14.4	29.5	0.245	0.044	0.54	1.48	11.4	125064	061110a
SWCL J222516.4−020825	20.1	46.0	0.680	0.061	1.49	1.76	9.8	185503	061110a
SWCL J222954.1+194350	32.6	88.4	2.524	0.128	5.57	1.70	12.4	154180	050820a
SWCL J223747.4−294022	15.7	41.2	0.427	0.087	0.81	2.23	7.0	56916	120703a
SWCL J224206.9+233408	38.4	112.0	4.891	0.297	10.91	2.51	8.9	55420	071021
SWCL J225533.4−710846	27.8	71.9	1.455	0.161	3.00	1.43	10.1	56193	090927
SWCL J230207.3+384751	42.5	100.2	1.594	0.149	4.40	1.39	9.7	72013	051109b
SWCL J230226.1+384830	31.7	76.6	0.768	0.123	2.12	1.41	11.7	51104	051109b
SWCL J230227.3+383724	12.6	48.3	0.398	0.075	1.10	1.34	6.5	69985	051109b
SWCL J230231.5+384252	12.9	55.4	0.617	0.095	1.70	1.40	8.4	68733	051109b
SWCL J230337.0+550001	11.5	29.5	0.442	0.054	1.88	2.05	9.1	153804	051211b
SWCL J230650.4−680400	108.9	213.3	13.112	0.390	26.93	1.91	8.4	86050	081029
SWCL J230754.9−681506	12.2	48.3	1.658	0.141	3.41	2.34	9.1	83976	081029
SWCL J231257.7+182543	15.0	50.7	0.788	0.136	1.78	1.71	7.4	42880	051111
SWCL J231406.8+055204	15.3	55.4	0.646	0.123	1.51	1.69	9.8	42643	110119a
SWCL J231733.7+322828	20.4	41.2	0.575	0.085	1.33	2.33	6.9	79533	111215a
SWCL J232244.2+055601	26.3	50.7	0.606	0.064	1.37	1.22	11.6	148444	050803
SWCL J232248.4+054810	27.3	142.6	9.570	0.215	21.59	1.43	4.6	206593	050803
SWCL J232308.0−313440	16.0	38.9	0.528	0.075	0.99	2.19	7.1	92945	051001
SWCL J232345.5−313047	12.4	57.7	2.157	0.145	4.07	2.12	3.7	102308	051001
SWCL J232647.4+263614	17.2	38.9	0.614	0.088	1.36	1.84	5.4	79577	100816a
SWCL J232717.2+263108	58.0	163.8	8.533	0.324	18.85	1.76	4.3	81285	100816a
SWCL J232725.6+263506	18.0	69.5	2.371	0.166	5.24	1.75	7.2	85762	100816a
SWCL J233009.3+264459	18.9	53.0	0.483	0.097	1.06	1.21	7.4	50913	070103
SWCL J233229.2−661835	25.0	29.5	0.182	0.031	0.37	1.46	9.8	187555	090926a
SWCL J233350.7−662758	18.3	31.8	0.269	0.040	0.55	1.47	8.6	164727	090926a
SWCL J233518.9−662143	27.0	81.3	2.267	0.138	4.65	1.25	7.7	118580	090926a
SWCL J233522.4−662335	11.2	41.2	0.961	0.151	1.97	2.43	8.7	41883	090926a

Swift Extended Source Name	Core Size (arcsec)	Extent (arcsec)	CR (ct/ks)	CR error (ct/ks)	Flux (10^{-17} W/m^2)	Bkg Flux (0.36/s/deg^2)	Off (arcmin)	Exp (s)	GRB Date
SWCL J233616.8−313629	81.1	206.2	41.257	0.961	77.92	2.05	4.4	44660	071028b
SWCL J233942.0+314932	24.7	57.7	0.557	0.101	1.27	1.52	8.2	54222	071025
SWCL J234043.1+314455	14.9	55.4	0.724	0.117	1.65	1.51	5.9	52833	071025
SWCL J234545.0−655056	11.8	46.0	0.774	0.143	1.58	1.81	9.8	37873	110319a
SWCL J234624.4+001915	11.9	48.3	2.360	0.453	4.96	1.75	12.6	11487	080810
SWCL J234627.1−655917	14.4	46.0	0.934	0.145	1.91	1.86	2.2	44355	110319a
SWCL J234709.8+002852	18.6	55.4	0.732	0.116	1.54	1.30	12.8	54641	080810
SWCL J234757.5+002121	16.8	48.3	0.642	0.103	1.35	1.42	12.2	61117	080810

Table 2.1: Table 4 from Dai et al. (2015). Details on extended sources in SACS, including position, core size, extent on the sky, soft count rate and uncertainty, soft X-ray flux, background count rate, off-axis angle, exposure time, and XRT GRB field name (the date the event was observed). Units are given in parenthesis.

2.3 SDSS Data

SDSS DR8 provides the optical data for this study. The publicly available data covers 14,555 deg^2 and has magnitude limits of $m_{lim} < 22.0$, 22.2, 22.2, 21.3 and 20.5 mag for the u, g, r, i, and z bands respectively (Adelman-McCarthy et al., 2007; Aihara et al., 2011). Of the 442 cluster candidates, 209 are nominally in the SDSS DR8 footprint. However, six candidates lie too close to the survey edges and were not considered further (see Figure 2.10), to leave us with 203 candidates in the sample. We downloaded catalogs of the positions, magnitudes, photometric redshifts, and available spectroscopic redshifts for all galaxies within a $40'$ radius of the cluster candidate centers to provide both source and background regions. A small fraction of these regions are incomplete in coverage due to either being on the edge of the SDSS sky coverage, bright object masks or cosmic ray masks (we discuss these in detail in Section 2.5.2).

2.4 The Method

We searched for galaxy over-densities in three-dimensional space using the galaxy positions and photometric redshifts provided by SDSS DR8. Where available, spectroscopic redshifts are used in place of the photometric redshifts. For each cluster candidate, we considered source regions with radii of $2'$ and $3'$ centered on the X-ray centroid. We then selected the galaxies within the prescribed source regions and separated them into redshift bins of width $\Delta z = 0.05$. The SDSS

photometric redshifts include uncertainties, which have an average of ~ 0.12 (Aihara et al., 2011), larger than this bin size; however, the accuracy of the cluster redshift is improved by $\sqrt{N_{Net}}$ and is typically smaller than $\Delta z = 0.05$, where N_{Net} is the number of galaxies above the background in the $2'$ or $3'$ source region and within the redshift bin. We search for over-densities by comparing this redshift distribution to that of the local background. We measured the local background in an annulus extending from $25'$ to $40'$ and centered on the *Swift* sources, where the inner radius was chosen to be sufficiently distant from the cluster regions to avoid contamination from the cluster. Local backgrounds are needed in our analysis due to cosmic variance and any non-uniformity in the exposure depth. An example of this variability can be seen in Figure 2.10 where there is a distinct difference in the galaxy density between SWCL J215423.1 (top left) and SWCL J015021.7 (top right). From the background annulus of each source, we chose 100 random regions equal in size to the source region (so with radii of $2'$ or $3'$) and calculated the mean and standard deviation of the galaxy count in each redshift bin. This Monte-Carlo approach is more general because it does not assume background distributions simply described by Poisson fluctuations.

We compare the average background count and its standard deviation per redshift bin to the redshift distribution of the source region. We consider an over-density peak significant if the number of galaxies in a redshift bin is 3σ above the averaged background and if the galaxy count is at least seven. Setting a minimum galaxy count is important to reduce the false positives for higher

redshift clusters ($z \gtrsim 0.6$), where the number of detected galaxies is low so that the standard deviation is rather small, and the 3σ cut can be affected more by systematic uncertainties, such as the incompleteness of galaxies in SDSS for higher redshifts. For potential clusters with multiple over-density peaks, we select the most significant redshift bin for that candidate. If the original distribution did not pick up a significant over-density peak, we shift all of the distribution bins to the left by 0.025 and search for over-density peaks as before. Using this method, we search at most 40 redshift bins of width $\Delta z = 0.05$ for each cluster candidate. Since all of our optically confirmed clusters are below $z = 0.8$, we essentially have at most 32 redshift bins for detection. For the 203 cluster candidates, the expected number of 3σ false positives is $32 * 203 * 0.0015 \lesssim 9$ or approximately 9% of the identifications. The cluster redshift is determined by averaging the galaxy redshifts in the over-density bin. However, this includes foreground and background galaxies in the bin so the cluster redshifts determined favor the center of the over-density bin. To measure a more accurate cluster redshift, we shift the center of the bin ± 0.025 using increments of 0.001. For each case, we perform the same method as before. We keep the most significant over-density as the best redshift estimate and report cluster details in Table 2.2. This maximizes the likelihood of our method detecting accurate redshifts while maintaining a low number of tests to minimize the number of false positives.

Our results are listed in Table 2.2, where '...' indicates cases where no 3σ peak was detected for either the $2'$ or $3'$ source region sizes. We confirm SDSS over-density peaks for 104 of the 203 cluster candidates in the SDSS footprint. This

does not mean that the remaining 105 are not clusters because the SDSS data are only deep enough to confirm $z \lesssim 0.4$ clusters consistently. Examples of our SDSS cluster confirmation for two *Swift* XRT images of GRB060204b and GRB061110a are shown in Figures 2.4 and 2.5 , respectively. The blue circles mark the positions of the extended X-ray sources, and the galaxy redshift distributions for the *Swift* cluster candidates (red dashed lines) are shown in separate panels together with the local mean redshift distribution and the 3σ level above the local mean.

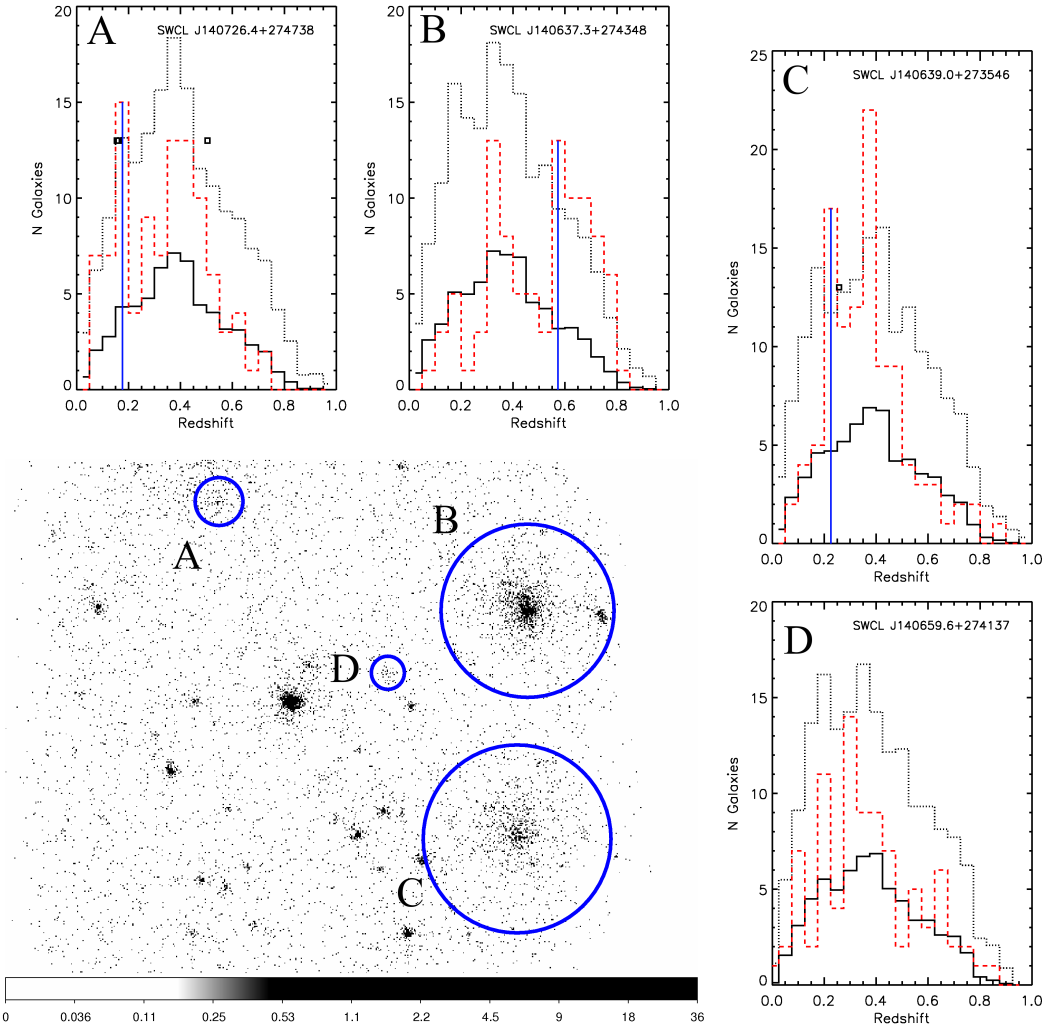


Figure 2.4: SDSS identification of *Swift* clusters in the GRB060204b field. (bottom left) The X-ray image with extended sources A−D indicated by the blue circles. (other panels) Photometric redshift distributions (red dashed line) of galaxies within $2'$ of source center are shown for the four labeled sources. Also shown are the averaged distribution of random positions of field galaxies (solid black line) along with 3σ above the average (dotted black line). The black squares indicate any SDSS spectroscopic redshifts for galaxies within the $2'$ region. The blue vertical lines indicate the confirmed redshifts. In this field, A is confirmed at $z = 0.174$ at a significance of 4.46σ, B is confirmed at $z = 0.600$ (5.34σ), C is confirmed at $z = 0.232$ (5.95σ), and D has no SDSS confirmation.

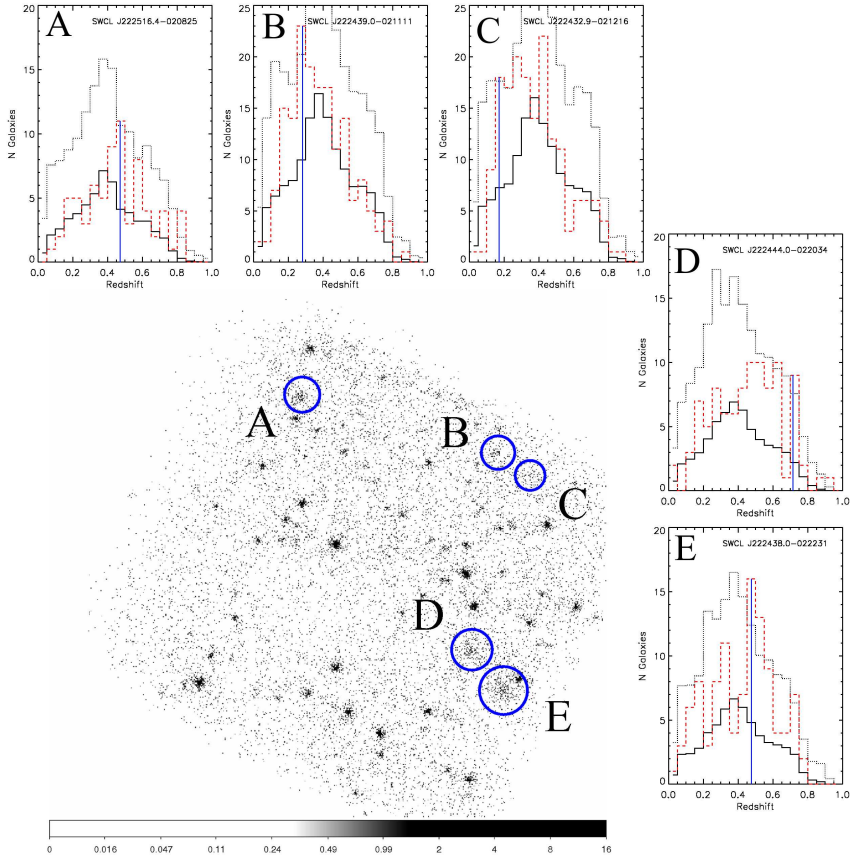


Figure 2.5: SDSS identification of *Swift* clusters in the GRB061110a field. (bottom left) The X-ray image with extended sources A−E indicated by the blue circles. (other panels) Photometric redshift distributions (red dashed line) of galaxies within $2'$ (A,D,E) and within $3'$ (B,C) of source center are shown for the five labeled sources. Also shown are the averaged distribution of random positions of field galaxies (solid black line) along with 3σ above the average (dotted black line). The blue vertical lines indicate the confirmed redshifts. In this field, A is confirmed at $z = 0.467$ at a significance of 3.56σ, B is confirmed at $z = 0.292$ (5.16σ), C is confirmed at $z = 0.162$ (4.00σ), D is confirmed at $z = 0.714$ (3.84σ), and E is confirmed at $z = 0.499$ (6.44σ).

Swift Cluster Candidate Name	2′ Reg. Conf. z	3′ Reg. Conf. z	Conf. Phot. z	Conf. σ	N_{Net}	N_{opt}	BCG r_{mag}	BCG r_{abs}	Offset (Mpc)	L_X (erg/s)	M_{500} ($M_\odot$)
SWCL J002111.4+210438	0.674	...	0.674	4.14	5.99	186.68	21.84	−23.24	0.66	3.52e+44	4.96e+14
SWCL J002114.5+205943	0.141	0.074	0.141	6.08	6.82	13.19	16.94	−22.02	0.06	3.75e+43	1.75e+14
SWCL J002823.6+092705	0.195	0.215	0.195	7.09	13.06	22.54	17.82	−23.23	0.02	7.95e+43	2.71e+14
SWCL J003317.8+193925	...	0.246	0.246	3.17	3.41	7.98	19.85	−22.20	0.61	9.62e+43	2.95e+14
SWCL J005136.8+074351	...	0.757	0.757	3.90	2.32	432.92	19.26	−26.40	0.74	8.50e+43	1.94e+14
SWCL J012310.5+375549	0.749	0.762	0.762	4.52	2.37	521.41	22.29	−23.54	1.11	9.45e+43	2.06e+14
SWCL J015751.5+170139	...	0.529	0.529	4.85	6.20	52.61	20.66	−23.34	0.01	1.25e+44	2.89e+14
SWCL J015752.9+165933	0.510	0.525	0.510	5.30	10.00	50.36	20.38	−23.15	0.29	2.26e+44	4.22e+14
SWCL J015803.5+165005	0.223	0.233	0.223	7.46	11.91	20.55	16.95	−24.33	0.01	8.09e+43	2.69e+14
SWCL J020003.8+084024	0.196	...	0.196	4.10	6.96	12.48	16.24	−24.90	0.02	1.93e+44	4.70e+14
SWCL J020006.4+084454	0.419	...	0.419	4.01	8.73	26.16	19.07	−23.85	0.03	1.32e+44	3.21e+14
SWCL J025547.9+000902	0.573	0.570	0.573	4.00	7.71	78.20	20.89	−23.39	0.63	3.36e+44	5.17e+14
SWCL J025630.7+000601	0.374	0.391	0.374	15.49	45.33	112.34	18.22	−24.48	0.01	7.60e+43	2.35e+14
SWCL J035259.4−004338	0.413	0.301	0.301	3.77	7.32	23.86	18.59	−22.94	0.36	4.58e+44	7.51e+14
SWCL J054716.7+641156	0.271	0.369	0.369	6.19	10.37	44.17	19.36	−26.24	0.80	8.25e+43	2.48e+14
SWCL J075043.2+310400	0.378	0.375	0.378	4.69	14.16	33.79	19.16	−23.59	0.43	1.09e+44	2.94e+14
SWCL J075900.8+324449	0.579	0.751	0.579	3.70	7.53	75.21	21.99	−22.36	0.64	3.50e+44	5.28e+14
SWCL J075908.5+324237	0.722	...	0.722	3.99	5.85	481.81	21.15	−24.13	0.58	2.45e+44	3.83e+14
SWCL J080022.5−085931	...	0.273	0.273	3.98	4.25	11.45	18.94	−23.12	0.32	1.28e+44	3.47e+14
SWCL J082113.9+320018	0.746	0.728	0.746	7.58	9.09	859.00	21.16	−24.28	0.08	9.68e+44	8.86e+14
SWCL J083340.9+331118	0.682	0.675	0.682	8.42	18.06	673.84	20.66	−24.35	0.22	5.10e+44	6.21e+14
SWCL J084749.4+133142	0.391	0.391	0.391	7.40	21.23	55.50	19.41	−23.22	0.07	1.64e+45	1.56e+15
SWCL J084959.1+521711	0.201	...	0.201	3.95	8.00	13.75	18.95	−22.06	0.15	1.20e+44	3.48e+14
SWCL J085523.8+110202	0.317	...	0.317	4.50	10.88	20.82	19.67	−22.04	0.40	1.10e+44	3.07e+14
SWCL J085552.1+465925	0.477	...	0.477	4.01	7.77	29.24	19.67	−23.81	0.69	1.27e+44	3.02e+14
SWCL J085619.7+470018	0.479	0.474	0.479	3.53	6.41	23.93	20.27	−23.05	0.05	6.83e+43	2.05e+14
SWCL J090714.8+351020	0.218	0.212	0.218	5.08	10.73	17.49	17.18	−23.57	0.36	5.01e+43	2.00e+14
SWCL J092607.0+314854	0.268	...	0.268	3.44	8.54	14.40	18.95	−22.61	0.25	7.47e+43	2.49e+14

Swift Cluster Candidate Name	2′ Reg. Conf. z	3′ Reg. Conf. z	Conf. Phot. z	Conf. σ	N_{Net}	N_{opt}	BCG r_{mag}	BCG r_{abs}	Offset (Mpc)	L_X (erg/s)	M_{500} ($M_\odot$)
SWCL J092649.8+301346	0.570	0.567	0.567	5.33	7.64	84.84	18.86	−25.48	0.78	3.58e+44	5.40e+14
SWCL J092719.6+301348	0.396	0.331	0.331	4.25	9.07	25.43	18.31	−23.72	0.04	1.52e+44	3.71e+14
SWCL J092730.1+301046	0.303	...	0.303	4.41	10.72	20.16	19.05	−23.22	0.23	3.67e+44	6.54e+14
SWCL J092852.3+002137	0.535	0.091	0.091	4.09	4.32	13.27	16.91	−20.52	0.02	2.77e+43	1.50e+14
SWCL J093041.3+170400	0.320	...	0.320	4.88	10.96	20.56	20.00	−22.23	0.46	7.25e+43	2.36e+14
SWCL J093045.4+165930	0.180	0.177	0.180	5.84	9.58	15.81	17.07	−23.62	0.19	4.15e+43	1.82e+14
SWCL J095257.1+102440	0.400	0.398	0.400	4.07	11.79	29.35	18.83	−23.92	0.02	1.52e+44	3.55e+14
SWCL J095513.4+181215	0.423	0.421	0.423	4.57	11.61	33.60	19.54	−23.33	0.57	1.34e+44	3.23e+14
SWCL J095515.5+180357	0.745	0.747	0.745	8.29	11.16	962.85	20.37	−25.03	0.19	3.47e+44	4.68e+14
SWCL J101341.5+430651	0.400	0.400	0.400	4.09	11.11	26.72	18.30	−24.53	0.03	1.37e+44	3.34e+14
SWCL J111736.0+033711	0.403	0.400	0.403	4.40	12.78	35.37	19.67	−23.46	0.26	3.71e+44	6.17e+14
SWCL J113427.6−070208	0.239	0.304	0.239	5.02	10.36	17.31	17.44	−24.04	0.01	1.21e+44	3.41e+14
SWCL J114232.3+505623	0.254	...	0.254	3.47	9.06	15.30	16.77	−24.81	0.02	8.59e+43	2.74e+14
SWCL J114503.1+600811	0.268	0.262	0.268	5.61	14.15	23.77	18.31	−23.34	0.01	5.52e+43	2.06e+14
SWCL J114553.0+595320	...	0.546	0.546	4.53	4.85	45.29	21.27	−22.63	0.36	1.39e+44	3.04e+14
SWCL J115811.3+452903	0.389	0.407	0.389	6.05	17.12	39.64	18.39	−24.48	0.22	1.04e+44	2.83e+14
SWCL J120137.8+104936	0.277	0.745	0.277	3.37	7.66	13.36	17.82	−23.78	1.16	1.39e+44	3.63e+14
SWCL J121628.2+353820	0.347	0.358	0.358	4.52	8.68	25.13	19.57	−23.74	0.81	1.12e+44	3.03e+14
SWCL J121711.8+353745	0.492	0.472	0.492	3.89	8.83	37.41	20.33	−23.00	0.25	2.30e+44	4.32e+14
SWCL J123313.9+210217	0.516	0.516	0.516	6.51	13.68	69.95	19.74	−24.07	0.11	2.26e+44	4.20e+14
SWCL J123612.4+290222	0.104	0.105	0.104	5.21	7.07	16.07	16.09	−23.29	0.21	7.48e+43	2.75e+14
SWCL J124308.5+170639	0.722	0.145	0.145	6.12	7.85	17.97	15.52	−25.00	0.30	3.71e+43	1.74e+14
SWCL J124312.1+170454	0.132	0.136	0.136	6.84	7.23	16.93	15.52	−24.99	0.20	5.65e+43	2.27e+14
SWCL J125957.2+155717	0.700	0.685	0.700	4.74	6.82	296.56	21.28	−23.71	0.62	2.83e+44	4.25e+14
SWCL J130332.1+591556	0.218	0.147	0.218	4.81	9.70	15.75	17.37	−23.56	0.42	1.06e+44	3.20e+14
SWCL J130911.8+611521	0.253	...	0.253	3.67	7.88	13.44	12.55	−29.00	0.01	8.34e+43	2.69e+14
SWCL J130959.1+612530	0.248	0.247	0.248	6.19	12.52	20.77	17.85	−23.44	0.04	1.05e+44	3.12e+14
SWCL J131521.9+164155	0.342	0.242	0.242	4.79	5.97	13.81	16.35	−24.70	0.01	3.78e+44	6.93e+14

Swift Cluster Candidate Name	2′ Reg. Conf. z	3′ Reg. Conf. z	Conf. Phot. z	Conf. σ	N_{Net}	N_{opt}	BCG r_{mag}	BCG r_{abs}	Offset (Mpc)	L_X (erg/s)	M_{500} ($M_\odot$)
SWCL J133051.0+420641	0.597	0.588	0.588	4.93	6.65	86.40	20.37	−23.82	0.60	1.70e+44	3.35e+14
SWCL J133055.8+420015	...	0.113	0.113	3.92	4.31	11.24	14.57	−23.36	0.00	1.13e+44	3.54e+14
SWCL J135914.0+470528	0.526	0.527	0.526	8.86	17.97	95.73	20.55	−23.32	0.28	1.03e+44	2.56e+14
SWCL J140637.3+274348	0.600	0.758	0.600	5.34	10.78	125.86	20.08	−24.41	0.17	1.35e+45	1.20e+15
SWCL J140639.0+273546	0.232	0.233	0.232	5.95	14.44	24.57	18.37	−22.67	0.07	1.39e+44	3.75e+14
SWCL J140726.4+274738	0.177	0.174	0.174	4.46	10.17	22.41	16.06	−24.26	0.01	7.85e+43	2.72e+14
SWCL J140907.4+242406	0.566	0.579	0.566	4.66	9.67	72.16	20.32	−23.58	0.44	1.24e+44	2.80e+14
SWCL J141221.8+165216	0.571	0.438	0.571	4.32	7.80	65.16	21.09	−23.32	0.43	2.25e+44	4.04e+14
SWCL J143211.6+362225	0.663	0.623	0.663	4.75	9.94	225.21	21.34	−23.47	0.11	1.63e+44	3.10e+14
SWCL J144209.2+333414	0.451	0.638	0.638	6.42	6.84	151.86	22.04	−23.64	0.85	3.31e+44	4.90e+14
SWCL J144604.5+203334	0.275	...	0.275	3.19	6.77	12.01	19.09	−22.68	0.17	8.84e+43	2.75e+14
SWCL J151550.9+442056	0.270	0.109	0.109	5.44	7.48	19.24	16.39	−23.00	0.02	1.04e+44	3.36e+14
SWCL J152252.9+253527	0.546	0.626	0.546	7.20	13.06	89.91	19.59	−24.67	0.01	5.83e+44	7.41e+14
SWCL J152316.4+254754	...	0.796	0.796	7.60	3.03	1156.89	21.59	−24.16	0.84	1.12e+44	2.24e+14
SWCL J155117.4+445118	0.697	...	0.697	5.66	9.43	328.74	21.99	−22.95	0.58	3.76e+44	5.09e+14
SWCL J155159.8+445748	0.213	0.207	0.213	6.23	12.02	20.09	16.60	−24.27	0.01	7.90e+43	2.67e+14
SWCL J155555.3+410548	0.368	...	0.368	5.10	14.71	32.07	18.17	−24.29	0.01	3.32e+44	5.89e+14
SWCL J155708.6+354100	0.429	0.440	0.429	4.20	10.80	30.22	19.66	−23.50	0.15	1.10e+44	2.85e+14
SWCL J155743.3+353020	0.166	0.161	0.166	35.68	54.31	97.45	15.91	−24.56	0.04	8.77e+44	1.22e+15
SWCL J160637.5+321351	0.065	0.058	0.065	5.22	7.27	25.61	16.22	−22.02	0.14	7.15e+43	2.73e+14
SWCL J160956.9+301052	0.114	0.276	0.114	4.64	10.02	21.14	17.66	−21.55	0.17	4.36e+43	1.95e+14
SWCL J164637.4+363021	...	0.077	0.077	3.54	2.93	9.67	17.39	−21.02	0.17	2.12e+43	1.28e+14
SWCL J164956.4+313021	0.734	...	0.734	4.82	8.39	617.61	21.73	−23.83	0.59	4.32e+44	5.41e+14
SWCL J170542.2+112451	...	0.409	0.409	3.69	6.25	25.12	19.83	−23.19	0.59	3.12e+44	5.52e+14
SWCL J170716.1+235208	0.084	0.085	0.085	4.83	4.79	15.17	20.35	−22.59	0.28	3.88e+43	1.85e+14
SWCL J170757.1+235135	0.212	0.213	0.212	6.34	10.28	17.97	17.64	−23.43	0.01	2.47e+44	5.42e+14
SWCL J172011.1+692315	0.470	0.270	0.270	4.90	6.77	15.61	20.80	−22.34	0.72	6.44e+43	2.27e+14
SWCL J200031.1+085259	...	0.047	0.047	3.94	3.28	2.21	18.63	−19.87	0.15	8.29e+41	1.73e+13

Swift Cluster Candidate Name	2′ Reg. Conf. z	3′ Reg. Conf. z	Conf. Phot. z	Conf. σ	N_{Net}	N_{opt}	BCG r_{mag}	BCG r_{abs}	Offset (Mpc)	L_X (erg/s)	M_{500} ($M_\odot$)
SWCL J215411.4−001127	0.381	0.214	0.381	6.14	14.54	41.65	20.52	−21.98	0.20	1.69e+44	3.84e+14
SWCL J215411.6−000654	0.213	0.106	0.106	3.68	2.77	7.72	18.60	−20.85	0.10	4.34e+43	1.96e+14
SWCL J215413.2+000413	0.227	0.166	0.227	4.60	10.58	18.72	17.67	−23.65	0.04	1.70e+44	4.25e+14
SWCL J215423.1+000526	0.169	0.170	0.169	8.58	15.76	28.35	16.10	−24.23	0.07	1.64e+44	4.31e+14
SWCL J215520.0−001115	0.373	0.371	0.371	3.83	7.08	26.74	19.81	−23.70	0.85	1.16e+44	3.06e+14
SWCL J222432.9−021216	0.204	0.162	0.162	4.00	5.54	13.21	18.57	−21.52	0.25	4.69e+43	1.99e+14
SWCL J222438.0−022231	0.499	0.496	0.499	6.44	13.73	71.02	19.91	−23.83	0.06	1.83e+44	3.72e+14
SWCL J222439.0−021111	...	0.292	0.292	5.16	8.99	24.41	18.44	−23.89	0.56	4.75e+43	1.85e+14
SWCL J222444.0−022034	0.714	0.718	0.714	3.84	6.71	546.21	22.08	−23.29	0.44	2.81e+44	4.20e+14
SWCL J222506.2−020611	0.524	...	0.524	3.45	6.35	40.70	20.50	−23.20	0.75	1.47e+44	3.20e+14
SWCL J222516.4−020825	0.467	0.585	0.467	3.56	8.61	34.29	20.42	−22.99	0.60	1.74e+44	3.69e+14
SWCL J222954.1+194350	0.287	0.290	0.287	7.65	15.63	28.27	18.00	−23.63	0.03	1.12e+44	3.15e+14
SWCL J224206.9+233408	0.402	...	0.402	5.38	13.98	40.30	19.40	−23.76	0.13	3.19e+44	5.61e+14
SWCL J231257.7+182543	0.325	0.548	0.325	3.83	8.73	21.26	19.98	−22.50	0.54	1.07e+44	2.99e+14
SWCL J231733.7+322828	0.400	0.376	0.400	4.35	13.24	37.54	19.32	−23.25	0.07	1.61e+44	3.67e+14
SWCL J232244.2+055601	0.235	...	0.235	4.18	7.80	13.89	17.51	−24.04	0.31	5.55e+43	2.11e+14
SWCL J232248.4+054810	0.320	0.244	0.244	5.92	9.94	23.97	16.85	−24.56	0.01	1.72e+44	4.24e+14
SWCL J232717.2+263108	0.223	0.223	0.223	11.50	13.29	31.74	16.85	−24.33	0.05	1.41e+44	3.80e+14
SWCL J232725.6+263506	0.257	0.227	0.257	5.71	8.79	16.05	17.99	−23.13	0.38	1.72e+44	4.21e+14
SWCL J233009.3+264459	...	0.522	0.522	3.68	4.00	36.17	19.82	−23.99	0.56	1.07e+44	2.64e+14

Table 2.2: SDSS confirmations of *Swift* cluster candidates. Non-detections are labeled with '...'. Cases where neither source region size confirmed a redshift are not included in this table. Cases where the 2′ and 3′ regions' redshifts differ are discussed in Section 2.4. N_{Net} is the number of galaxies above the background for the detected redshift bin. N_{opt} is the estimated optical richness, described in Section number 2.6.3. We list the BCG SDSSr apparent magnitude, the calculated absolute magnitude (r_{abs}) and the BCG-to-X-ray offset in Mpc. L_X is the X-ray bolometric luminosity and M_{500} is a virialized mass estimate.

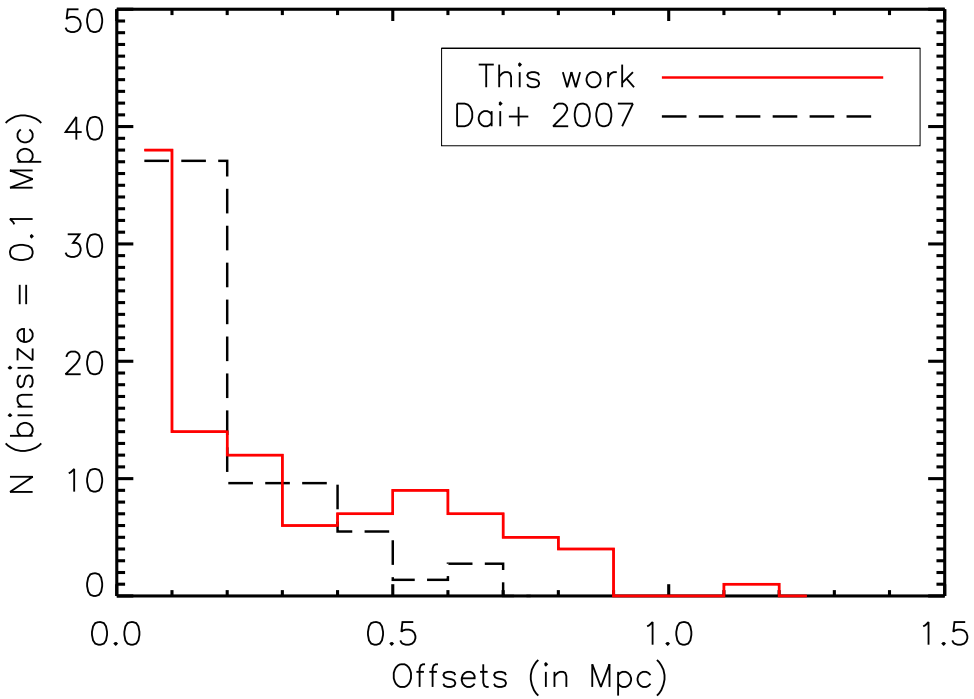


Figure 2.6: Offsets between BCGs and the X-ray source centers for the 104 confirmed clusters (red, solid line). For comparison, the black, dashed line is the result from Dai et al. (2007), normalized to our study.

For each candidate with a confirmed over-density peak, we measure the distance between the BCG and the X-ray source center, and calculate the distribution of the physical offsets (in Mpc) between the BCG and the X-ray source center (Figure 2.6). We select the BCG as the galaxy with the brightest SDSS $r-$band magnitude in the source region and the $\Delta z = 0.05$ redshift bin. In Table 2.2, we list the SDSS $r-$band apparent and absolute magnitudes of the BCGs and their physical offsets to their corresponding X-ray centers. It is often assumed that both BCGs and X-ray centroids define the center of the cluster potential wells and thus, their locations should overlap. However, in studies of optically selected galaxy groups it has been found that the brightest halo galaxies can be satellite galaxies instead of central galaxies (e.g., Skibba et al. 2011; Weinmann et al. 2006; van den Bosch et al. 2008; Pasquali et al. 2009). Skibba et al. (2011) also found that the number of brightest halo galaxies that were not central increased when studying a higher group mass bin. We show our calculated mass (details in Section 2.6.2) versus BCG-to-X-ray offset in Figure 2.7 and find the opposite to be true for our sample, that higher mass clusters have low BCG offsets. The BCG-to-X-ray centroid distance distribution exhibits a broad tail extending from a compact core (e.g., Lin & Mohr 2004; von der Linden et al. 2007; Dai et al. 2007). We compare our offset distribution with that of 2MASS clusters (Dai et al., 2007), which is normalized to match our sample count, and find that the distributions are similar.

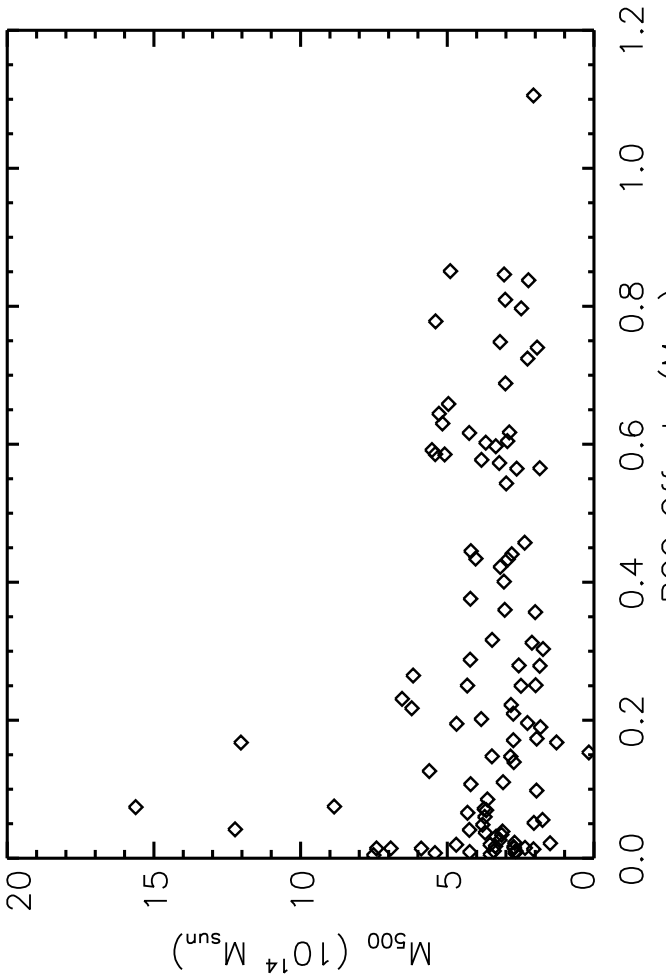


Figure 2.7: Mass versus BCG offsets for the 104 confirmed clusters.

Of the 104 confirmed clusters, there are 73 cases where our method found SDSS galaxy over-densities for both the $2'$ and $3'$ regions. 70% of these cases agree within the redshift range $\delta z \lesssim 0.05$, where we assigned the more significant peak as the redshift of the cluster. The twenty-four cases where the $2'$ and $3'$ regions both detect an over-density peak but the peaks are located in different redshift bins are listed in Table 2.3. We compared both the significance of the over-density peak and the BCG-to-X-ray center offset (in Mpc) for both possibilities and assign a score as $(\sigma_2 - \sigma_3)/3 - (\mathrm{Offset}_2 - \mathrm{Offset}_3)/\mathrm{Mpc}$ for each cluster in Table 2.3. If the score is positive (negative) then we assign the redshift to that measured by the $2'$ ($3'$) region. The final assigned redshifts are shown in bold in Table 2.3.

Swift Name	z_2	z_3	σ_2	σ_3	Offset$_2$	Offset$_3$	Score
SWCL J002114.5+205943	**0.141**	0.074	6.075	5.425	0.056	0.108	0.269
SWCL J035259.4−004338	0.413	**0.301**	4.398	3.775	0.358	0.004	−0.145
SWCL J054716.7+641156	0.271	**0.369**	3.193	6.190	0.282	0.797	−0.485
SWCL J075900.8+324449	**0.579**	0.751	3.696	3.017	0.644	0.838	0.421
SWCL J092719.6+301348	0.396	**0.331**	3.717	4.255	0.522	0.037	−0.664
SWCL J092852.3+002137	0.535	**0.091**	3.443	4.092	0.604	0.022	−0.799
SWCL J113427.6−070208	**0.239**	0.304	5.024	4.663	0.010	0.013	0.122
SWCL J120137.8+104936	**0.277**	0.745	3.367	4.565	0.085	1.159	0.675
SWCL J124308.5+170639	0.722	**0.145**	3.898	6.120	0.601	0.303	−1.038
SWCL J130332.1+591556	**0.218**	0.147	4.808	4.112	0.422	0.332	0.142
SWCL J131521.9+164155	0.342	**0.242**	5.038	4.786	0.533	0.014	−0.435
SWCL J140637.3+274348	**0.600**	0.758	5.342	4.929	0.168	0.545	0.515
SWCL J141221.8+165216	**0.571**	0.438	4.325	3.997	0.434	0.860	0.535
SWCL J144209.2+333414	0.451	**0.638**	3.256	6.423	0.314	0.851	−0.519
SWCL J151550.9+442056	0.270	**0.109**	3.903	5.444	0.152	0.017	−0.648
SWCL J152252.9+253527	**0.546**	0.626	7.201	5.655	0.014	0.015	0.516
SWCL J160956.9+301052	**0.114**	0.276	4.639	3.975	0.173	0.362	0.410
SWCL J172011.1+692315	0.470	**0.270**	3.066	4.902	0.695	0.724	−0.583
SWCL J215411.4−001127	**0.381**	0.214	6.142	4.248	0.202	0.446	0.876
SWCL J215411.6−000654	0.213	**0.106**	3.542	3.680	0.211	0.098	−0.159
SWCL J215413.2+000413	0.227	**0.166**	4.597	8.218	0.041	0.460	−0.788
SWCL J222516.4−020825	**0.467**	0.585	3.564	3.523	0.602	0.996	0.407

Swift Name	z_2	z_3	σ_2	σ_3	Offset_2	Offset_3	Score
SWCL J231257.7+182543	**0.325**	0.548	3.832	3.597	0.543	0.530	0.065
SWCL J232248.4+054810	0.320	**0.244**	4.636	5.925	0.080	0.009	−0.501

Table 2.3: z_2, z_3: redshifts confirmed by the $2'$ and $3'$ regions respectively, bold represents the final redshift determined for that candidate. σ_2, σ_3: standard deviations above the average. Offset_2, Offset_3: offsets in Mpc between BCG and X-ray source's center. Score $= (\sigma_2 - \sigma_3)/3 - (\text{Offset}_2 - \text{Offset}_3)/\text{Mpc}$. If Score $>$ ($<$) 0 then $2'$ ($3'$) region confirmed.

2.5 Special Cases

In this section, we discuss the situation where multiple *Swift* cluster candidates are closely located in angular position and redshift space and check for complications in the SDSS confirmation method. We also discuss how we treat clusters with incomplete SDSS coverage of either the source or background areas.

2.5.1 Close Pairs of *Swift* Cluster Candidates

We found four cases with *Swift* cluster candidate pairs within $6'$ of each other and with similar redshifts ($\delta z \lesssim 0.05$). With the possibility of overlapping source regions, these could result in false positive detections or redshift mis-assignments and thus require a closer examination. For each case, we compare the following for the cluster properties in question: the significance of the over-density peak, confirmation using the other source region size (so either $2'$ or $3'$), the BCG−to−X-ray offset, any other redshift peaks over 3σ (i.e. multiple peaks), and both X-ray images and galaxy positions. We list the conclusions of our analysis in Table 2.4, and show two examples in Figures 2.8 and 2.9, where we also include a discussion of our conclusions in the figure captions.

SWCL J215423.1 and SWCL J215413.2 are separated by a distance of $2\farcm7$ and both have a high significance peak ($> 6\sigma$) around $z \sim 0.17$, and SWCL J215413.2 has a second galaxy over-density peak at $z = 0.227$ (with significance $\sigma = 4.60$). It is likely that the $z \sim 0.17$ peak for SWCL J215413.2 is contaminated by the cluster members of SWCL J215423.1. We assign $z = 0.169$ for SWCL J215423.1

and $z = 0.227$ for SWCL J215413.2.

SWCL J232717.2 and SWCL J232725.6 are separated by a distance of 4.′4 and both have a high significance peak ($> 6\sigma$) at $z \sim 0.22$, and SWCL J232725.6 has a second galaxy over-density peak at $z = 0.257$ (with significance $\sigma = 5.71$). It is likely that the $z \sim 0.22$ peak for SWCL J232725.6 is contaminated by the cluster members of SWCL J232717.2. We assign $z = 0.223$ for SWCL J232717.2 and $z = 0.257$ for SWCL J232725.6 (Figure 2.8).

In the remaining two cases, there are no additional over-density peaks in either of the close pairs. For the SWCL J092730.1 and SWCL J092719.6 pair, we detected over density peaks at $z \sim 0.396$ ($z \sim 0.331$) using $2'$ ($3'$) source size regions for SWCL J092719.6, but only a peak at $z \sim 0.303$ using $2'$ region for SWCL J092730.1. Further examining the BCG offsets, significance of the peaks and the X-ray images, we determine that both are clusters, possibly merging. We reach a similar conclusion for the SWCL J085552.1 and SWCL J085619.7 pair (Figure 2.9).

Name 1	Name 2	Distance	z_1	z_2	σ_1	σ_2	BCG_1	BCG_2	Multiple peak?	Conclusion
SWCL J085552.1	SWCL J085619.7	4.799	0.477	0.479	4.01	3.53	0.694	0.050	no	1: cluster at 0.477, 2: $z = 0.479$
SWCL J092730.1	SWCL J092719.6	3.795	0.303	0.331	4.41	4.25	0.254	0.036	no	1: cluster at $z = 0.303$, 2: $z = 0.331$
SWCL J215423.1	SWCL J215413.2	2.745	0.169	0.166	8.58	8.22	0.063	0.449	yes	1: strong cluster at 0.169, 2: $z = 0.227$
SWCL J232725.6	SWCL J232717.2	4.378	0.227	0.223	6.42	11.50	0.328	0.048	yes	1: cluster at $z = 0.257$, 2: strong cluster at $z = 0.223$

Table 2.4: Close contaminations are defined to be the cases where the X-ray source centers are within $6'$ and the difference in redshifts is $\delta z \lesssim 0.05$. Distances are given in arcminutes and the BCG offsets are given in Mpc. We discuss this more in Section 2.5.1.

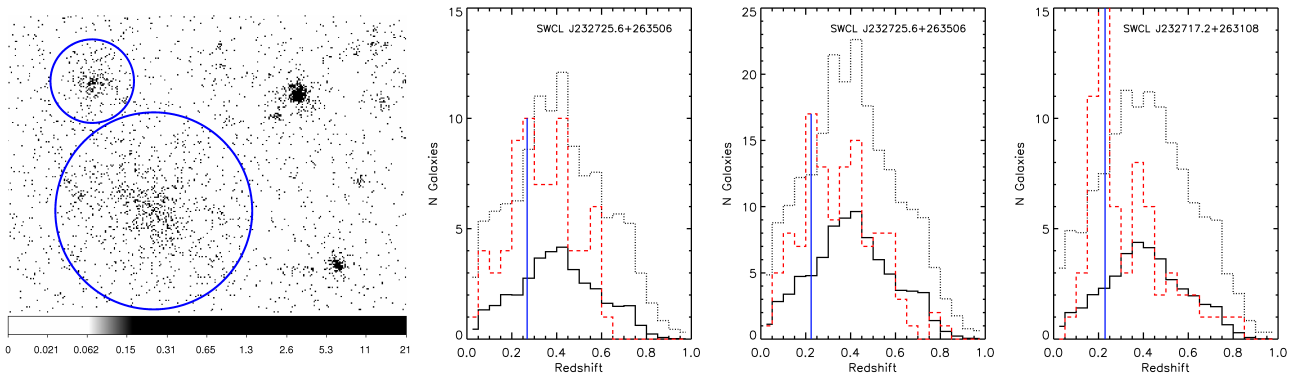


Figure 2.8: An example of nearby contamination. Left: the *Swift* X-ray image. SWCL J232725.6 (upper source, left middle: 2′ detection, right middle: 3′ detection) and SWCL J232717.2 (lower source, right panel, 3′ detection) have centers that are 4.38′ apart. Both source size regions for SWCL J232717.2 detected a galaxy cluster at $z \sim 0.223$ and the 3′ source size region for SWCL J232725.6 detected a cluster at $z \sim 0.227$. SWCL J232725.6 also detected a galaxy cluster at 0.257 via 2′ detection. We determine the 3′ confirmation for SWCL J232725.6 is contamination and that SWCL J232725.6 is a cluster at $z \sim 0.257$.

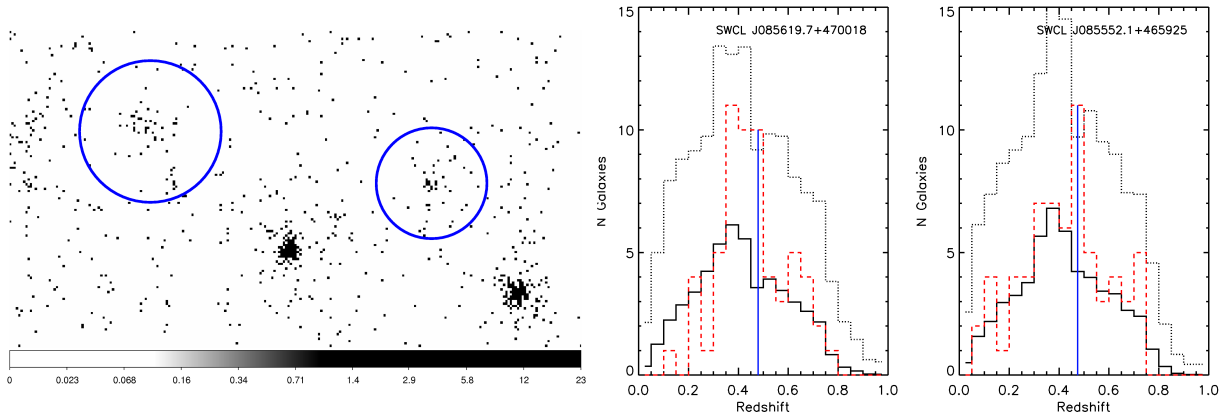


Figure 2.9: An example of nearby contamination. Left: the *Swift* X-ray image. SWCL J085619.7 (middle panel, left source) and SWCL J085552.1 (right panel, right source) have centers that are 4.8′ apart. The 2′ source size region for SWCL J085552.1 and the 2′ and 3′ source size regions for SWCL J085619.7 all have significant over-density peaks at $z \sim 0.48$. The distributions from the 2′ regions are shown here. We conclude that SWCL J085619.7 and SWCL J085552.1 are both clusters.

2.5.2 Incomplete SDSS Coverage

If a cluster candidate is close to the edge of the SDSS footprint, then the $40'$ region surrounding the X-ray source's center will appear to be artificially devoid of galaxies. In addition, there are masking regions associated with bright sources and cosmic rays in the images. To check for coverage completeness for each candidate cluster, the galaxy distribution within $40'$ of X-ray source center was visually inspected.

Eight of the candidates have incomplete $3'$ source regions as shown in Figure 2.10. Each dot represents a galaxy, the blue solid circles represent the $2'$ regions and the red dashed circles represent the $3'$ regions, indicating the largest source region size considered in our analysis. Two of the eight cases (c and g of Figure 2.10) have complete $2'$ source regions and thus, are mostly complete in SDSS and are included in this study. The other six incomplete source regions shown in Figure 2.10 are excluded from this study. We are examining these cases by performing our own follow-up observations. This lead to the exclusion of 6 candidates (SWCL J012302.8, SWCL J020934.7, SWCL J032216.0, SWCL J075036.6, SWCL J173932.6 and SWCL J194530.3), as discussed earlier in Section 2.3.

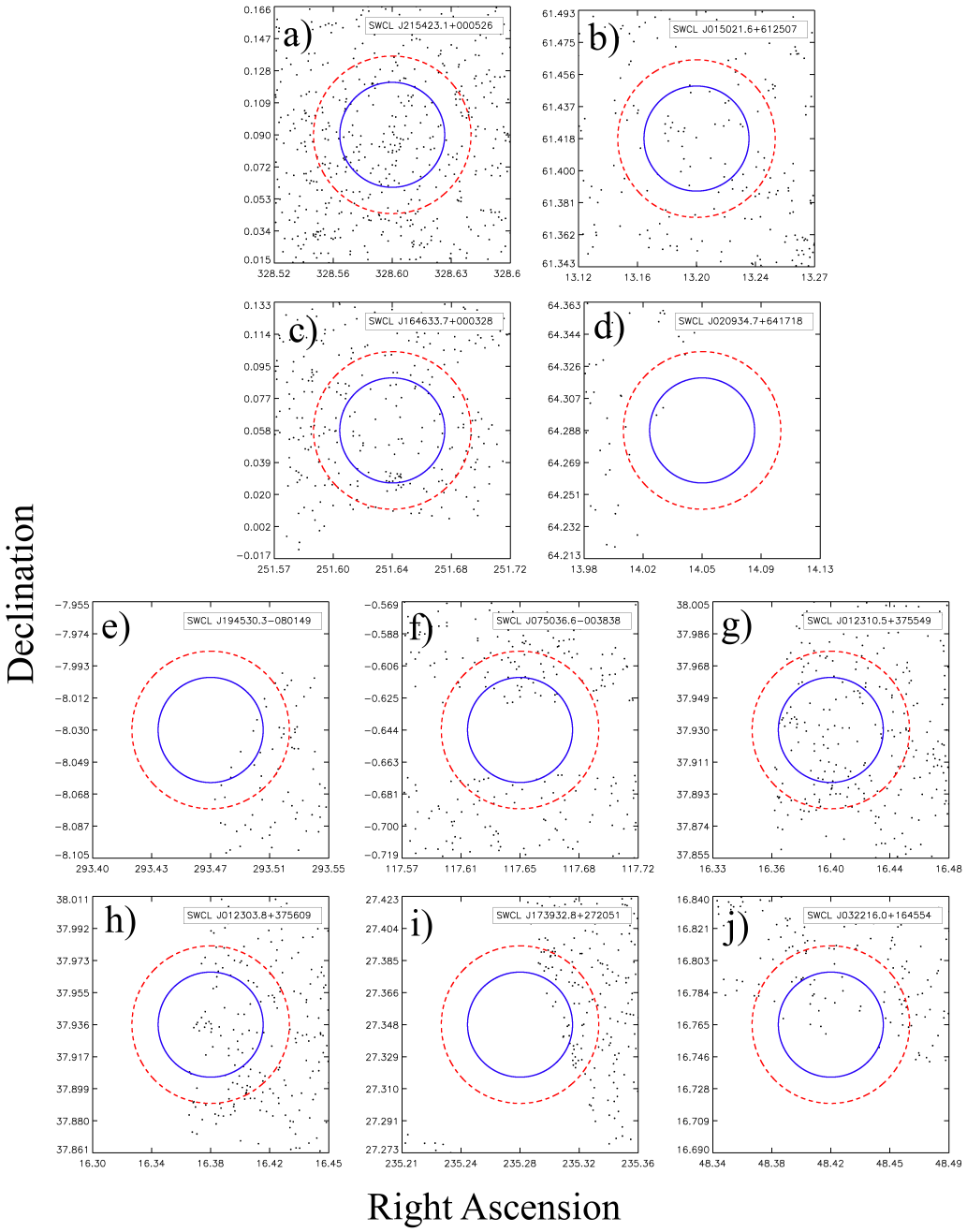


Figure 2.10: Distributions of SDSS galaxies relative to source regions. Each dot is a galaxy and the source regions are indicated by the red, dashed lines (3′ radius) and blue, solid lines (2′ radius). The top row (a and b) shows examples of cluster candidates with complete source regions in SDSS DR8. The remaining cases show various degrees of incompleteness: c and g are complete for the 2′ region and thus are included in the survey. The remaining six are too incomplete and are rejected from the survey, so that the number of cluster candidates in this survey is 203.

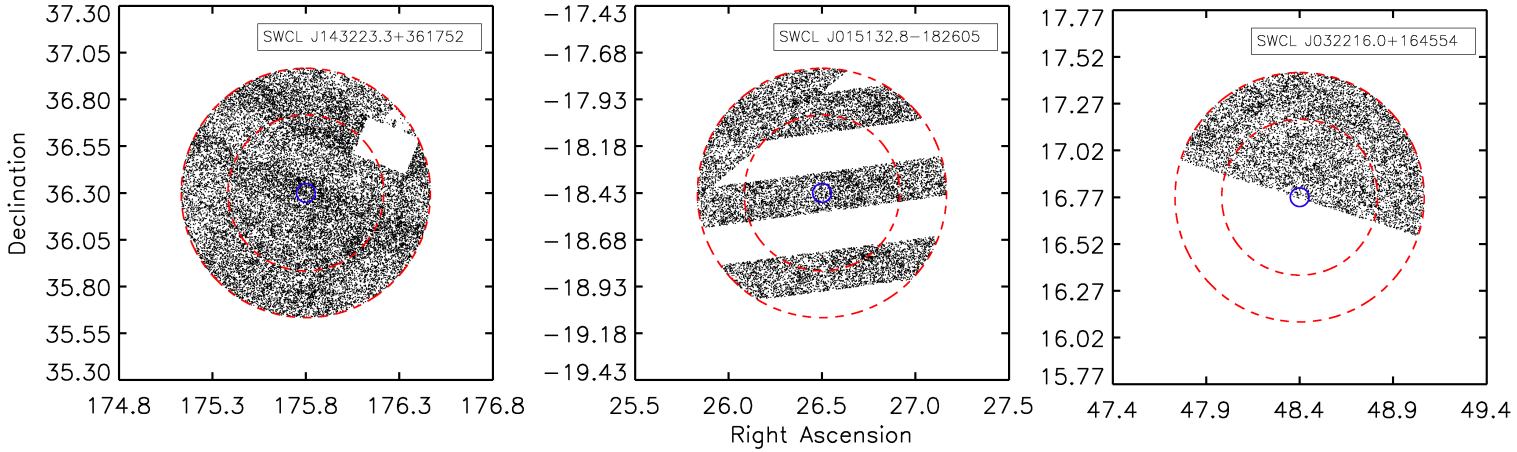


Figure 2.11: Incomplete backgrounds of SDSS fields. Each dot is a galaxy, the blue, solid circle represents the $3'$ region and the red, dashed circles encompass the background annulus from $25'$ to $40'$. Left: an example of background that is $\geq 90\%$ complete. Middle, Right: Examples of background regions that are $> 10\%$ incomplete.

There are 33 candidates with incomplete background annuli, and Figure 2.11 shows a few examples. Other examples of incomplete backgrounds are similar in shape and incompleteness to those that are shown. Each dot represents a galaxy, the blue solid circles are $3'$ regions containing the source, and the red dashed circles denote the background annulus with inner and outer radii $25'$ and $40'$. Since we consider 100 random regions to calculate the average local background and variance, the incomplete background causes the average count of galaxies to artificially decrease and the variance significantly increases. For these 33 cluster candidates, we considered 100 random regions that exclude the incomplete areas. The redshifts and cluster details reported in Table 2.2 reflect the results of this augmented method.

2.6 Properties of the SDSS Confirmed *Swift* Clusters

Here we describe various properties of the 104 SDSS confirmed clusters, match them to existing catalogs and discuss the implications for cluster science.

2.6.1 Overall Redshift Distribution

Figure 2.12 shows the distribution of our SDSS confirmed cluster redshifts, as compared to the Tinker et al. (2008) model for the mass function and redshift evolution of dark matter halos with masses ranging from $10^{14}h^{-1}M_{\odot}$ to $10^{15}h^{-1}M_{\odot}$, assuming $\Omega_m = 0.25$, $\sigma_8 = 0.9$, $h = 0.72$, and $\Delta = 2000$. Although the cosmological parameters are slightly different from the ones used in our paper, the model predictions are sufficient for our current qualitative comparison, providing

us with a model to test the completeness of our catalog. For lower redshifts, our survey appears complete up to $z \sim 0.3$ and is 80% complete up to $z \sim 0.4$. However, the observed distribution is significantly lower for higher redshifts. This is presumably due to the shallowness of the SDSS DR8 catalog for galaxies at these redshifts where galaxies are fainter. For the higher-z cluster candidates, we are performing our own, deeper optical observations.

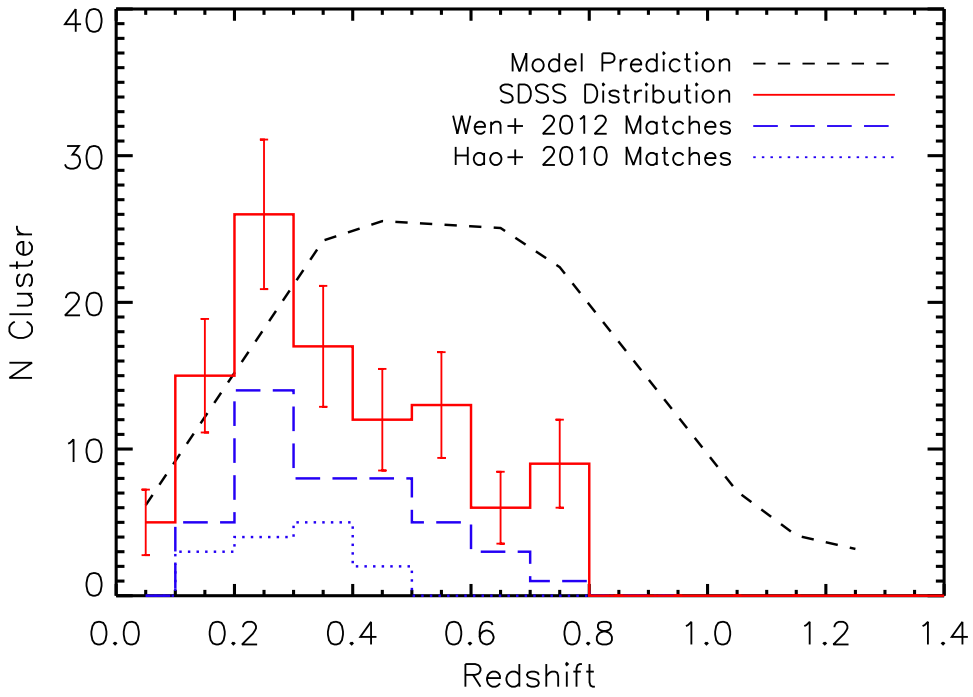


Figure 2.12: Observed redshift distribution (red, solid) as compared to a model prediction (dashed, Tinker et al. 2008). Standard error bars of $\sqrt{N}$ are used. The dashed and dotted histograms show redshift distributions of matches between our clusters and the Wen et al. (2012) and GMBCG (Hao et al., 2010) catalogs.

2.6.2 X-ray Bolometric Luminosities

An advantage of having an X-ray selected catalog with optical follow-up is that we can more easily identify correlations between properties in the two bands. Here, we discuss how we estimate the X-ray luminosity and compare it to the optical properties of the 104 candidate clusters with confirmed SDSS galaxy overdensities.

We used XSPEC (Arnaud, 1996) to convert the *Swift* X-ray count rates to luminosities, assuming a Galactic neutral hydrogen density of $5{\times}10^{20}$ cm^{-2}, a cluster temperature of 5 keV, and an abundance of 0.4 Solar. Assuming a β-model with $\beta = 0.65$, we corrected the X-ray luminosities to an aperture of radius 1.0 Mpc. In this way the aperture would be similar to that used for the optical richness calculations. The uncertainties in L_X, as seen in Figure 2.13, are a combination of the uncertainties of the X-ray photon counts and the 25% systematic uncertainties from changing the assumed β value by ± 0.15. We also estimate M_{500}, the mass inside of a radius R_{500} at which the density of the cluster is 500 times the critical density (ρ_c), using the relation

$$\ln L_X = (47.392 \pm 0.085) + (1.61 \pm 0.14) \ln M_{500} + (1.850 \pm 0.42) \ln E(z) - 0.39 \ln (h/0.72) \pm (0.396 \pm 0.039) \quad (2.1)$$

from Vikhlinin et al. (2009), where $E(z) \equiv H(z)/H_0$. These estimates are included in Table 2.2.

2.6.3 Optical Properties

We report observed galaxy counts (N_{Net}) and optical richness estimates (N_{opt}) in Table 2.2. The first is the excess galaxy count above the average background in the redshift bin of width $\Delta = 0.05$. N_{opt} is the estimated number of galaxies with magnitude brighter than M_*, assuming a Schechter luminosity function (e.g., Blackburne & Kochanek 2012; Dai 2009) with a break magnitude $M_* = -21.34$ mag and slope $\alpha = -1.07$ based on the results of Bell et al. (2003) for SDSS$-r$ band. We assume M_* evolves with redshift using the correction $\Delta M_* = Qz$ with $Q = 1.2$ as described by Dai (2009).

We converted the limiting apparent $r-$band magnitude $m_{lim} < 22.2$ into an absolute magnitude limit for each cluster candidate with a confirmed SDSS galaxy over-density. In calculating the limiting absolute magnitudes, we take into account Galactic dust extinction and also apply K-corrections. We use the NED[3] online calculator for Galactic extinction values based on the X-ray positions of the cluster candidates. We apply K-corrections using the template models of Assef et al. (2010) for the elliptical galaxies, the expected dominant galaxy population in clusters. We normalize the Schechter luminosity function for each cluster candidate using the limiting absolute magnitude and the observed background-subtracted galaxy count. We then use the redshift dependent M_* to estimate the optical richness, N_{opt}, of the confirmed galaxy clusters.

Since N_{Net} is found using apparent radii on the sky of $2'$ and $3'$, we correct N_{opt}

[3]NASA/IPAC Extragalactic Database: `ned.ipac.caltech.edu`

to an aperture radius of 1.0 Mpc, assuming an NFW density profile (Navarro et al., 1995). We do this by multiplying N_{opt} by $F(< R_{1.0})/F(< R_{obs})$, where $R_{1.0}$ is the projected radius of 1.0 Mpc, R_{obs} is the aperture radius in Mpc corresponding to either $2'$ or $3'$, and $F(< R)$ is the projected fraction inside radius R. We used the $L_X - M_{500}$ and $M_{200} - c_{200}$ relations to estimate the scale radius r_s (Vikhlinin et al., 2009; Shan et al., 2015; Navarro et al., 1995; Dai et al., 2010; Girardi et al., 1998). The uncertainties in N_{opt} are dominated by the statistical uncertainties in the galaxy counts ($\sqrt{N_{Net}}$) and are plotted in Figure 2.13. Since we calculate the excess galaxy count using a redshift bin width $\delta = 0.05$, smaller than the typical photometric redshift uncertainty of ~ 0.12 (as discussed in Section 2.4), we apply a correction factor of 6.01 for all clusters. At $z > 0.6$, where any SDSS galaxies must be significantly brighter than L_*, this procedure produces large corrections that tend to grossly overestimate N_{opt}. These clusters are indicated in Figure 2.13 with crosses ($\times$). In addition to N_{Net} and N_{opt}, we include r-band absolute magnitude of the BCGs. These are listed in Table 2.2.

2.6.4 Optical-to-X-ray Correlations

Figure 2.13 shows L_X as a function of N_{opt} for cluster candidates confirmed using the $3'$ region. Both L_X and N_{opt} correlate well with mass, as L_X probes the gas mass and N_{opt} traces the galaxy members (e.g., Lopes et al. 2006). The scaling relation $L_X/10^{44} = 10^{-3.53} N_{opt}^{2.67}$ we obtain in log space using an orthogonal regression fit with error dependent weights is shown in Figure 2.13 (solid line). Without the error dependent weights, we obtain the scaling relation of $L_X/10^{44} =$

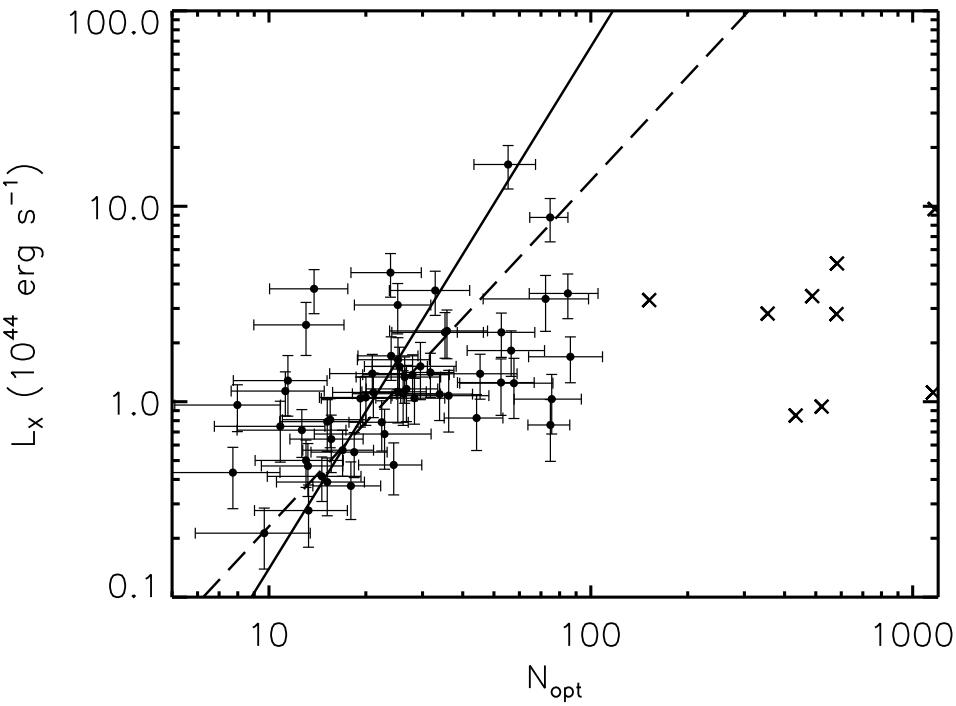


Figure 2.13: X-ray Bolometric Luminosity versus Optical Richness. The points are the confirmed *Swift* clusters and the black lines are the best fit orthogonal regression lines for the clusters with $z < 0.6$. The equations for the solid and dashed lines are $L_X/10^{44} = 10^{-3.53} N_{opt}^{2.67}$ and $L_X/10^{44} = 10^{-2.49} N_{opt}^{1.86}$, respectively. The former represents the best fit that includes error dependent weights and the latter represents the best fit without any weighting. The $\times$'s indicate clusters with $z > 0.6$, most likely with over-estimated richnesses due to the magnitude limits of SDSS and the faintness of distant galaxies. For this reason, these are excluded from the linear fit.

$10^{-2.49} N_{opt}^{1.86}$, also shown in Figure 2.13 (dashed line). The orthogonal regression line minimizes the perpendicular distances between the data points and the line (e.g., Isobe et al. 1990). Our slope of 2.67 is steeper than the results of Dai et al. (2007) and Kochanek et al. (2003), who report slopes of 1.56 and 1.33, respectively. Our slope of 1.86 agrees better with these two optically selected studies. Lopes et al. (2006) compares the slopes of the $L_X - N_{opt}$ from several studies in their Figure 17 and these slopes are in general steeper than what we measure here, ranging from 1.84 to 5.86. Comparisons are difficult, as each study can vary in fitting methods and in defining and estimating N_{opt} and L_X. For example, Lopes et al. (2006) discuss two methods of linear regression solutions, the ordinary least-squares (OLS) bisector and orthogonal regression (e.g., Isobe et al. 1990, where the OLS bisector is the line that bisects the OLS solution minimized in the Y direction (OLS(Y—X)) and the OLS solution minimized in the X direction (OLS(X—Y)). Lopes et al. (2006) found that the orthogonal regression line was better suited for this fit, especially in cases of large scatter. For ease of comparison and based on their results, we choose to use the orthogonal regression method. We find our slope is on the shallow end of those seen in Lopes et al. (2006). Here we mention a few potential reasons for this difference. We define optical richness in Section 2.6.3, and Lopes et al. (2006) use a definition based on a physical aperture and apparent magnitude of member galaxies. Furthermore, we use a bolometric X-ray luminosity and they use L_X in the [0.1−2.4 keV] energy band. Both Dai et al. (2007) and Donahue et al. (2001) use bolometric X-ray luminosities and report slopes of 1.56 and 3.60, respectively. Since clusters

are virialized objects, the predicted scaling relation between L_X and mass is $L_X \propto M^{4/3}$, $M \propto N_{opt}$, and $L_X \propto N_{opt}^{4/3}$ (e.g., Kaiser 1991). However, with the presence of non-gravitational effects, the scaling relations deviate from the above predictions. One of the recent measurement between L_X and total mass and stellar mass yields $L_X \propto M^{1.85}$ and $L_X \propto M_*^{2.53}$ (Anderson et al., 2015) and our measured slope $L_X \propto N_{opt}^{2.67}$ agrees with the L_X–M_* relation but deviates from the L_X–M relation of Anderson et al. (2015). And our measured slope of $L_X \propto M^{1.86}$, using a fit without error dependent weights, agrees with the L_X–M relation. Since all of these measurements have their own systematic uncertainties, we do not expect an exact match in the slopes at this stage. However, those studies that measured extreme steep slopes, 4–5, for the L_X–N_{opt} relation were subject to more severe systematic uncertainties.

We show L_X as a function of BCG r_{abs} in Figure 2.14. Here we test the correlation of luminosity and mass of the ICM with the luminosity of the BCG. Although there is a large scatter, we observe a general positive correlation when we fit the data with the orthogonal regression method (e.g., Isobe et al. 1990). The data is well correlated, with a Spearman's correlation coefficient of $r_s = -0.26$ and a probability of 0.03. Points shown in red indicate the BCGs with smallest BCG-to-X-ray center offsets. These clusters show less scatter than clusters with greater BCG-to-X-ray offsets, with correlation coefficients of -0.42 and -0.17 and probabilities of 0.04 and 0.27, respectively.

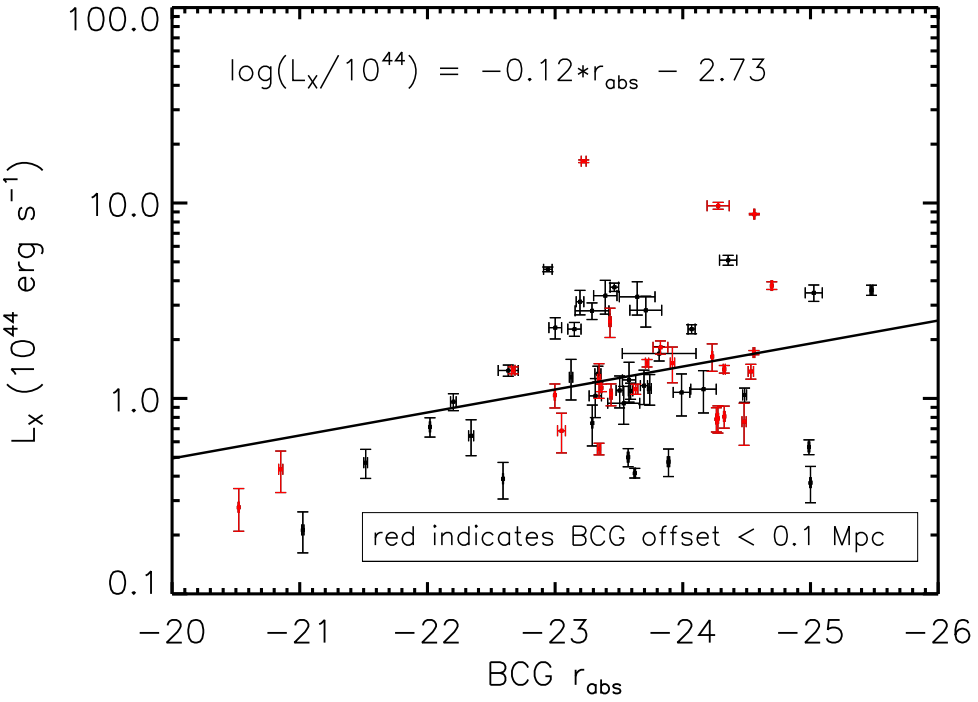


Figure 2.14: X-ray Bolometric Luminosity as a function of BCG Absolute Magnitude. Here we observe a roughly positive trend, with Spearman's correlation coefficient and probability of $r_s = -0.26$ and 0.03. This indicates a positive correlation (with large spread) between gas mass (from L_X) and BCG luminosity (from r_{abs}). The red points indicate BCG-to-X-ray-center offsets of < 0.1 Mpc and show a higher correlation than offsets of > 0.1 Mpc, with $r_s = -0.42$ and $r_s = -0.17$ and probabilities of 0.04 and 0.27, respectively.

2.6.5 The Red Sequence

We examined the color distributions for each candidate with a confirmed SDSS galaxy over-density to search for the red sequence feature seen in galaxy clusters. In general, cluster members and the surrounding background form a bimodal color distribution that is well represented by a two Gaussian fit, as seen in Figure 2.15 (e.g., Hao et al. 2010; Bell et al. 2004). The narrow, taller Gaussian is the red sequence feature, prominent in galaxy clusters. The distribution of background and/or foreground field galaxies can generally be approximated with a shallower, wider Gaussian, because the background galaxies are from different redshifts and the weak color bimodality is smoothed by redshifts. Following Hao et al. (2010), we shifted between the $g-r$, $r-i$, and $i-z$ colors to follow the shifting location of the Balmer break with redshift. The redshift ranges used for each color are listed in Table 2.5.

Redshift Range	Color
0.00 - 0.43	g − r
0.43 - 0.70	r − i
0.70 - 1.00	i − z

Table 2.5: From Table 2 of Hao et al. (2010). These are the colors used for the red sequence plots, dependent on redshift.

For each cluster candidate with a confirmed SDSS galaxy over-density, we examine the color distribution using galaxies within $3'$ of the cluster center and within redshifts $z_{cl} \pm 0.1$, where z_{cl} is our measured cluster redshift. We fit

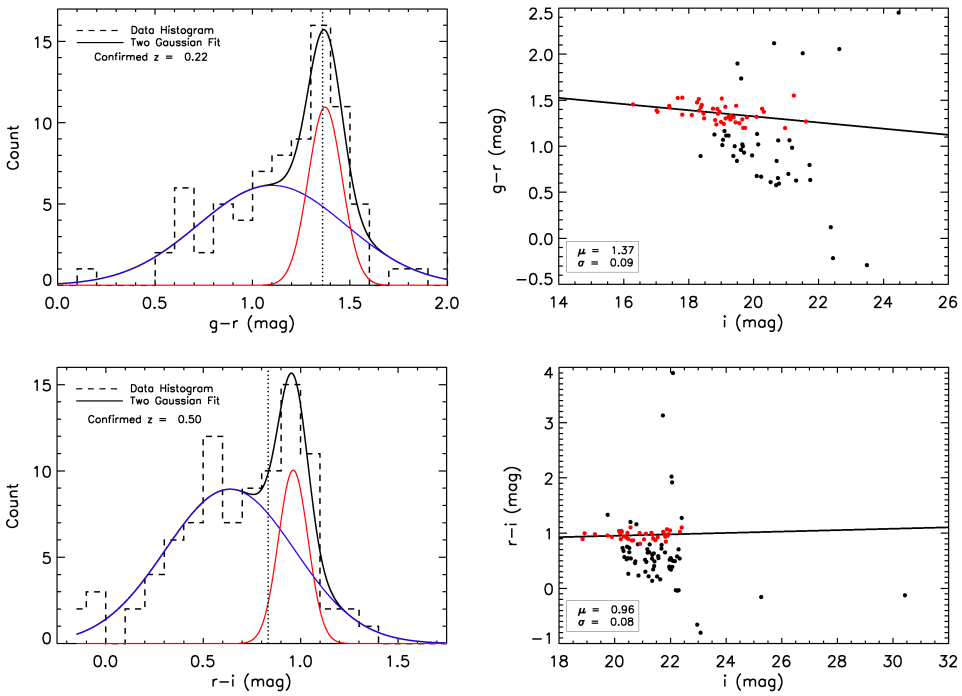


Figure 2.15: Color distributions and color magnitude diagrams. Left: Color distributions showing clear red sequences (red Gaussian fit) and field galaxies (blue Gaussian fit), in g − r for SWCL J232717.2 (top) at $z = 0.223$ and r − i for SWCL J222438.0 at $z = 0.499$ (bottom). Right: The corresponding CMDs with red points indicating galaxies within 2σ of the red sequence Gaussian. The line indicates the best fit to these points with mean μ and Gaussian dispersion σ.

the color distribution to a two Gaussian model where we allow the normalization, mean, and width of both Gaussians to vary and minimize the χ^2 statistic. For the lower redshift clusters, $z_{cl} \lesssim 0.11$, we use a single Gaussian model with one prior for the expected color. For these cases, we do not observe color contribution from the background galaxies, likely due to the extent of the clusters on the sky. Our two Gaussian model includes priors that constrain the width of the red sequence compared to that of the background and constrain the mean of the red sequence to favor the colors used by Hao et al. (2010) in their catalog of Gaussian Mixture Brightest Cluster Galaxy (GMBCG) clusters. We use the second prior because we know from Hao et al. (2010) how the red sequence evolves with redshift (see Figure 2.16). We calculate the second prior by averaging the color of GMBCG clusters in redshift bins of width $\Delta z = 0.05$. These are shown by green diamonds in Figure 2.16 and by the vertical lines in Figure 2.15. We find the red sequence feature in $\sim$85% of the confirmed clusters. The cluster galaxies (red dots in Figure 2.15, right), are the galaxies with color within 2σ of the red sequence mean. Two examples are shown in Figure 2.15, along with corresponding color magnitude diagrams (CMDs). Here we can observe the red sequence feature clearly both in the narrow histogram and in the clustering of galaxies in color-magnitude space. We also show the mean red sequence color as a function of redshift in Figure 2.16. Although there is a significant amount of scatter, Figure 2.16 shows a general positive trend for the g $-$ r and r $-$ i colors as redshift increases, as expected. We include GMBCG cluster colors from Hao et al. (2010) (dots) in Figure 2.16 as well as the color priors used for our two Gaussian fit (green

diamonds). In Figure 2.17, we plot the mass of clusters with confirmed redshifts, denoting clusters with a detected red sequence with red triangles and clusters without with black crosses ($\times$). We see that in general there is no difference in mass dependence. We performed a Kolmogorov-Smirnov (K-S) test to determine whether the two mass distributions are in fact different. We find there is a 0.56 probability that the distributions are drawn from the same distribution, signifying that the mass distribution of clusters with a detected red sequence is not significantly different than those without a detected red sequence. However, we do detect the red sequence in the six most massive clusters, so clusters with mass greater than $6.7 \times 10^{14} M_{\odot}$. Also, we find that the redshift distributions for detected red sequences versus undetected are significantly different, with a K-S test probability of 0.03.

The non-detections of the red sequence in our survey has several origins. The principle problem is that many of the galaxies are relatively faint, potentially leading to large color errors compared to the width of the red sequence. Galaxies fainter than the magnitude limit of SDSS will not be included in the color distributions, so that the distribution may not fit the two Gaussian model. This is especially true for more distant clusters where the observed flux is lower. At low redshifts, the X-ray data is also sensitive enough to include lower mass groups, which lack the well-defined red sequences of rich clusters. Nilo Castellón et al. (2014) had similar issues in their study of low X-ray luminosity galaxy clusters.

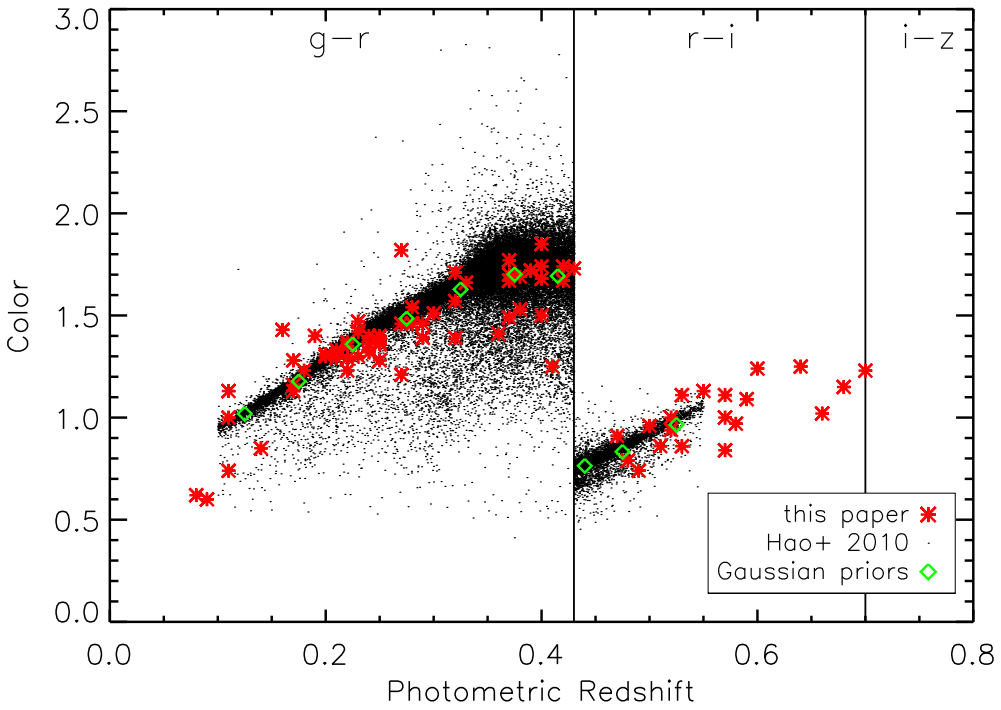


Figure 2.16: Mean red sequence color as a function of redshift for every galaxy cluster (red stars) that has an SDSS galaxy over-density and convergent Gaussian fit of the red sequence. The points are clusters from the GMBCG catalog (Hao et al., 2010). The green diamonds are the color priors from the GMBCG catalog used in the two Gaussian fits.

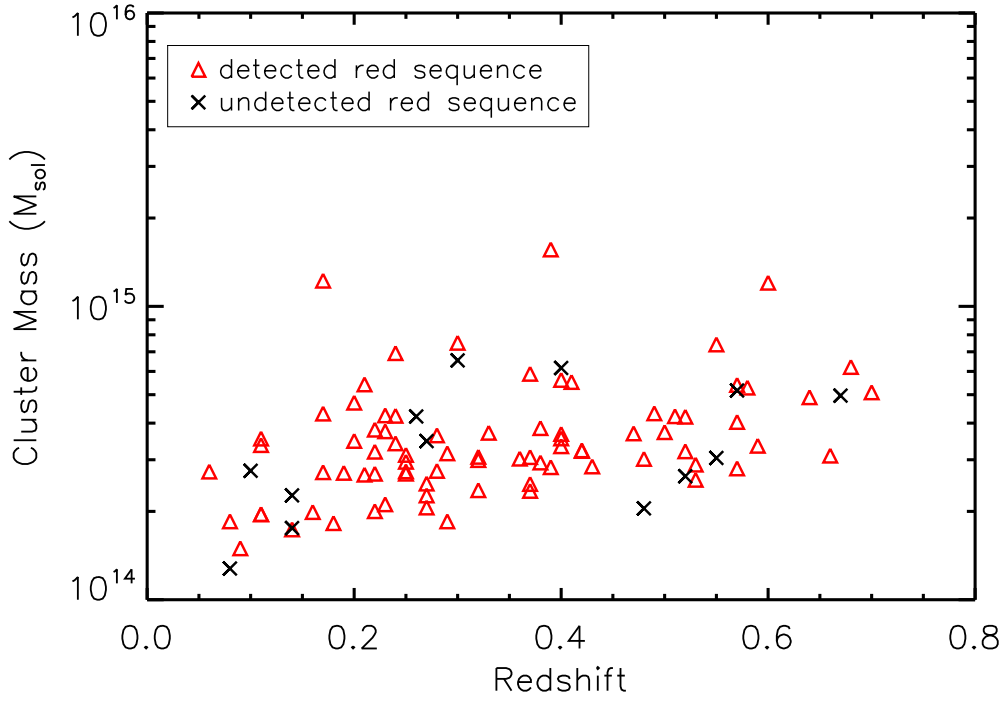


Figure 2.17: Cluster mass (in $M_{\odot}$) versus redshift. Here we look for a mass trend in clusters with detected red sequences in SDSS (red triangles) versus those without (black $\times$). We detect the red sequence in the 6 most massive clusters, although in general, we do not observe a mass trend.

2.6.6 Matching with Other Catalogs

We compare our catalog to other studies across multiple wavelengths to test for accuracy and completeness. We chose to compare to catalogs with large footprints since our *Swift* targets are scattered over a large fraction of the sky. First, we compare with optical catalogs, starting with the 132,684 galaxy clusters in the catalog from Wen et al. (2012). Their method uses a friend-of-friend algorithm incorporating SDSS III galaxies to identify clusters and their BCGs. We used a matching angular radius of up to $1'$. Out of 44 position matches, 41 agree in redshift within $|\delta z| < 0.1$ with an average redshift difference of 0.026. These are listed in Table 2.6. Of the 41 redshift matches, $\sim 70\%$ have mass greater than the median mass of our sample, showing that in general we are matching our more massive clusters to the optically selected catalog. Wen et al. (2012) claimed their catalog is 95% complete for $M_{500} > 10^{14} M_{\odot}$ and for the redshift range $0.05 \leq z < 0.42$, and our sample is complete for $M_{500} > 10^{14} M_{\odot}$ and $z < 0.3$. The number of clusters per survey area for the overlapping conditions $M_{500} > 10^{14} M_{\odot}$ and $0.05 < z < 0.3$ are equal (~ 0.37) and thus, the completeness statements for both samples are in agreement. We also compare our confirmed cluster redshifts to the GMBCG clusters (Hao et al., 2010). Using the above matching procedure, there are 18 position matches and 15 that agree in position as well as redshift, 14 of which are in the Wen et al. (2012) catalog. SWCL J121628.2 is not in the Wen et al. (2012) catalog, so the right ascension, declination and separation reported in Table 2.6 refer to the GMBCG catalog. The differences in redshift and position

between our catalog and these optical catalogs could arise from the fact that our clusters are X-ray selected and thus centered on the X-ray emission from the clusters as opposed to their optically selected clusters. However, some of the matches with large angular match radii ($> 0\farcm6$) might be spurious associations.

Swift Name	Separation (Arcmin)	Wen RA	Wen DEC	Wen Phot. z	GMBCG Phot. z	*Swift* Phot. z
SWCL J015752.9+165933	0.036	29.471	16.992	0.507	...	0.510
SWCL J015803.5+165005	0.036	29.515	16.835	0.209	...	0.223
SWCL J020003.8+084024	0.101	30.014	8.674	0.215	...	0.196
SWCL J025630.7+000601	0.049	44.129	0.101	0.355	0.375	0.374
SWCL J035259.4−004338	0.017	58.247	−0.727	0.325	0.314	0.301
SWCL J054716.7+641156	0.932	86.793	64.209	0.363	...	0.369
SWCL J083340.9+331118	0.513	128.421	33.197	0.709	...	0.682
SWCL J084749.4+133142	0.034	131.956	13.528	0.359	...	0.391
SWCL J090714.8+351020	0.566	136.802	35.167	0.210	...	0.218
SWCL J092730.1+301046	0.789	141.864	30.188	0.373	0.293	0.303
SWCL J095257.1+102440	0.061	148.237	10.410	0.375	...	0.400
SWCL J095513.4+181215	0.324	148.808	18.209	0.327	0.316	0.423
SWCL J095515.5+180357	0.983	148.818	18.050	0.622	...	0.745
SWCL J101341.5+430651	0.097	153.424	43.116	0.423	...	0.400
SWCL J111736.0+033711	0.817	169.387	3.625	0.442	...	0.403
SWCL J113427.6−070208	0.046	173.616	−7.036	0.251	...	0.239
SWCL J114232.3+505623	0.069	175.636	50.940	0.260	...	0.254
SWCL J114553.0+595320	0.010	176.471	59.889	0.182	...	0.546
SWCL J115811.3+452903	0.701	179.560	45.492	0.409	0.416	0.389
SWCL J121628.2+353820	0.058*	184.117*	35.640*	...	0.266	0.358
SWCL J121711.8+353745	0.458	184.306	35.635	0.443	0.459	0.492
SWCL J123313.9+210217	0.288	188.312	21.040	0.544	...	0.516
SWCL J130959.1+612530	0.166	197.492	61.423	0.243	0.254	0.248
SWCL J131521.9+164155	0.062	198.840	16.699	0.223	...	0.242
SWCL J140637.3+274348	0.054	211.655	27.731	0.655	...	0.600
SWCL J140639.0+273546	0.232	211.664	27.600	0.263	0.259	0.232

Swift Name	Separation (Arcmin)	Wen RA	Wen DEC	Wen Phot. z	GMBCG Phot. z	*Swift* Phot. z
SWCL J140726.4+274738	0.083	211.861	27.795	0.159	0.171	0.174
SWCL J143211.6+362225	0.845	218.041	36.361	0.572	...	0.663
SWCL J151550.9+442056	0.145	228.963	44.347	0.116	...	0.109
SWCL J152252.9+253527	0.037	230.720	25.591	0.549	...	0.546
SWCL J155159.8+445748	0.050	238.000	44.963	0.201	0.208	0.213
SWCL J155555.3+410548	0.046	238.980	41.097	0.355	0.375	0.368
SWCL J155708.6+354100	0.054	239.285	35.683	0.413	0.390	0.429
SWCL J155743.3+353020	0.245	239.427	35.508	0.148	0.169	0.166
SWCL J170757.1+235135	0.036	256.989	23.859	0.221	...	0.212
SWCL J215423.1+000526	0.381	328.598	0.084	0.175	0.156	0.169
SWCL J222432.9−021216	0.378	336.131	−2.203	0.242	...	0.162
SWCL J222438.0−022231	0.164	336.158	−2.372	0.507	...	0.499
SWCL J222444.0−022034	0.061	336.184	−2.343	0.658	...	0.714
SWCL J222954.1+194350	0.132	337.473	19.731	0.272	...	0.287
SWCL J224206.9+233408	0.391	340.522	23.571	0.432	...	0.402
SWCL J231257.7+182543	0.983	348.233	18.414	0.460	...	0.325
SWCL J231733.7+322828	0.216	349.394	32.476	0.405	...	0.400
SWCL J232248.4+054810	0.039	350.701	5.802	0.244	...	0.244
SWCL J232717.2+263108	0.225	351.825	26.522	0.230	...	0.223

Table 2.6: List of 45 position matches from comparing clusters of the GMBCG catalog (Hao et al., 2010) and catalog of Wen et al. (2012) to the SDSS identifications of the *Swift* AGN and Cluster Survey. We used a matching radius of $1'$. Of these 45, 42 agree in redshift to $\delta z < 0.1$. The remaining three are different enough in redshift to be different clusters and thus, not a match. Note: SWCL J121628.2+353820 is the only match in the GMBCG catalog that does not have a corresponding entry in the Wen et al. (2012) catalog, thus the separation, RA and Dec reported are actually from the GMBCG catalog.

Here we compare to catalogs with selections based on X-ray, SZ and lensing data. These trace the location of the gas in the cluster (e.g., Kravtsov & Borgani 2012) and should align with our sources better than optically selected surveys, so we use a smaller matching radius of 30″. We search for matches to X-ray selected clusters using the Meta-Catalog of X-Ray Detected Clusters of Galaxies (MCXC, Piffaretti et al. 2011). MCXC comprises of 1743 clusters and combines the ROSAT All Sky Survey with cluster surveys based on serendipitous observations. We find only two previously detected clusters, MCXC_J1557.7+3530 at redshift $z = 0.155$ and MCXC_J1557.7+3530 at $z = 0.360$. These match to our clusters SWCL J155743.3 at $z = 0.166$ and SWCL J025630.7 at $z = 0.374$ (Piffaretti et al., 2011). SWCL J025630.7 is also detected with the Atacama Cosmology Telescope (ACT) (Hasselfield et al., 2013) using the SZ effect. This is the only cluster match when compared to the 148 GHz observations by ACT of 68 galaxy clusters. We also compared our survey to the first release of SZ sources observed by Planck (Planck Collaboration et al., 2014b) and found that SWCL J084749.4 at $z = 0.391$ is a match to PSZ1_G213.43+31.78 at $z = 0.349$. Finally, we compared our confirmed galaxy clusters to the Deep Lensing Survey (Ascaso et al., 2014) but found no matches.

In Dai et al. (2015), we compared our catalog of extended sources to the *Swift* XRT Cluster Survey (SWXCS) (Tundo et al., 2012), and found 55 of 72 sources agreed in position to within 30″. Liu et al. (2015) expanded the analysis from using only GRB fields in Tundo et al. (2012) to also including non-GRB fields, increasing the number of fields to $\sim 3,000$ and finding 263 cluster candidates in a

total solid angle of ~ 400 deg^2. They cross-correlated their catalog with optical, X-ray, and SZ catalogs to match known galaxy and galaxy cluster redshifts that have similar positions. Of the 442 extended sources in Dai et al. (2015), 88 agree within $30''$ and 68 agree within $10''$. Although the number of SWXCS cluster candidates increases from 72 to 263 (Tundo et al., 2012; Liu et al., 2015), we do not see a comparative increase in matches because, like Tundo et al. (2012), our analysis includes only *Swift* GRB fields.

We compared the positions of our SDSS confirmed galaxy clusters to their updated catalog and found 37 position matches in the SDSS footprint using a matching radius of $10''$. These are shown in Table 2.7. In Liu et al. (2015), there are clusters with multiple reported redshifts that come from comparing the SWXCS to other studies. For these cases, we report the average of those redshifts in Table 2.7. Of those 37 matches, 23 have redshifts in both catalogs, 22 agree within $|\delta z| < 0.1$ and 19 agree within $|\delta z| < 0.05$ with an average redshift difference of $\Delta z \sim 0.033$. Furthermore, 17 of the 37 position matches were also matched to the Wen et al. (2012) catalog and thus are also presented in Table 2.6.

Swift Name	Separation (Arcmin)	SWXCS RA	SWXCS DEC	SWXCS Phot. z	*Swift* Phot. z
SWCL J002114.5+205943	0.051	5.3095	20.9956	...	0.141
SWCL J002823.6+092705	0.045	7.0987	9.4517	0.224	0.195
SWCL J012303.8+375609	0.150	20.7625	37.9361	...	...
SWCL J015752.9+165933	0.018	29.4699	16.9924	0.507	0.510
SWCL J020003.8+084024	0.026	30.0158	8.6730	0.215	0.196
SWCL J020745.0+002053	0.098	31.9375	0.3498	...	...
SWCL J035259.4−004338	0.033	58.2471	−0.7274	0.328	0.301

Swift Name	Separation (Arcmin)	SWXCS RA	SWXCS DEC	SWXCS Phot. z	*Swift* Phot. z
SWCL J075900.8+324449	0.065	119.7527	32.7480	...	0.579
SWCL J084749.4+133142	0.096	131.9544	13.5276	0.349	0.391
SWCL J092649.8+301346	0.043	141.7085	30.2296	0.559	0.567
SWCL J092719.6+301348	0.086	141.8327	30.2309	0.302	0.331
SWCL J092730.1+301046	0.058	141.8744	30.1798	0.312	0.303
SWCL J095206.7+102137	0.108	148.0280	10.3622	...	...
SWCL J095513.4+181215	0.052	148.8058	18.2051	0.416	0.423
SWCL J101341.5+430651	0.058	153.4235	43.1152	0.449	0.400
SWCL J114232.3+505623	0.037	175.6344	50.9393	0.260	0.254
SWCL J114503.1+600811	0.048	176.2613	60.1362	0.285	0.268
SWCL J124312.1+170454	0.126	190.8026	17.0812	0.142	0.136
SWCL J133051.0+420641	0.150	202.7158	42.1111	...	0.588
SWCL J133055.8+420015	0.076	202.7310	42.0048	...	0.113
SWCL J140637.3+274348	0.049	211.6547	27.7302	0.655	0.600
SWCL J140639.0+273546	0.109	211.6611	27.5974	0.252	0.232
SWCL J143211.6+362225	0.084	218.0467	36.3740	0.572	0.663
SWCL J143223.3+361752	0.028	218.0967	36.2980	...	...
SWCL J152252.9+253527	0.152	230.7187	25.5926	0.557	0.546
SWCL J155117.4+445118	0.083	237.8208	44.8551	...	0.697
SWCL J155743.3+353020	0.082	239.4292	35.5065	0.158	0.166
SWCL J164956.4+313021	0.082	252.4857	31.5070	...	0.734
SWCL J173932.8+272051	0.038	264.8860	27.3480	...	...
SWCL J194004.2+782415	0.051	295.0164	78.4033	...	...
SWCL J215507.7+164725	0.028	328.7821	16.7907	...	...
SWCL J222438.0−022231	0.092	336.1594	−2.3742	0.507	0.499
SWCL J222444.0−022034	0.006	336.1832	−2.3428	0.658	0.714
SWCL J222516.4−020825	0.068	336.3192	−2.1411	...	0.467
SWCL J222954.1+194350	0.159	337.4729	19.7292	0.272	0.287
SWCL J232248.4+054810	0.053	350.7014	5.8036	0.244	0.244
SWCL J232725.6+263506	0.037	351.8565	26.5843	0.059	0.257

Table 2.7: List of 37 position matches comparing clusters of the SWXCS catalog (Liu et al., 2015) to the SDSS identifications of the *Swift* AGN and Cluster Survey. Both cluster surveys use *Swift* fields to locate extended X-ray sources as potential galaxy clusters. We used a matching radius of $10''$. The redshifts of SWXCS are reported from various optical, X-ray and SZ catalogs (see Liu et al. (2015) for details). For SWXCS clusters with multiple redshifts listed, we report the average of these redshifts here. Of these 37 position matches, 23 have redshifts in both catalogs. 22 of 23 clusters agree in redshift to $\delta z < 0.1$. The remaining position match is different enough in redshift to be considered different clusters and thus, not a match. 19 clusters agree within redshift $\delta z < 0.05$.

2.7 Confirmed Clusters Not in Current Catalog

We went through various iterations of the X-ray source selection method before using the latest one discussed in Dai et al. (2015). There are 10 X-ray sources selected using a previous version of our algorithm that were confirmed as galaxy clusters using SDSS data and the method described above. These are listed in Table 2.8. Due to slight changes in the X-ray source selection algorithm, the significances of these sources changed to be below the significance threshold and so are not included in the current catalog or in Table 2.2. These clusters are worth mentioning for researchers interested in these individual clusters in future studies.

Swift Name	2′ Reg. Conf. z	3′ Reg. Conf. z	Conf. Phot. z	Conf. σ	N_{Net}	N_{opt}	BCG r_{mag}	BCG r_{abs}	Offset (Mpc)	L_X (erg/s)	M_{500} ($M_\odot$)
SWCL J015803.5+165006	0.223	0.232	0.223	7.42	11.92	3.43	16.95	−24.33	0.01	8.08e+43	2.69e+14
SWCL J095513.4+181216	0.423	0.421	0.423	4.51	11.59	5.58	19.54	−23.34	0.57	1.29e+44	3.15e+14
SWCL J095515.7+180359	0.745	0.747	0.745	8.35	11.14	160	20.37	−25.03	0.21	3.34e+44	4.57e+14
SWCL J083340.9+331117	0.682	0.676	0.682	8.42	18.06	112	20.66	−24.36	0.22	5.38e+44	6.43e+14
SWCL J124313.2+170443	0.132	0.134	0.132	6.28	10.16	3.31	15.80	−24.02	0.03	6.49e+43	2.48e+14
SWCL J224206.2+233350	0.403	...	0.403	5.69	15.04	7.18	19.40	−23.76	0.15	3.56e+44	6.01e+14
SWCL J115811.3+452904	0.389	0.407	0.389	5.90	17.08	6.58	18.39	−24.48	0.22	1.08e+44	2.91e+14
SWCL J160637.7+321349	0.065	0.064	0.065	5.22	7.25	4.23	16.22	−22.02	0.14	7.45e+43	2.80e+14
SWCL J082114.0+320018	0.746	0.732	0.746	7.39	9.08	142	21.16	−24.28	0.08	9.15e+44	8.55e+14
SWCL J232248.3+054810	0.319	0.245	0.245	5.63	9.50	22.8	16.85	−24.56	0.01	1.78e+44	4.33e+14
SWCL J222954.1+194349	0.286	0.291	0.286	8.18	16.66	5.03	18.00	−23.63	0.04	1.13e+44	3.19e+14
SWCL J143211.7+362226	0.663	0.623	0.663	4.66	10.36	39.0	21.34	−23.47	0.10	1.79e+44	3.29e+14

Table 2.8: Clusters we found in a previous version of our X-ray selection method, but excluded from the current catalog due to changes in the significance threshold. Columns are the same as in Table 2.2.

2.8 Summary & Discussion

In this paper, we present SDSS identifications (Table 2.2), including estimated redshifts, X-ray and optical properties, for the X-ray selected galaxy clusters we identified in Dai et al. (2015). We confirmed 104 of the 203 cluster candidates in the SDSS footprint and estimate that the catalog is 80% complete up to $z = 0.4$. Most of the remaining cluster candidates are expected to be at higher redshifts where the member galaxies are too faint to use SDSS for confirmations. This sample significantly increases the number of X-ray selected clusters with confirmed redshifts and it is one of the largest uniformly-selected cluster samples, covering a total sky area of 125 deg^2.

We observe clear red sequences and clustering of galaxies in color-magnitude space in ∼85% of the clusters. X-ray source centers and BCG locations show good agreement, with small offsets and distributions similar to other studies. We find clear matches with previously observed clusters. Our X-ray luminosities correlate well with optical properties and our $L_X - N_{opt}$ slope agrees with other estimates. Thus, it is clear the *Swift* technique presented in Dai et al. (2015) is successfully identifying extended X-ray sources that are in fact galaxy clusters. In future studies, we will look at changing the significance threshold of the X-ray source detection (Dai et al., 2015) as it may be too stringent currently. For example, we list 10 clusters in Table 2.8 that were confirmed by the SDSS data but removed from the current X-ray catalog based on the final choice for the significance threshold.

Our method combines X-ray and optical techniques and properties to confirm galaxy cluster candidates and can be used for similar studies. In this way we find 63 new galaxy clusters in the SDSS footprint that were not detected using the optical cluster finding methods of Wen et al. (2012) and Hao et al. (2010). The next step is to look deeper in magnitude and beyond the footprint of SDSS. Although SDSS was a good start, the data is too shallow for higher redshift clusters and has incomplete sky coverage. There are $\sim$ 100 undetected *Swift* extended sources in the SDSS footprint, and still $\sim$ 250 outside, for a total of $\sim$ 350.

We have been performing our own follow-up observations with observing programs taking photometric data at the MDM 2.4m, Kitt Peak 4m, and CTIO (Cerro Tololo Inter-American Observatory) 4m. We have also observed candidates with redshifts of $z \sim 0.5$ at the Magellan 6.5m and MDM 2.4m using multi-slit spectroscopic masks. Once we derive galaxy redshifts from our data we will use the method outlined in this paper to confirm additional clusters at higher redshifts. Furthermore, our sample will be more statistically significant when it is more complete, which will lead to better constraints on the cluster mass function.

2.9 Acknowledgements

This chapter is reproduced by permission of the American Astronomical Society from the following publication: Griffin, R. D., X. Dai, C. Kochanek, & J. Bregman

(Jan 2016). “The *Swift* AGN and Cluster Survey. II. Cluster Confirmation with SDSS Data”. In: ApJS 222, 13.

We acknowledge the financial support from the NASA ADAP program NNX11AD09G and NSF grant AST-1413056. Funding for the creation and distribution of the SDSS Archive has been provided by the Alfred P. Sloan Foundation, the Participating Institutions, the National Aeronautics and Space Administration, the National Science Foundation, the US Department of Energy, the Japanese Monbukagakusho, and the Max Planck Society. We thank the anonymous referee for the detailed report and helpful comments.

Chapter 3

New Limits On Gamma-Ray Emission From Galaxy Clusters

We developed a method of stacking *Fermi* gamma-ray count maps to constrain the signal expected from galaxy clusters. Here we discuss the method, our results and the impact on cosmology. In Appendix A, we discuss our revised method to study the gamma-ray emission from luminous and ultraluminous infrared galaxies.

3.1 Introduction

Galaxy clusters are the largest gravitationally bound structures in the universe and as such are important tools for studies of structure formation and cosmology. Past and current methods of detection include optical and X-ray observations, the Sunyaev-Zel'dovich effect, and gravitational lensing (e.g., Kravtsov & Borgani 2012 and references within). Each new way of observing galaxy clusters can reveal more about these objects, the physics involved, and the history of their formation.

The prevailing structure formation theory suggests that galaxy clusters formed through the hierarchical merging of smaller systems, driven by the gravity of the dominant dark matter. During the merging process, merger shocks form in the baryons, accelerating cosmic ray (CR) particles to ultra-relativistic speeds with Lorentz factors $\Gamma \gg 1000$ (e.g., Völk et al. 1996; Berezinsky et al. 1997). Evidence

for this can be seen in the form of cluster radio halos or relics, spatially extended radio emission or giant radio arcs on scales of $\sim$1 Mpc due to synchrotron emission by CR electrons (Feretti et al., 2012). Electrons lose energy quickly ($\leq 10^8$ yr) due to the high efficiency of synchrotron emission, non-thermal bremsstrahlung, and up-scattering of CMB radiation and so radio relics only probe recent events.

The shock models also predict that a much larger amount of energy is deposited in the hadronic component (ultra-relativistic protons). CR protons have a very long cooling time ($\geq 10^{10}$ yr) and interact with protons in the hot intergalactic medium (1–10 keV) of the clusters (e.g., Berezinsky et al. 1997; Berrington & Dermer 2003; Kravtsov & Borgani 2012). Hadronic debris from these p$-$p interactions includes neutral pions, whose main decay channel is two γ-rays: $\pi^0 \rightarrow 2\gamma$ (99%) (Amsler et al., 2008). This π^0 decay is expected to dominate the CR induced γ-ray emission which is predicted to be detectable by the *Fermi* Large Area Telescope and other γ-ray missions (*Fermi*-LAT, e.g., Ackermann et al. 2014; Vazza & Brüggen 2014, Reimer et al. 2003, Aleksić et al. 2012, Arlen et al. 2012).

Other processes that contribute to the γ-ray emission are inverse Compton scattering and relativistic bremsstrahlung emissions, but these are likely subdominant (e.g., Jeltema et al. 2009; Pinzke & Pfrommer 2010; Vazza & Brüggen 2014; Brunetti & Jones 2014). In addition, to detect any dark matter annihilation signal in clusters and set stringent constraints on dark matter annihilation cross-sections, the CR emission is a background that must be characterized as part of the spectrum (Ackermann et al. 2014; Huber et al. 2013).

Several recent papers focus on *Fermi*-LAT searches for this γ-ray emission; however, no diffuse γ-ray emission from galaxy clusters has firmly been detected (Ackermann et al. 2014, Huber et al. 2013, Prokhorov and Churazov 2014 by stacking $\sim$ 50 clusters; Ackermann et al. 2014, Han et al. 2012, Zandanel and Ando 2014 for individual clusters). *Fermi*-LAT has detected point-like γ-ray emission from the radio galaxies at the centers of the Virgo and Perseus clusters, although these are not attributed to neutral pion decay in the intergalactic medium (Abdo et al. 2009a, 2009b). In these studies, extragalactic sources beyond the 2FGL catalog[1] (Nolan et al., 2012) could cause contamination (Han et al. 2012, Ackermann et al. 2014, Prokhorov and Churazov 2014). The results of the stacking analyses of Ackermann et al. (2014), Huber et al. (2013), and Prokhorov and Churazov (2014) establish the lowest flux upper limits to date and Huber et al. (2013) reached the lowest limits at 2.8–4.9$\times10^{-11}$ photon cm^{-2} s^{-1} in the 1–300 GeV band. Flux upper limits from these stacking analyses are in partial conflict with current models of CR acceleration (e.g., Huber et al. 2013). Vazza & Brüggen (2014) argued that the expected γ-ray emission for most clusters with radio relics should be close to or above the flux limits set by these stacking analyses.

In this Letter, we present an independent study on this topic, using a uniformly selected sample of nearby clusters. Our sample is unique among *Fermi* cluster stacking analyses as all of the studies mentioned above use only high X-ray flux HIFLUGCS clusters (Reiprich & Böhringer 2002). Our final selection of 78

[1] `http://heasarc.gsfc.nasa.gov/W3Browse/all/fermilpsc.html`

clusters includes just 5 HIFLUGCS clusters and of the original 163, 33 are in the HIFLUGCS catalog. In §2 we discuss the cluster sample, the γ-ray data reduction process and the stacking analysis, and we discuss the results and consequences in §3. We assume $H_0 = 70$ km s^{-1}Mpc^{-1}, $k = 0$, $\Omega_M = 0.3$, and $\Omega_\Lambda = 0.7$.

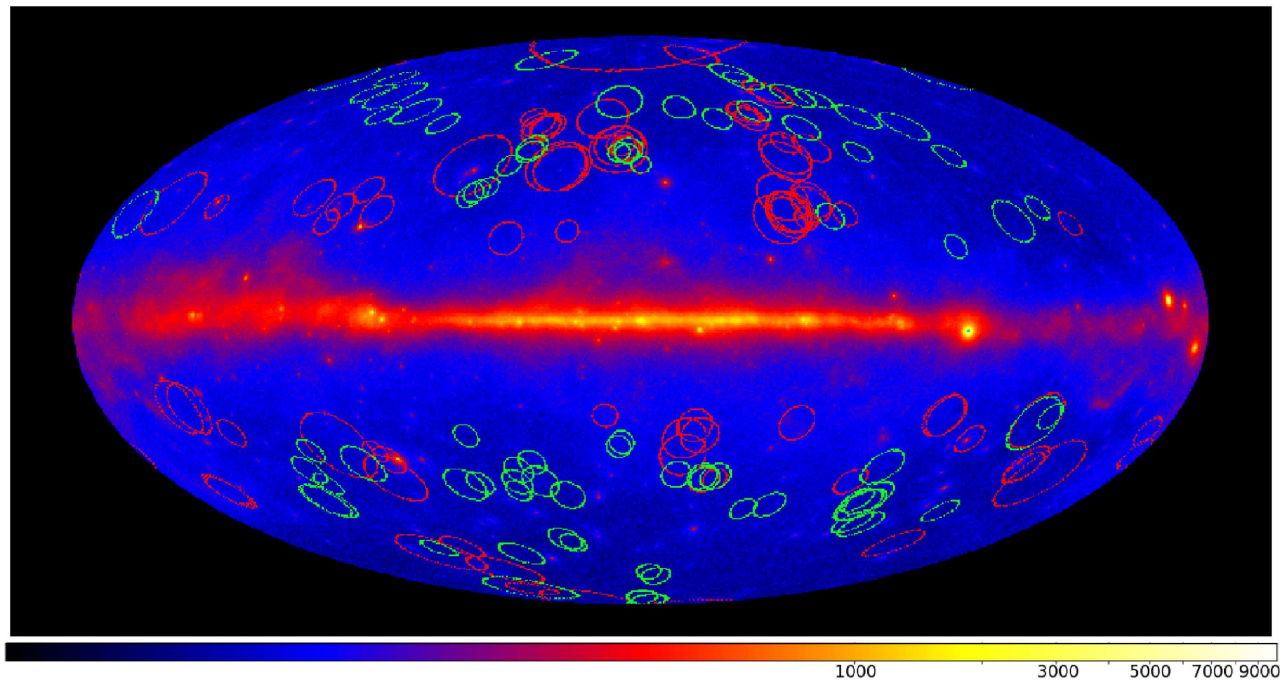


Figure 3.1: All-sky photon count map for the analyzed data. The green ellipses show the locations and area of the 78 rich 2MASS clusters included in the final analysis and red ellipses show the rejected clusters.

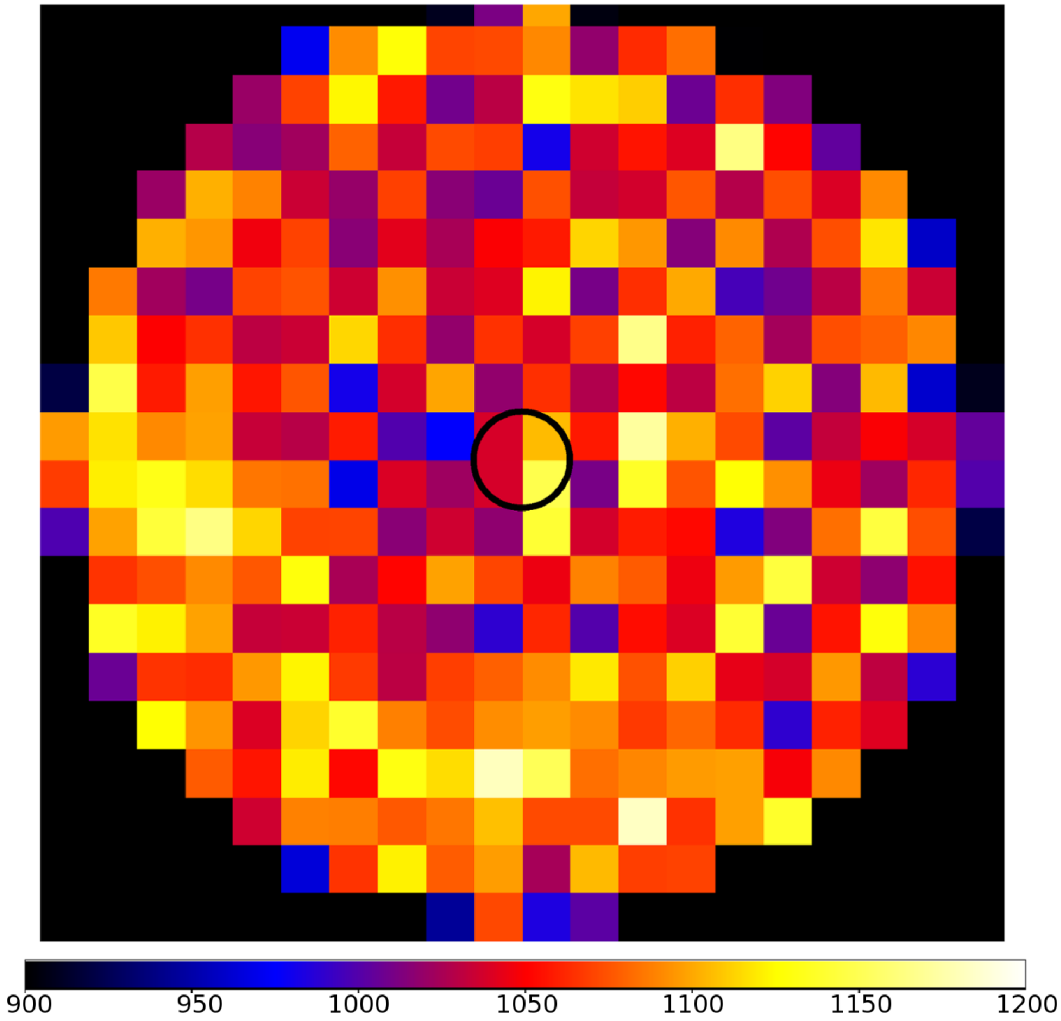


Figure 3.2: Final 0.8–100 GeV stacked image for the 78 clusters. The analysis region is 20 Mpc in radius and we limit the flux in the central 2 Mpc source region (black circle).

3.2 Analysis

Our cluster sample consists of the richest, nearby ($z < 0.12$) clusters in the 2MASS catalog of clusters identified using a matched filter algorithm (Kochanek et al. 2003). Like *Fermi*, 2MASS is also an all-sky survey, and we start with the 163 richest clusters outside of the Galactic plane ($|b| > 20°$) with $z < 0.12$ ($\bar{z} = 0.08$) and typical masses of $M_{200} \sim 6 \times 10^{14} M_{\odot}$. The sample is well-characterized in richness and distance with extensive calibrations using both near-IR and X-ray stacking analyses (Dai et al., 2007, 2010; Blackburne & Kochanek, 2012). We eventually use 78 of the original 163 clusters as discussed in §3. Details of these clusters are listed in Table 3.1.

Name	RA	Decl	z	Richness	In Final Stack?
2MASSCL_J0330-5235	52.590	-52.585	0.060	28.758	yes
2MASSCL_J0317-4417	49.438	-44.297	0.074	13.183	yes
2MASSCL_J0108-1526	17.228	-15.435	0.053	10.392	yes
2MASSCL_J0327-5323	51.841	-53.392	0.061	16.375	yes
2MASSCL_J0343-5338	55.753	-53.643	0.059	20.109	yes
2MASSCL_J0312-4725	48.191	-47.417	0.081	10.006	yes
2MASSCL_J2235+0129	338.935	1.496	0.059	14.214	yes
2MASSCL_J0112+1611	18.103	16.196	0.061	11.029	yes
2MASSCL_J0544-2558	86.200	-25.968	0.042	15.188	yes
2MASSCL_J1311+3915	197.832	39.262	0.072	15.287	yes
2MASSCL_J1157+0504	179.370	5.081	0.076	11.157	yes
2MASSCL_J1335+5910	203.986	59.175	0.070	10.987	yes
2MASSCL_J0431-6124	67.809	-61.415	0.059	26.199	yes
2MASSCL_J2201-2225	330.476	-22.428	0.069	10.336	yes
2MASSCL_J1426+1641	216.664	16.699	0.053	11.816	yes
2MASSCL_J0116+1618	19.063	16.304	0.066	11.666	yes
2MASSCL_J2308-1953	347.126	-19.884	0.081	12.324	yes
2MASSCL_J2336+2106	354.081	21.101	0.058	12.712	yes
2MASSCL_J2152-1538	328.002	-15.639	0.063	11.427	yes
2MASSCL_J0358-3015	59.576	-30.259	0.097	13.264	yes

Name	RA	Decl	z	Richness	In Final Stack?
2MASSCL_J1032+4010	158.067	40.175	0.072	13.507	yes
2MASSCL_J2354-1024	358.549	-10.407	0.076	19.762	yes
2MASSCL_J2158-6025	329.574	-60.426	0.075	23.248	yes
2MASSCL_J0017-3511	4.404	-35.190	0.097	17.916	yes
2MASSCL_J1039+0510	159.862	5.174	0.068	11.689	yes
2MASSCL_J0328-5541	52.175	-55.695	0.086	13.444	yes
2MASSCL_J0051-2830	12.838	-28.504	0.112	17.951	yes
2MASSCL_J0042-2834	10.695	-28.578	0.108	19.567	yes
2MASSCL_J1215-0650	183.792	-6.844	0.077	10.614	yes
2MASSCL_J2145-1005	326.497	-10.089	0.079	11.595	yes
2MASSCL_J1353+0508	208.277	5.150	0.079	15.175	yes
2MASSCL_J2312-2131	348.050	-21.526	0.109	24.831	yes
2MASSCL_J2358-6036	359.712	-60.609	0.099	18.808	yes
2MASSCL_J0908-0938	137.224	-9.643	0.054	27.751	yes
2MASSCL_J1709+3425	257.423	34.423	0.084	17.255	yes
2MASSCL_J2130-1312	322.564	-13.207	0.084	10.189	yes
2MASSCL_J2214-1021	333.632	-10.355	0.096	15.374	yes
2MASSCL_J0045-6333	11.481	-63.562	0.079	11.636	yes
2MASSCL_J2153-5745	328.475	-57.760	0.076	31.222	yes
2MASSCL_J1121+4803	170.382	48.054	0.116	25.634	yes
2MASSCL_J1552+2731	238.120	27.524	0.079	17.984	yes
2MASSCL_J1008+0004	152.250	0.071	0.095	14.101	yes
2MASSCL_J1236-3353	189.146	-33.894	0.081	15.386	yes
2MASSCL_J1227+0851	186.879	8.853	0.089	19.426	yes
2MASSCL_J1702+3330	255.707	33.505	0.088	16.891	yes
2MASSCL_J2129-5048	322.400	-50.806	0.077	11.344	yes
2MASSCL_J0006-3442	1.603	-34.703	0.113	16.636	yes
2MASSCL_J0046+0000	11.595	0.002	0.115	10.305	yes
2MASSCL_J0049+2427	12.458	24.466	0.082	18.477	yes
2MASSCL_J1200+5614	180.040	56.247	0.065	11.905	yes
2MASSCL_J1141+0536	175.292	5.603	0.097	10.596	yes
2MASSCL_J2202-0956	330.579	-9.947	0.079	14.990	yes
2MASSCL_J2224-0135	336.009	-1.591	0.091	12.921	yes
2MASSCL_J1620+2949	245.208	29.832	0.095	14.003	yes
2MASSCL_J1654+3128	253.730	31.479	0.098	10.870	yes
2MASSCL_J1119+5341	169.925	53.687	0.103	25.892	yes
2MASSCL_J1132-1152	173.229	-11.880	0.104	13.710	yes
2MASSCL_J1510+0449	227.703	4.830	0.078	16.013	yes
2MASSCL_J1330-0151	202.723	-1.866	0.087	12.033	yes
2MASSCL_J1248+6237	192.167	62.624	0.104	12.704	yes
2MASSCL_J1113+0231	168.461	2.526	0.076	10.203	yes
2MASSCL_J1558+2714	239.592	27.240	0.089	40.181	yes
2MASSCL_J1249-0142	192.301	-1.703	0.085	16.449	yes

Name	RA	Decl	z	Richness	In Final Stack?
2MASSCL_J0020+2838	5.167	28.643	0.096	17.278	yes
2MASSCL_J0854+0040	133.639	0.667	0.107	12.482	yes
2MASSCL_J2146-5715	326.685	-57.260	0.075	29.000	yes
2MASSCL_J1518+0613	229.691	6.232	0.103	23.762	yes
2MASSCL_J0955-2933	148.793	-29.552	0.095	11.477	yes
2MASSCL_J1229+1146	187.456	11.776	0.087	11.929	yes
2MASSCL_J2131+0356	322.864	3.947	0.093	17.564	yes
2MASSCL_J0714+4525	108.635	45.431	0.055	10.817	yes
2MASSCL_J2034-3557	308.715	-35.961	0.088	11.221	yes
2MASSCL_J2041-3513	310.482	-35.226	0.090	16.545	yes
2MASSCL_J0046+2028	11.622	20.481	0.104	12.830	yes
2MASSCL_J1453+5416	223.490	54.271	0.099	14.337	yes
2MASSCL_J1515+0422	228.823	4.369	0.098	16.932	yes
2MASSCL_J0548-2157	87.088	-21.958	0.093	10.598	yes
2MASSCL_J1516-0048	229.061	-0.814	0.117	18.458	yes
2MASSCL_J1453+1643	223.252	16.725	0.045	10.248	no
2MASSCL_J0433-1318	68.379	-13.305	0.033	12.794	no
2MASSCL_J0721+5544	110.347	55.744	0.039	19.432	no
2MASSCL_J2338+2705	354.716	27.086	0.031	13.706	no
2MASSCL_J1347-3257	206.874	-32.956	0.039	14.885	no
2MASSCL_J0547-2533	86.968	-25.551	0.041	22.982	no
2MASSCL_J0056-0113	14.061	-1.228	0.045	17.459	no
2MASSCL_J1327-2715	201.858	-27.264	0.041	20.446	no
2MASSCL_J1952-5506	298.039	-55.100	0.060	16.974	no
2MASSCL_J0108-1534	17.246	-15.579	0.099	16.807	no
2MASSCL_J2155-5721	328.913	-57.362	0.076	10.311	no
2MASSCL_J1241+1833	190.294	18.556	0.072	13.352	no
2MASSCL_J2019-5247	304.962	-52.785	0.048	17.235	no
2MASSCL_J0312-2659	48.032	-26.991	0.067	10.747	no
2MASSCL_J0627-5426	96.878	-54.444	0.050	24.705	no
2MASSCL_J2202-6011	330.579	-60.195	0.097	17.172	no
2MASSCL_J1511+0554	227.760	5.902	0.079	28.127	no
2MASSCL_J2051-5247	312.897	-52.792	0.045	21.389	no
2MASSCL_J1257-1724	194.367	-17.412	0.047	17.543	no
2MASSCL_J0626-5343	96.528	-53.723	0.053	17.512	no
2MASSCL_J2012-5649	303.108	-56.832	0.055	29.253	no
2MASSCL_J1215-3300	183.960	-33.009	0.090	16.507	no
2MASSCL_J1713+6403	258.295	64.057	0.080	10.898	no
2MASSCL_J1712+6403	258.246	64.052	0.080	35.346	no
2MASSCL_J0041-0919	10.410	-9.321	0.055	15.533	no
2MASSCL_J1713+6403	258.297	64.060	0.080	14.796	no
2MASSCL_J0023-0146	5.910	-1.783	0.085	11.675	no
2MASSCL_J1333-3137	203.430	-31.618	0.049	10.502	no

Name	RA	Decl	z	Richness	In Final Stack?
2MASSCL_J1511+0517	227.786	5.293	0.079	13.211	no
2MASSCL_J0102-2154	15.631	-21.901	0.055	10.785	no
2MASSCL_J1605+1748	241.364	17.814	0.037	16.136	no
2MASSCL_J1628+3935	247.133	39.590	0.030	16.378	no
2MASSCL_J2324+1439	351.111	14.658	0.042	12.131	no
2MASSCL_J1218+0515	184.743	5.254	0.077	10.532	no
2MASSCL_J1258-0146	194.692	-1.781	0.084	16.129	no
2MASSCL_J1244-1159	191.101	-11.993	0.094	10.601	no
2MASSCL_J1259+2755	194.900	27.930	0.023	21.477	no
2MASSCL_J0155+3354	28.785	33.904	0.088	12.073	no
2MASSCL_J1257-3021	194.277	-30.365	0.055	26.164	no
2MASSCL_J1741+1723	265.479	17.392	0.061	10.862	no
2MASSCL_J0246+3653	41.549	36.892	0.048	10.347	no
2MASSCL_J1605+1617	241.422	16.293	0.041	12.860	no
2MASSCL_J0333-6414	53.289	-64.240	0.079	11.084	no
2MASSCL_J1603+1614	240.765	16.244	0.038	28.733	no
2MASSCL_J1522+2741	230.619	27.696	0.072	23.001	no
2MASSCL_J1516+0703	229.188	7.055	0.038	12.301	no
2MASSCL_J1323-3142	200.997	-31.708	0.048	13.226	no
2MASSCL_J1328-3132	202.087	-31.534	0.048	50.157	no
2MASSCL_J1331-3144	202.814	-31.739	0.048	25.392	no
2MASSCL_J1332-0338	203.127	-33.135	0.049	11.461	no
2MASSCL_J1703+0305	255.959	3.086	0.095	11.527	no
2MASSCL_J1311-3417	197.887	-34.297	0.095	12.003	no
2MASSCL_J2305+2102	346.336	21.036	0.101	16.301	no
2MASSCL_J1703+7839	255.873	78.655	0.058	32.456	no
2MASSCL_J1512+0727	228.155	7.454	0.045	10.443	no
2MASSCL_J1254-2901	193.630	-29.030	0.054	17.226	no
2MASSCL_J1217+0337	184.390	3.624	0.077	20.523	no
2MASSCL_J0825+0429	126.463	4.499	0.101	15.061	no
2MASSCL_J0259+1337	44.751	13.621	0.074	15.832	no
2MASSCL_J1254-0238	193.720	-2.635	0.116	15.396	no
2MASSCL_J0257+1257	44.300	12.956	0.072	14.641	no
2MASSCL_J0258+1320	44.586	13.347	0.074	37.626	no
2MASSCL_J2002-3005	300.638	-30.089	0.088	14.009	no
2MASSCL_J1517-0043	229.341	-0.722	0.117	35.425	no
2MASSCL_J1252-1526	193.238	-15.437	0.046	12.585	no
2MASSCL_J1849+7020	282.339	70.348	0.090	10.051	no
2MASSCL_J0301+3548	45.436	35.815	0.046	13.786	no
2MASSCL_J1302-0227	195.711	-2.461	0.083	12.108	no
2MASSCL_J1759+6912	269.784	69.206	0.082	15.738	no
2MASSCL_J2006-8316	301.516	-83.282	0.059	11.552	no
2MASSCL_J0413+1028	63.372	10.482	0.087	21.473	no

Name	RA	Decl	z	Richness	In Final Stack?
2MASSCL_J1510+3329	227.553	33.492	0.113	24.913	no
2MASSCL_J1522+2821	230.609	28.365	0.083	10.773	no
2MASSCL_J0436+1039	69.125	10.666	0.095	24.492	no
2MASSCL_J0448-2029	72.036	-20.491	0.072	19.624	no
2MASSCL_J1801+5738	270.319	57.640	0.068	14.003	no
2MASSCL_J1509+0732	227.391	7.549	0.078	15.506	no
2MASSCL_J1521+3035	230.297	30.592	0.078	15.753	no
2MASSCL_J1527+2855	231.948	28.929	0.066	14.577	no
2MASSCL_J1219-1321	184.900	-13.359	0.069	12.298	no
2MASSCL_J1259-0411	194.877	-4.197	0.082	11.736	no
2MASSCL_J0452-2039	73.210	-20.666	0.063	10.139	no
2MASSCL_J0540-4325	85.033	-43.420	0.086	13.618	no
2MASSCL_J0708+7151	107.003	71.861	0.105	14.233	no
2MASSCL_J2303+1742	345.809	17.702	0.078	12.230	no

Table 3.1: Position, redshift and richness for the 163 galaxy clusters used in our study. The first 78 are the clusters used in the final stacked image and are ordered by the variance of the background, starting with the lowest variance cluster. The richness is the number of galaxies with luminosity $L > L_*$ (Kochanek et al., 2003). Note that 5 of the 78 clusters in our final stack (33 of 163) are HIFLUGCS clusters (Reiprich & Böhringer 2002).

We downloaded the Pass 7 LAT data from the Fermi Science Support Center (FSSC)[2], along with the Fermi Science Tools (version `v9r31p1`). We used the pre-generated weekly all-sky files which span 2008–08–04 to 2013–06–20 for a total of 255 weeks ($\sim$ 5 years) for SOURCE class photon events. We followed the FSSC Data Preparation recommendations for our analysis. Since the point spread function (PSF) of *Fermi*-LAT decreases with energy, we used a minimum energy threshold of $\sim$ 1 GeV so that the PSF is always more compact than 0.6 deg, which also lowers the contributions of point sources. A zenith angle cut of 100° was applied to avoid CR-produced γ-rays originating

[2] `http://fermi.gsfc.nasa.gov/ssc`

from the Earth's atmospheric limb. Good time intervals were identified using the recommended selection expression ((DATA_QUAL==1) && (LAT_CONGIF==1) && ABS(ROCK_ANGLE)<52) to exclude periods of dead time during spacecraft maneuvers, software updates, and transits through the Southern Atlantic Anomaly.

We first extracted count and exposure maps for each week and then stacked them in time to make a single count and exposure map for each cluster. We then stacked the clusters to obtain the final stacked image. As we generate the map for each cluster, we search for high background flares from variable γ-ray sources in the weekly images, 2σ above the mean photon flux (photon cm^{-2} s^{-1}), and reject these time periods. We used seven logarithmically spaced energy bins to cover the $0.8 - 100$ GeV band and the exposure maps were calculated at the mean energy of each bin.

Since clusters at higher redshifts have smaller angular sizes, we combine the clusters over a fixed 20 Mpc radius region of interest (ROI) binned into 2 Mpc pixels. This is more physical than stacking on a fixed angular scale as done previously (Ackermann et al. 2014; Huber et al. 2013; Prokhorov & Churazov 2014). The cluster emission should lie only in the central 2 Mpc and the remainder provides the background region. We also weight the clusters by z^2 so that the stacked signal is not dominated by nearby clusters. This also helps to reduce the variance in the final, stacked image. Since the 2 Mpc extraction region can be smaller than the *Fermi* PSFs at lowest energies $\sim$ 1 GeV, we calculated energy-dependent aperture flux corrections, and applied them to the flux limits calculated in all energy bands.

We masked bright sources from the 2FGL catalog (Nolan et al., 2012) using 0.°5 radius circles to minimize contributions from known point sources to the background. This mask radius is larger than the PSF of point sources for all but the lowest energies ($\sim$ 1 GeV) considered in our analysis. We tested various mask sizes and found that 0.°5 radius resulted in the smoothest background, although there is still some contamination to the background, up to 35% of the source signal. This contamination contributes randomly to the background and has little effect on the final flux estimates. The masked region was then statistically filled using the average local background, which we defined to be the annulus with inner and outer radii of 0.°7 and 0.°9, respectively. This average local background contains little contamination from the bright source itself ($<$ 8% of the source signal). For multiple bright sources, we masked from brightest to dimmest to minimize the contamination on adjacent masks. We then visually rejected clusters with poorly masked, bright 2FGL sources. We flattened each count map to the average exposure near the center of each cluster to make the effective exposure time uniform across the image. For any overlapping clusters (separation $<$ 2 Mpc) we excluded the more distant cluster. We also excluded one cluster where a bright source mask completely covers the cluster region. These procedures left us with 78 clusters (Figure 3.1) with the final stacked 0.8–100 GeV image shown in Figure 3.2. In addition to this map we also examined maps in which we sequentially stack the clusters in order of increasing background variance. This "stacking by variance" method provides an alternate approach for images with complex, multi-component backgrounds including bright sources, the Galactic

background, and the diffuse extragalactic background.

3.3 Results and Discussion

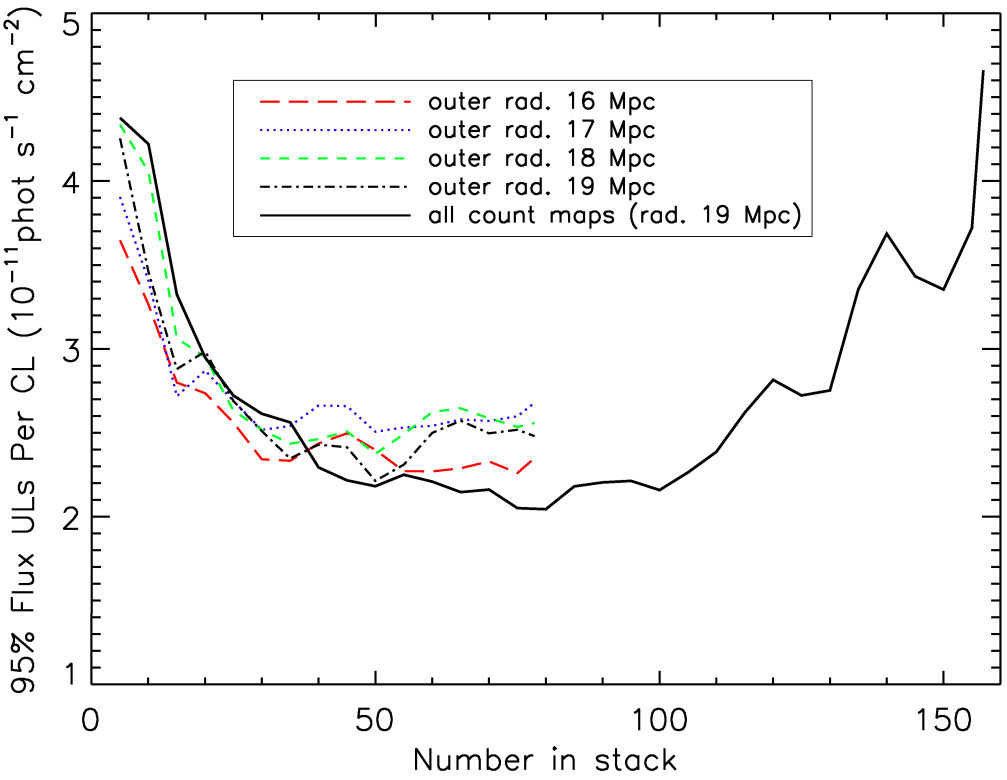


Figure 3.3: Photon flux upper limits $[0.8 - 100$ GeV$]$ per cluster as a function of the number of clusters included in the stack for different outer background radii (the inner radius is fixed at 3 Mpc). The stacks are ordered by the increasing variance of the cluster maps. The limits initially decline and then flatten. The black solid line indicates the stacking analysis that includes all count maps not in the Galactic plane, even those with poorly masked 2FGL sources. The trend increases after $N \sim 100$ suggesting that we correctly rejected images with large contamination.

Within our 2 Mpc source region of the final stack of 78 count maps (see Figure 3.2) we detect no excess γ-ray emission above the background. We find an aperture corrected 95% confidence upper limit of 2.48×10^{-11} photon cm^{-2} s^{-1} per cluster in the $0.8 - 100$ GeV band when we compare the source region to 500 random 2 Mpc regions in our standard background annulus (3–19 Mpc). This Monte-Carlo approach is more general in that it does not assume a Poisson background. The choice of the outer background radius has little effect (see Figure 3.3). Figure 3.3 also shows how the limits depend on the number of clusters as we stack them in order of increasing variance. There is an initial, rapid decline and then a flattening with a minimum at $N = 45$–55 clusters. Taking the median of the best upper limits from the stacking by variance method from the four different background apertures, we obtain the final upper limit of 2.32×10^{-11} photon cm^{-2} s^{-1} per cluster corresponding to a luminosity limit of 3.5×10^{44} phot s^{-1} in the $0.8 - 100$ GeV band given the median redshift of $z = 0.0758$. If we extend this to include clusters with poorly masked 2FGL sources (black, solid line in Figure 3.3), the number of clusters increases to 155 but the limits begin to significantly worsen as we reach $N > 100$ clusters. This indicates that our exclusion of these clusters was well-justified. We also constrain the γ-ray emission upper limits in a range of narrower energy bands and these limits are listed in Table 3.2.

Figure 3.4 compares our aperture corrected 95% confidence limits for the $0.8 - 100$ GeV band to the results of Ackermann et al. (2014) (1–200 GeV) and Huber et al. (2013) (1–300 GeV). We corrected for energy band differences by

modeling the photon flux as $dN/dE \propto (E/E_0)^{-2}$ (Pfrommer & Enßlin, 2004; Huber et al., 2013), but the corrections are very small ($\sim$ 5%). As seen in Figure 3.4, our new flux limits are an order of magnitude stronger than those for typical individual clusters and a factor of 2.1–1.2 improvement on the Huber et al. (2013) stacking limits of 2.8–4.9$\times 10^{-11}$ photon cm^{-2} s^{-1}. Because the Huber et al. (2013) sample is slightly closer, with a mean redshift of $z = 0.052$, this results in a factor two difference in z^2 compared to our sample. The mean mass of the Huber et al. (2013) clusters is also roughly a factor of two larger at $M_{500} = 5.6 \times 10^{14}\ M_\odot$, thus our mass-weighted luminosity limit is twice that of Huber et al. (2013), but for slightly smaller systems. In the 10–300 GeV band, our mass-weighted luminosity limit is also consistent with the constraint from Prokhorov & Churazov (2014).

Energy Range	Outer Bkg. Radius	Flux UL ($N \equiv 78$)	Lowest UL (N)
$0.8 - 100.0$	16 Mpc	23.5	22.6 ($N = 75$)
$13.0 - 300.0$	16 Mpc	1.32	1.24 ($N = 70$)
$0.8 - 1.6$	16 Mpc	20.9	17.2 ($N = 70$)
$1.6 - 3.2$	16 Mpc	8.06	7.87 ($N = 55$)
$3.2 - 6.3$	16 Mpc	3.35	3.13 ($N = 50$)
$6.3 - 13.0$	16 Mpc	1.88	1.83 ($N = 70$)
$13.0 - 25.0$	16 Mpc	1.01	1.01 ($N = 78$)
$25.0 - 50.0$	16 Mpc	0.591	0.569 ($N = 70$)
$50.0 - 100.0$	16 Mpc	0.419	0.415 ($N = 75$)
$100.0 - 170.0$	16 Mpc	0.322	0.293 ($N = 65$)
$170.0 - 300.0$	16 Mpc	0.278	0.236 ($N = 75$)

Table 3.2: Flux upper limits (UL) per cluster at 95% confidence in units of 10^{-12}photon cm^{-2} s^{-1}for various energy ranges. Shown here are our results with an outer background radius of 16 Mpc. First Column: The energy range considered. Second: Outer radius of the background annulus. Third: Upper limits for the complete stack of 78 clusters. Fourth: Lowest flux upper limits found for the number of clusters producing the best limit in the stacking by variance method.

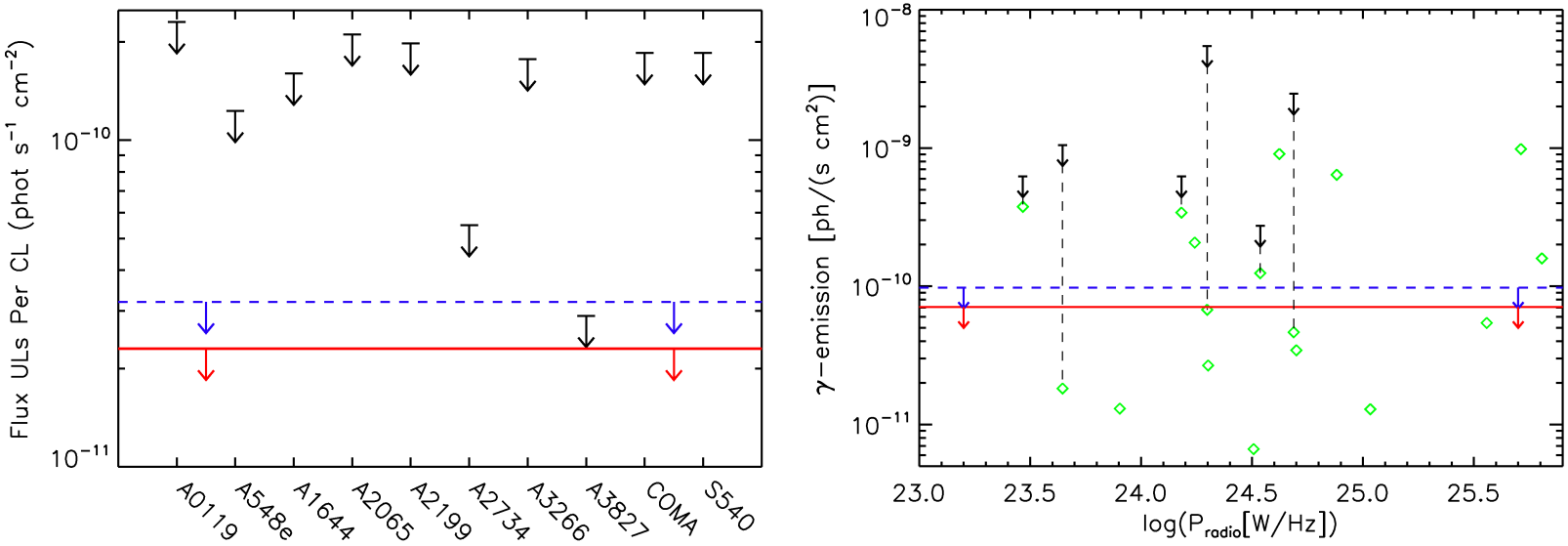


Figure 3.4: (Left) Flux limits from recent *Fermi*-LAT studies. The arrows are 10 clusters randomly selected from Ackermann et al. (2014). The lower red, solid line is our new upper limit, and the upper blue, dashed limit is from Huber et al. (2013). (Right) Model predictions for the 0.2–100 GeV flux for galaxy clusters with radio relics (green diamonds, from Vazza & Brüggen 2014) as compared to limits from individual cluster (black arrows, Ackermann et al. 2014) and the stacking limits from Huber et al. (2013, blue, dashed lines) and our analysis (red, solid line). We converted our 0.8–100 GeV limit to the 0.2–100 GeV band by scaling Vazza & Brüggen's (2014) conversion of Huber et al. (2013) limits that assumed a proton energy index of 2. Notice that the flux limit derived from our stacking method is less than that found by Huber et al. (2013) and therefore the comparison of our upper limit can emphasize the problem described by Vazza & Brüggen (2014), where upper limits on γ-ray flux obtained from stacking methods are lower than the predicted fluxes from nearby clusters.

Gamma-ray emission from galaxy clusters probes the non-thermal component of the intra-cluster gas. We can compare our flux limits to recent model predictions for the γ-ray emission from clusters by Huber et al. (2013), assuming that π^0 decay is the main γ-ray emission source. Since our mass weighted luminosity limit is twice that of Huber et al. (2013), we place upper limits of the CR-to-thermal energy ratio of 8% as scaled to Huber et al. (2013), corresponding to a CR-to-thermal pressure ratio of $P_{CR}/P_{Th} \simeq 4\%$. These results confirm the recent claims (Huber et al., 2013; Prokhorov & Churazov, 2014) that the CR energy and pressure contribute only marginally to the total energy and pressure of the intra-cluster gas. This reduces one uncertainty in estimating the hydrostatic cluster mass using thermal X-ray emission.

Moreover, γ-ray emission from galaxy clusters provides an additional window to constrain the details of cluster formation. Large-scale cosmological simulations have successfully predicted the mass function of galaxy clusters. However, we lack additional constraints to test the details of these models because we generally observe only the final stages of the merging history. Since the cooling time of the hadronic CR component is longer than a Hubble time, the hadronic CR component essentially accumulates in clusters (e.g., Berezinsky et al., 1997) so that the final γ-ray emission produced by the hadronic CRs depends on the full merger history. This should be compared to the CR electron-driven synchrotron radio emission – both are driven by the same shocks but the radio emission depends only on recent activity due to the short CR election life times. Since cluster merger models predict that all clusters have experienced similar shocks

during the assemblage history, the clusters with radio relics are considered an evolutionary stage of clusters because of the fast electron cooling time-scale.

Thus, we can compare the γ-ray flux constrained from a general cluster population with the radio flux from clusters with radio relics, because both the CR components are accelerated by the same shocks. While some model predicted γ-ray fluxes from clusters with radio halos are consistent with our limits (e.g., Kushnir et al. 2009), using a semi-analytical model, Vazza & Brüggen (2014) calculated the expected γ-ray emission from clusters with radio relics (arcs) that are evidence for shocks with Mach numbers of 2–4. Figure 3.4 (right) compares the predictions of Vazza & Brüggen (2014) (green diamonds) to the observed limits (arrows and horizontal lines), and, like Huber et al. (2013) our limits are well below the typical predictions. The problem can be more severe because there can be multiple mergers as a cluster forms. Several papers explored scenarios to resolve this discrepancy, including over-estimated Mach numbers from the radio data, lower energy deposition rates to the hadronic CR component than in standard diffuse shock acceleration models, and reacceleration of electrons (e.g., Vazza & Brüggen 2014; Brunetti & Jones 2014; Zandanel et al. 2014).

3.4 Acknowledgements

This chapter is reproduced by permission of the American Astronomical Society from the following publication: Griffin, R. D., X. Dai, & C. Kochanek (Nov 2014). "New Limits on Gamma-Ray Emission from Galaxy Clusters". In: ApJL 795, 21.

This research has made use of the publicly available *Fermi*-LAT data. We thank the anonymous referee and G. Brunetti, T. A. Thompson, D. Kushnir, B. Katz, F. Zandanel, and J. Han for helpful comments.

References

Abdo, A. A., Ackermann, M., Ajello, M., et al. 2009a, ApJ, 699, 31

—. 2009b, ApJ, 707, 55

—. 2010a, ApJ, 709, L152

—. 2010b, A&A, 523, A46

—. 2010c, A&A, 523, L2

—. 2010d, A&A, 512, A7

Abell, G. O. 1958, ApJS, 3, 211

Abell, G. O., Corwin, Jr., H. G., & Olowin, R. P. 1989, ApJS, 70, 1

Acero, F., Aharonian, F., Akhperjanian, A. G., et al. 2009, Science, 326, 1080

Acero, F., Ackermann, M., Ajello, M., et al. 2015, ApJS, 218, 23

Ackermann, M., Ajello, M., Allafort, A., et al. 2012, ApJ, 755, 164

Ackermann, M., Ajello, M., Albert, A., et al. 2014, ApJ, 787, 18

Adami, C., Mazure, A., Pierre, M., et al. 2011, A&A, 526, A18

Adelman-McCarthy, J. K., Agüeros, M. A., Allam, S. S., et al. 2007, ApJS, 172, 634

Aihara, H., Allende Prieto, C., An, D., et al. 2011, ApJS, 193, 29

Allen, S. W., Evrard, A. E., & Mantz, A. B. 2011, ARA&A, 49, 409

Amsler, C., Doser, M., Antonelli, M., et al. 2008, Physics Letters B, 667, 1

Anderson, M. E., Gaspari, M., White, S. D. M., Wang, W., & Dai, X. 2015, MNRAS, 449, 3806

Arnaud, K. A. 1996, in Astronomical Society of the Pacific Conference Series, Vol. 101, Astronomical Data Analysis Software and Systems V, ed. G. H. Jacoby & J. Barnes, 17

Ascaso, B., Wittman, D., & Dawson, W. 2014, MNRAS, 439, 1980

Assef, R. J., Kochanek, C. S., Brodwin, M., et al. 2010, ApJ, 713, 970

Bahcall, N. A. 1988, ARA&A, 26, 631

Barkhouse, W. A., Green, P. J., Vikhlinin, A., et al. 2006, ApJ, 645, 955

Bartelmann, M., & Schneider, P. 2001, Phys. Rep., 340, 291

Bell, E. F., McIntosh, D. H., Katz, N., & Weinberg, M. D. 2003, ApJS, 149, 289

Bell, E. F., Wolf, C., Meisenheimer, K., et al. 2004, ApJ, 608, 752

Berezinsky, V. S., Blasi, P., & Ptuskin, V. S. 1997, ApJ, 487, 529

Berrington, R. C., & Dermer, C. D. 2003, ApJ, 594, 709

Blackburne, J. A., & Kochanek, C. S. 2012, ApJ, 744, 76

Bleem, L. E., Stalder, B., de Haan, T., et al. 2015, ApJS, 216, 27

Blom, J. J., Paglione, T. A. D., & Carramiñana, A. 1999, ApJ, 516, 744

Böhringer, H., Voges, W., Huchra, J. P., et al. 2000, ApJS, 129, 435

Bourne, N., Dunne, L., Ivison, R. J., et al. 2011, MNRAS, 410, 1155

Bradač, M., Clowe, D., Gonzalez, A. H., et al. 2006, ApJ, 652, 937

Brandt, W. N., & Hasinger, G. 2005, ARA&A, 43, 827

Brodwin, M., Greer, C. H., Leitch, E. M., et al. 2015, ApJ, 806, 26

Brunetti, G., & Jones, T. W. 2014, International Journal of Modern Physics D, 23, 1430007

Burenin, R. A., Vikhlinin, A., Hornstrup, A., et al. 2007, ApJS, 172, 561

Carlstrom, J. E., Holder, G. P., & Reese, E. D. 2002, ARA&A, 40, 643

Carlstrom, J. E., Joy, M. K., Grego, L., et al. 2000, Physica Scripta Volume T, 85, 148

Cassano, R., Brunetti, G., Setti, G., Govoni, F., & Dolag, K. 2007, MNRAS, 378, 1565

Cillis, A. N., Torres, D. F., & Reimer, O. 2005, ApJ, 621, 139

Cooray, A., & Sheth, R. 2002, Phys. Rep., 372, 1

Dai, X. 2009, ApJ, 697, L68

Dai, X., Bregman, J. N., Kochanek, C. S., & Rasia, E. 2010, ApJ, 719, 119

Dai, X., Griffin, R. D., Kochanek, C. S., Nugent, J. M., & Bregman, J. N. 2015, ApJS, 218, 8

Dai, X., Kochanek, C. S., & Morgan, N. D. 2007, ApJ, 658, 917

D'Elia, V., Perri, M., Puccetti, S., et al. 2013, A&A, 551, A142

Donahue, M., Mack, J., Scharf, C., et al. 2001, ApJ, 552, L93

Dunne, L., & Eales, S. A. 2001, MNRAS, 327, 697

Eisenhardt, P. R. M., Brodwin, M., Gonzalez, A. H., et al. 2008, ApJ, 684, 905

Enßlin, T., Pfrommer, C., Miniati, F., & Subramanian, K. 2011, A&A, 527, A99

Evans, P. A., Osborne, J. P., Beardmore, A. P., et al. 2014, ApJS, 210, 8

Feretti, L., Giovannini, G., Govoni, F., & Murgia, M. 2012, A&A Rev., 20, 54

Finoguenov, A., Guzzo, L., Hasinger, G., et al. 2007, ApJS, 172, 182

Finoguenov, A., Tanaka, M., Cooper, M., et al. 2015, A&A, 576, A130

Gal, R. R., de Carvalho, R. R., Lopes, P. A. A., et al. 2003, AJ, 125, 2064

Gehrels, N., Chincarini, G., Giommi, P., et al. 2004, ApJ, 611, 1005

Giacconi, R., Kellogg, E., Gorenstein, P., Gursky, H., & Tananbaum, H. 1971, ApJ, 165, L27

Girardi, M., Giuricin, G., Mardirossian, F., Mezzetti, M., & Boschin, W. 1998, ApJ, 505, 74

Gitti, M., Brunetti, G., Feretti, L., & Setti, G. 2004, A&A, 417, 1

Gladders, M. D., & Yee, H. K. C. 2000, AJ, 120, 2148

—. 2005, ApJS, 157, 1

Gonzalez, A. H., Sivanandam, S., Zabludoff, A. I., & Zaritsky, D. 2013, ApJ, 778, 14

Griffin, R. D., Dai, X., & Kochanek, C. S. 2014, ApJ, 795, L21

Griffin, R. D., Dai, X., Kochanek, C. S., & Bregman, J. N. 2016, ApJS, 222, 13

Gursky, H., Kellogg, E., Murray, S., et al. 1971, ApJ, 167, L81

Guzzo, L., Schuecker, P., Böhringer, H., et al. 2009, A&A, 499, 357

Hao, J., McKay, T. A., Koester, B. P., et al. 2010, ApJS, 191, 254

Hasselfield, M., Hilton, M., Marriage, T. A., et al. 2013, J. Cosmology Astropart. Phys., 7, 008

Healey, S. E., Romani, R. W., Taylor, G. B., et al. 2007, ApJS, 171, 61

Heckman, T. M., Dahlem, M., Eales, S. A., Fabbiano, G., & Weaver, K. 1996, ApJ, 457, 616

Hennawi, J. F., Gladders, M. D., Oguri, M., et al. 2008, AJ, 135, 664

Hoeft, M., & Brüggen, M. 2007, MNRAS, 375, 77

Hoekstra, H. 2007, MNRAS, 379, 317

Hoekstra, H., & Jain, B. 2008, Annual Review of Nuclear and Particle Science, 58, 99

Huber, B., Tchernin, C., Eckert, D., et al. 2013, A&A, 560, A64

Isobe, T., Feigelson, E. D., Akritas, M. G., & Babu, G. J. 1990, ApJ, 364, 104

Iwasawa, K., Matt, G., Guainazzi, M., & Fabian, A. C. 2001, MNRAS, 326, 894

Jeltema, T. E., Kehayias, J., & Profumo, S. 2009, Phys. Rev. D, 80, 023005

Kaiser, N. 1991, ApJ, 383, 104

Kang, H., & Ryu, D. 2013, ApJ, 764, 95

Kawamata, R., Oguri, M., Ishigaki, M., Shimasaku, K., & Ouchi, M. 2016, ApJ, 819, 114

Kellogg, E., Gursky, H., Leong, C., et al. 1971, ApJ, 165, L49

Kennicutt, Jr., R. C. 1998, ARA&A, 36, 189

Kochanek, C. S., White, M., Huchra, J., et al. 2003, ApJ, 585, 161

Koester, B. P., McKay, T. A., Annis, J., et al. 2007, ApJ, 660, 239

Kravtsov, A. V., & Borgani, S. 2012, ARA&A, 50, 353

Lacki, B. C., Horiuchi, S., & Beacom, J. F. 2014, ApJ, 786, 40

Lacki, B. C., & Thompson, T. A. 2013, ApJ, 762, 29

Lacki, B. C., Thompson, T. A., & Quataert, E. 2010, ApJ, 717, 1

Lacki, B. C., Thompson, T. A., Quataert, E., Loeb, A., & Waxman, E. 2011, ApJ, 734, 107

Lin, Y.-T., & Mohr, J. J. 2004, ApJ, 617, 879

Liu, T., Tozzi, P., Tundo, E., et al. 2015, ApJS, 216, 28

Loeb, A., & Waxman, E. 2006, J. Cosmology Astropart. Phys., 5, 003

Lopes, P. A. A., de Carvalho, R. R., Capelato, H. V., et al. 2006, ApJ, 648, 209

Mantz, A., Allen, S. W., Rapetti, D., & Ebeling, H. 2010, MNRAS, 406, 1759

Marriage, T. A., Acquaviva, V., Ade, P. A. R., et al. 2011, ApJ, 737, 61

Mehrtens, N., Romer, A. K., Hilton, M., et al. 2012, MNRAS, 423, 1024

Melia, F. 2012, MNRAS, 422, 1418

Murase, K., Ahlers, M., & Lacki, B. C. 2013, Phys. Rev. D, 88, 121301

Navarro, J. F., Frenk, C. S., & White, S. D. M. 1995, MNRAS, 275, 720

Nilo Castellón, J. L., Alonso, M. V., García Lambas, D., et al. 2014, MNRAS, 437, 2607

Nolan, P. L., Abdo, A. A., Ackermann, M., et al. 2012, ApJS, 199, 31

Oguri, M., Bayliss, M. B., Dahle, H., et al. 2012, MNRAS, 420, 3213

Oguri, M., Takada, M., Okabe, N., & Smith, G. P. 2010, MNRAS, 405, 2215

Paglione, T. A. D., Marscher, A. P., Jackson, J. M., & Bertsch, D. L. 1996, ApJ, 460, 295

Pasquali, A., van den Bosch, F. C., Mo, H. J., Yang, X., & Somerville, R. 2009, MNRAS, 394, 38

Pavlidou, V., & Fields, B. D. 2001, ApJ, 558, 63

Peng, F.-K., Wang, X.-Y., Liu, R.-Y., Tang, Q.-W., & Wang, J.-F. 2016, ApJ, 821, L20

Pfrommer, C., & Enßlin, T. A. 2004, A&A, 413, 17

Pfrommer, C., Enßlin, T. A., Springel, V., Jubelgas, M., & Dolag, K. 2007, MNRAS, 378, 385

Piccinotti, G., Mushotzky, R. F., Boldt, E. A., et al. 1982, ApJ, 253, 485

Piffaretti, R., Arnaud, M., Pratt, G. W., Pointecouteau, E., & Melin, J.-B. 2011, A&A, 534, A109

Planck Collaboration, Ade, P. A. R., Aghanim, N., et al. 2011, A&A, 536, A8

—. 2014a, A&A, 571, A20

—. 2014b, A&A, 571, A29

Prokhorov, D. A., & Churazov, E. M. 2014, A&A, 567, A93

Puccetti, S., Capalbi, M., Giommi, P., et al. 2011, A&A, 528, A122

Rangwala, N., Maloney, P. R., Glenn, J., et al. 2011, ApJ, 743, 94

Refregier, A. 2003, ARA&A, 41, 645

Reichardt, C. L., Stalder, B., Bleem, L. E., et al. 2013a, ApJ, 763, 127

—. 2013b, ApJ, 763, 127

Rengarajan, T. N. 2005, ArXiv Astrophysics e-prints, astro-ph/0511156

Richard, J., Smith, G. P., Kneib, J.-P., et al. 2010, MNRAS, 404, 325

Rosati, P., Borgani, S., & Norman, C. 2002, ARA&A, 40, 539

Sanders, D. B., Mazzarella, J. M., Kim, D.-C., Surace, J. A., & Soifer, B. T. 2003, AJ, 126, 1607

Sarazin, C. L. 1986, Reviews of Modern Physics, 58, 1

Sargent, M. T., Schinnerer, E., Murphy, E., et al. 2010, ApJ, 714, L190

Schlickeiser, R. 2002, Cosmic Ray Astrophysics

Shan, H., Kneib, J.-P., Li, R., et al. 2015, ArXiv e-prints, arXiv:1502.00313

Skibba, R. A., van den Bosch, F. C., Yang, X., et al. 2011, MNRAS, 410, 417

Smith, H. E., Lonsdale, C. J., Lonsdale, C. J., & Diamond, P. J. 1998, ApJ, 493, L17

Stanford, S. A., Gonzalez, A. H., Brodwin, M., et al. 2014, ApJS, 213, 25

Stanford, S. A., Holden, B., Rosati, P., et al. 2002, AJ, 123, 619

Sunyaev, R. A., & Zeldovich, Y. B. 1970, Ap&SS, 7, 20

—. 1972, Comments on Astrophysics and Space Physics, 4, 173

Tang, Q.-W., Wang, X.-Y., & Tam, P.-H. T. 2014, ApJ, 794, 26

Thompson, T. A., Quataert, E., & Waxman, E. 2007, ApJ, 654, 219

Thompson, T. A., Quataert, E., Waxman, E., Murray, N., & Martin, C. L. 2006, ApJ, 645, 186

Tinker, J., Kravtsov, A. V., Klypin, A., et al. 2008, ApJ, 688, 709

Torres, D. F., Reimer, O., Domingo-Santamaría, E., & Digel, S. W. 2004, ApJ, 607, L99

Tundo, E., Moretti, A., Tozzi, P., et al. 2012, A&A, 547, A57

Umetsu, K., Zitrin, A., Gruen, D., et al. 2016, ApJ, 821, 116

Umetsu, K., Medezinski, E., Nonino, M., et al. 2014, ApJ, 795, 163

Valentinuzzi, T., Poggianti, B. M., Fasano, G., et al. 2011, A&A, 536, A34

van Breukelen, C., Clewley, L., Bonfield, D. G., et al. 2006, MNRAS, 373, L26

van den Bosch, F. C., Aquino, D., Yang, X., et al. 2008, MNRAS, 387, 79

van der Kruit, P. C. 1971, A&A, 15, 110

Vazza, F., & Brüggen, M. 2014, MNRAS, 437, 2291

Vazza, F., Brüggen, M., Wittor, D., et al. 2016, MNRAS, 459, 70

VERITAS Collaboration, Acciari, V. A., Aliu, E., et al. 2009, Nature, 462, 770

Vikhlinin, A., Burenin, R. A., Ebeling, H., et al. 2009, ApJ, 692, 1033

Voges, W., Aschenbach, B., Boller, T., et al. 1999, A&A, 349, 389

Voit, G. M. 2005, Reviews of Modern Physics, 77, 207

Völk, H. J., Aharonian, F. A., & Breitschwerdt, D. 1996, Space Sci. Rev., 75, 279

von der Linden, A., Best, P. N., Kauffmann, G., & White, S. D. M. 2007, MNRAS, 379, 867

von der Linden, A., Allen, M. T., Applegate, D. E., et al. 2014, MNRAS, 439, 2

Weinberg, D. H., Mortonson, M. J., Eisenstein, D. J., et al. 2013, Phys. Rep., 530, 87

Weinmann, S. M., van den Bosch, F. C., Yang, X., & Mo, H. J. 2006, MNRAS, 366, 2

Wen, Z. L., Han, J. L., & Liu, F. S. 2012, ApJS, 199, 34

Wittman, D., Dell'Antonio, I. P., Hughes, J. P., et al. 2006, ApJ, 643, 128

Yoast-Hull, T. M., Gallagher, J. S., & Zweibel, E. G. 2015, MNRAS, 453, 222

Yun, M. S., Reddy, N. A., & Condon, J. J. 2001, ApJ, 554, 803

Zandanel, F., & Ando, S. 2014, MNRAS, 440, 663

Zatloukal, M., Röser, H.-J., Wolf, C., Hippelein, H., & Falter, S. 2007, A&A, 474, L5

Zwicky, F. 1933, Helvetica Physica Acta, 6, 110

Appendix A

Constraining Gamma-Ray Emission from Luminous Infrared Galaxies

In this appendix, I present our *Fermi*-LAT analysis of luminous and ultraluminous galaxies. Here, we use an updated version of the method discussed in Chapter 3.

A.1 Introduction

Gamma-ray emission provides a sensitive probe of the cosmic ray content of star-forming galaxies. When cosmic ray protons collide with the dense ISM of star-forming galaxies, they produce secondary electron-positron pairs, neutrinos, and gamma-rays through pion production on a characteristic timescale $t_{\rm pp} \simeq 7 \times 10^7\,{\rm yr}\,n^{-1}$, where n is the gas density of the ISM in units of ${\rm cm}^{-3}$ (e.g., Schlickeiser 2002). For average ISM densities larger than $\sim 10 - 100\,{\rm cm}^{-3}$, $t_{\rm pp}$ may be sufficiently short that one expects most of the cosmic rays to interact with the ISM before escaping the host galaxy through diffusion, or via advection in a large-scale galactic wind (Loeb & Waxman, 2006). Assuming that cosmic rays are predominantly accelerated in supernovae, if the cosmic ray escape time is much longer than $t_{\rm pp}$, then one expects a one-to-one linear relation between the gamma-ray luminosity and the star formation rate, as measured by the far-infrared luminosity or GHz radio continuum (RC) luminosity (Thompson et al., 2007; Lacki et al., 2010, 2011).

The diffuse gamma-ray emission from star-forming galaxies and its contribution to the extragalactic diffuse gamma-ray background has been predicted by a number of authors (e.g., Paglione et al., 1996; Blom et al., 1999; Torres et al., 2004; Cillis et al., 2005; Thompson et al., 2007; Pavlidou & Fields, 2001). Observational breakthroughs occurred with the detections of nearby starburst galaxies M82 (VERITAS, VERITAS Collaboration et al., 2009) and NGC 253 (H.E.S.S., Acero et al., 2009) by Cherenkov telescopes and *Fermi* (Abdo et al., 2010a). Ackermann et al. (2012) further summarized the *Fermi* detections of diffuse gamma-ray emission from local group galaxies, including the Milky Way, M31, the LMC and SMC, and from nearby star-forming galaxies NGC 4945 and NGC 1068. Tang et al. (2014) observed a $\sim 5.5\sigma$ detection from the luminous infrared galaxy NGC 2146. Ackermann et al. (2012) also established empirical correlations between the diffuse gamma-ray emission and both the FIR or radio emission of star-forming galaxies, where the latter two continua are also tightly correlated (e.g., van der Kruit, 1971; Yun et al., 2001; Sargent et al., 2010; Bourne et al., 2011).

In this paper, we focus on *Fermi* observations of luminous (LIRGs; $10^{11} < L_{\rm IR}(8-1000\mu{\rm m})/L_{\odot} < 10^{12}$) and ultra-luminous IR galaxies (ULIRGs (LIRGs; $L_{\rm IR}(8-1000\mu{\rm m})/L_{\odot} > 10^{12}$), probing the highest luminosity regime. We assume a flat ΛCDM cosmology of $H_0 = 70$ km s^{-1}Mpc^{-1}, $\Omega_m = 0.3$, and $\Omega_\Lambda = 0.7$.

A.2 Analysis

For our galaxy sample, we use infrared bright ($L_{\rm IR}(8-1000\mu m) > 10^{11} L_{\odot}$) galaxies from the *Infrared Astronomical Satellite* (*IRAS*) Revised Bright Galaxy Sample (RBGS, Sanders et al. 2003). The RBGS contains all 629 extragalactic objects brighter than 5.24 Jy at 60 μm surveyed by the *IRAS*. These are the brightest extragalactic 60 μm sources (Sanders et al., 2003) and are ideal candidates for studying gamma-ray emission in star-forming galaxies. Most of the galaxies have low infrared luminosities $L_{\rm IR}(8 - 1000\mu m) < 10^{11} L_{\odot}$. Further excluding targets close to the Galactic plane ($|b| < 20^{\circ}$), where the Galactic gamma-ray background is high, our sample contains 135 galaxies with a range of redshifts from 0.0030 to 0.082, with a median redshift 0.022. In this sample, there are 123 LIRGs and 12 ULIRGs. As discussed later in this section, we use 82 of the total 135 galaxies by further excluding targets with high backgrounds.

Using 399 weeks ($\sim$ 7.7 years) of *Fermi*-LAT data, we obtain photon flux upper limits (ULs) from individual and stacked photon count maps of galaxy positions. We follow a similar method as described in Griffin et al. (2014), where we study *Fermi*-LAT count map stacks of galaxy clusters to obtain the lowest ULs to date. Here we summarize the method and discuss any changes and updates that are tailored to stack galaxies. For more details, see Griffin et al. (2014). In general, galaxies have much smaller angular sizes than nearby galaxy clusters, and considering the angular resolution of *Fermi*-LAT, most galaxies are unresolved in the gamma-ray regime. Therefore, we choose to use a fixed angular

radius to stack the data rather than a fixed physical radius as in Griffin et al. (2014). The corresponding background regions are in general smaller, and the number of contaminating background sources lower. We use PASS8 LAT source photons and determine good time intervals using the recommended expression `((DATA_QUAL==1) && (LAT_CONFIG==1))`. We use the recommended zenith angle cut of 90° to exclude gamma-rays from Earth's atmospheric limb.

For each count map, we exclude weeks with high background flaring activity, where the photon flux (phot cm^{-2} s^{-1}) is greater than 2σ above the mean flux. This removes the contribution to the background from variable gamma-ray sources (Griffin et al., 2014). We use 7 logarithmically spaced energy bins across the bandpass $0.8 - 100$ GeV. We use a pixel size of 0.°4 and count maps of 4° radii to estimate the background contribution. We tested other pixel radii; however they were either much lower than the resolution of the *Fermi*-LAT, or were too large, which results in a larger background, increasing the number of contaminated targets. The 4° count map radius was found to be optimal to encompass source and background regions. The lower energy bin PSFs (~ 1 GeV) are larger than the 0.°4 source radius, so we calculate an energy-dependent aperture flux correction to apply to flux limits calculated in all energy bands.

We first co-add the exposure and count maps in the time domain so that we have one count map and one exposure map for each galaxy position. We flatten each count map using the average exposure measured from the center so that the effective exposure time is uniform across each image. To minimize background contamination from known point sources, we mask bright sources from the 3FGL

catalog (Acero et al., 2015). We exclude any photons within 0.°5 of the source and populate this region with randomly placed photons using the average local background measured in the annulus with inner and outer radii 0.°7 to 0.°9, respectively. We visually rejected any count maps with residual contamination from poorly masked 3FGL sources. In general, these contaminating sources are nearby blazars or pulsars. Among the rejected cases are the previously detected LIRGs NGC 2146 and NGC 1068 (Tang et al., 2014; Ackermann et al., 2012). In our final sample, we have 82 galaxies where 7 are ULIRGs, including Arp 220 and Mrk 273. The other 75 are LIRGs. The positions of these galaxies and their 4° extent on the sky are shown in green in Figure A.1, while the rejected galaxies are shown in red.

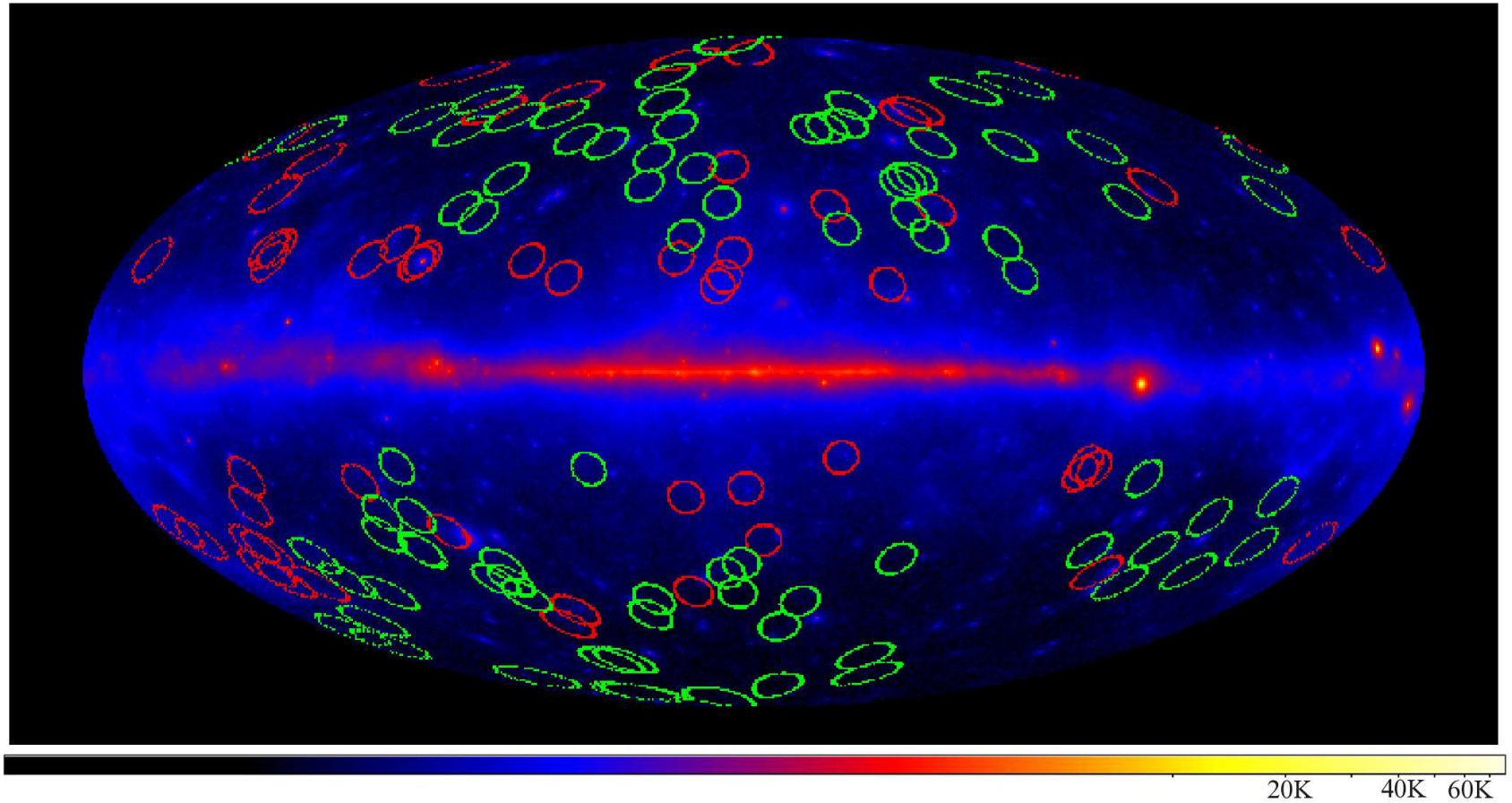


Figure A.1: All-sky gamma-ray photon count map, 135 ellipses indicate positions of *IRAS* galaxies used in this analysis and their 4° extents on the sky. The 82 green ellipses shown include Arp 220 and the 81 galaxies used in the final stacked image. Red ellipses are rejected sources due to background contamination.

A.3 Results and Discussion

Figure A.2 (left) shows the final stack of 81 photon count maps with a black central circle indicating the 0.°4 source region. We detect no excess gamma-ray source emission above the background and find an aperture corrected 95% confidence upper limit of 1.74×10^{-11} photon cm^{-2} s^{-1} per galaxy in the $0.8 - 100$ GeV energy band (excluding Arp 220). ULs are obtained using a fixed inner background radius of 1.°2 and outer background radii of 2.°4, 2.°8, 3.°2, and 3.°6, respectively. The UL of 1.74×10^{-11} photon cm^{-2} s^{-1} per galaxy is the median UL using the four background regions and is represented by the horizontal line in Figure A.3. We find that the choice of outer background radius has little impact on the UL, as shown in Figure A.3. We stack the count maps in order of background variance and as expected, as we add more photon count maps the flux ULs drop significantly and level out after ~ 50. Additionally, Figure A.3 shows the ULs obtained from the stack of 135 count maps, including the visually rejected point source contamination cases. This shows that we do not see improvement from including these count maps and that the choice to exclude these cases is valid. The sharp uptick at the right end of Figure A.3 is from the inclusion of 2 count maps that have the pulsar PSR J1836+5925 (e.g., Acero et al. 2015), providing strong contamination to the background. We also study the LIRG and ULIRG stacks separately. The LIRG photon flux UL we obtain is 1.73×10^{-11} photon cm^{-2} s^{-1} per galaxy and with a mean redshift of 0.023 for the 75 galaxies, and we obtain a corresponding luminosity limit of 1.30×10^{41}

ergs s^{-1} in the $0.8-100$ GeV energy band. The UL we obtain from stacking the 6 ULIRGs, excluding Arp 220, is 5.44×10^{-11} photon cm^{-2} s^{-1} per galaxy. With a mean redshift of 0.052, we obtain a corresponding luminosity limit of 2.19×10^{42} ergs s^{-1} in the $0.8 - 100$ GeV energy band.

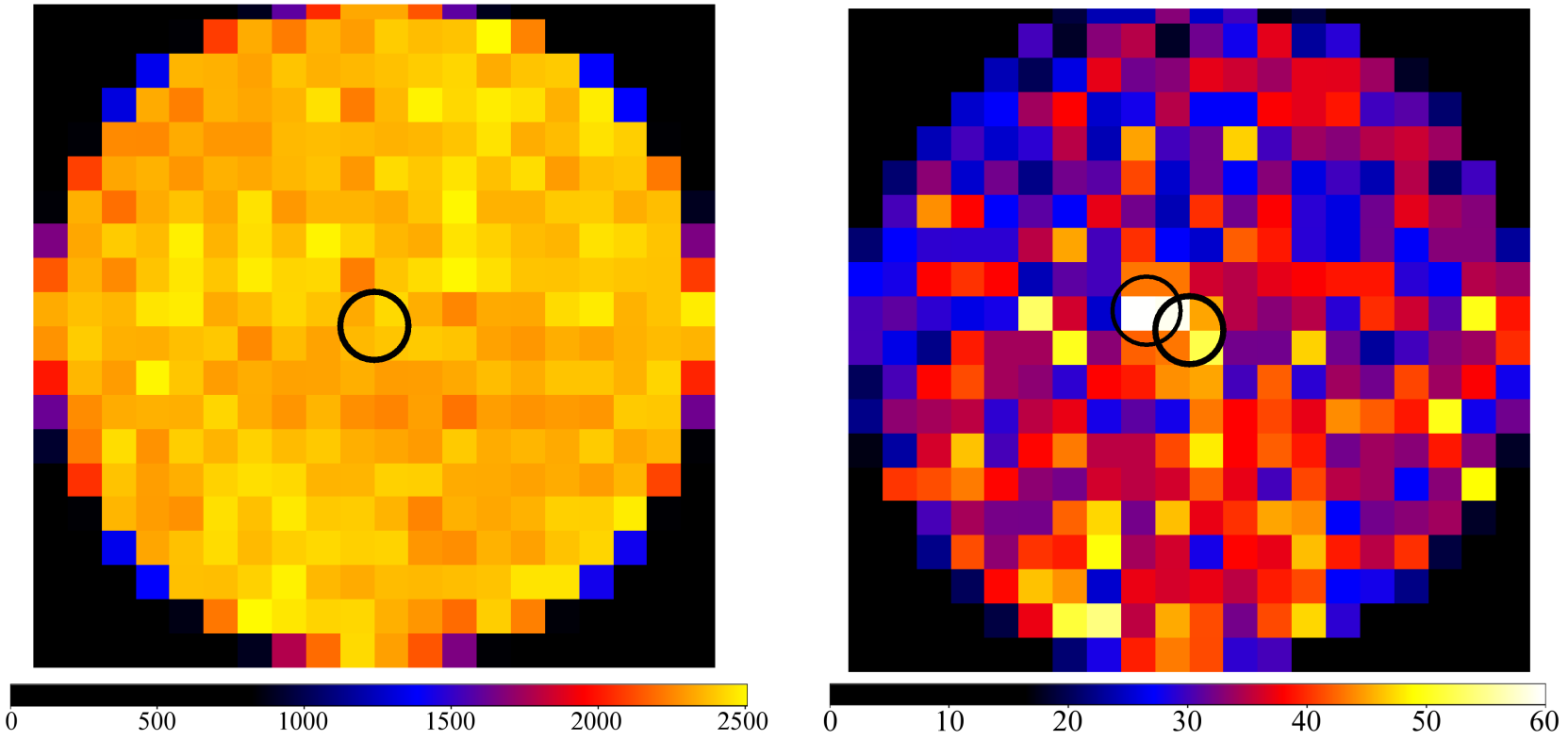


Figure A.2: Left: Final stacked photon count map of 81 *IRAS* galaxies. We exclude the detection of Arp 220 from this stack. Right: Photon count map of Arp 220 with 3.78σ source detection. The thinner black circle indicates the position of CRATES J153246 + 234400, the likely source of contamination. A binned likelihood analysis determined a TS value of 21.3 ($\sim 4.6\sigma$) for Arp 220. Both count maps include a black circle indicating the 0°.4 source region.

In addition to examining stacks of galaxy count maps, we study each galaxy individually. In all but one case, we do not detect any source significantly above the background. The one exception is Arp 220, the closest ULIRG to our galaxy, where we detect gamma-ray emission at 3.78σ significance above the local background in the $0.8 - 100$ GeV energy band. Excluding Arp 220, we find that the individual flux ULs for each galaxy in the entire sample range from 8.2×10^{-11} to 3.0×10^{-10} photon cm^{-2} s^{-1}. Of the 81 galaxies, we measure a median individual galaxy UL of 1.4×10^{-10} photon cm^{-2} s^{-1} and mean redshift of 0.026. We obtain a corresponding luminosity limit of 1.3×10^{42} ergs s^{-1} in the $0.8-100$ GeV energy band.

Arp 220 is a two galaxy merging system with extreme conditions, and has been studied extensively across multiple wavelengths (e.g., Smith et al., 1998; Heckman et al., 1996; Dunne & Eales, 2001; Rangwala et al., 2011; Lacki et al., 2011). The redshift of Arp 220 is $z = 0.018$, implying a distance of 77 Mpc. This ULIRG has previously not been detected in the gamma-ray regime and one of the galaxy nuclei might house a hidden AGN (e.g., Iwasawa et al., 2001; Rangwala et al., 2011). We detect a gamma-ray signal at the location of Arp 220 that is 3.78σ above the mean background level (Figure A.2, right), where we sample the mean background and its standard deviation by randomly drawing 500 regions of the same size as the source region in the background area. The off-center peak emission seen in Figure A.2 implies some contamination from a nearby source. This emission is not from a source in the 3FGL catalog (Acero et al., 2015). In their analysis of Arp 220, Tang et al. (2014) suggest CRATES J153246 + 234400,

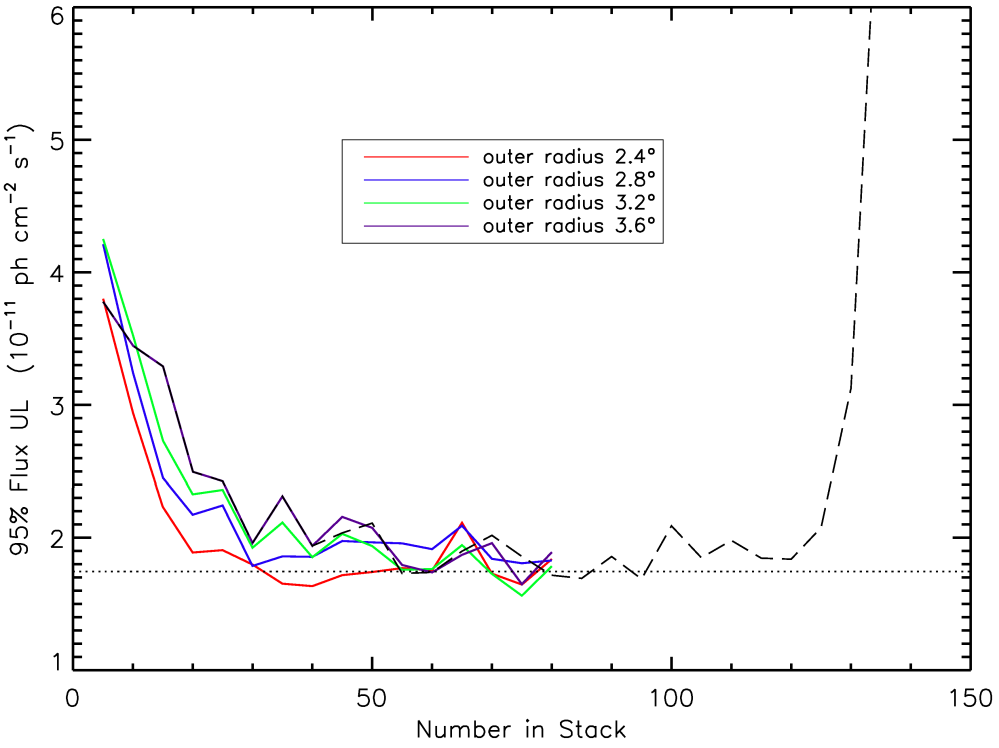


Figure A.3: Photon flux upper limits versus stack size, sorted by background variance. The solid lines represent the four different outer radii used for the 81 count maps in the final stack (we exclude the detection of Arp 220). As the stack size increases, the flux ULs decrease and flatten as expected. The dashed line represents the stacking analysis of the 135 count maps, including those with background contaminations from 3FGL sources, namely blazars and pulsars. The horizontal dotted line is the median flux of the final 81 count maps stack: 1.74×10^{-11} phot cm^{-2} s^{-1}.

a flat-spectrum radio quasar (FSRQ, Healey et al. 2007) as the likely candidate of the contamination. The position of this source is located 0.55° from Arp 220 and aligns with the peak emission, as indicated in Figure A.2 with the thinner black circle. We examine smaller energy bins to determine if the detection of Arp 220 is significant despite the contamination. We use the energy dependent mean PSFs of each sub energy bin as a source radius. We mask the overlapping area from the contaminating source and fill in that mask with a proportional count of photons from the unaffected area of the Arp 220 signal. In so doing, we find that the first energy bin with energies [0.8, 1.6] GeV is contaminated but the remaining energy bands together [1.6, 100] GeV provide a 3.03σ signal above the background. Thus, it seems there is a significant signal from Arp 220 and we analyze the system more closely.

We perform a binned likelihood analysis of Arp 220 using the recommended method from the Fermi Science Support Center[1]. We use photons with energies in the bandpass 0.8–100 GeV, using an ROI of radius 10° with Arp 220 at the center and we model the emission from all 3FGL sources within 15° as point sources. We include two additional point sources, for Arp 220 and CRATES J153246+234400, modeled with power-law spectrums: $dN/dE = N_\circ(E/E_\circ)^{-\Gamma_{ph}}$, where Γ_{ph} is the photon index. We model the Galactic and extragalactic backgrounds using the most up-to-date versions: gll_psc_v16.fit and iso_P8R2_SOURCE_V6_v06.txt. For CRATES J153246 + 234400, we measure a TS value, photon index, and photon flux of 20.3 (4.5σ), 3.472 ± 1.23 and $2.66 \pm 0.78 \times 10^{-10}$, respectively. For Arp

[1]FSSC, fermi.gsfc.nasa.gov/ssc/

220, we measure a TS value of 21.3 (4.6σ) with a photon index of 2.23 ± 0.46 and photon flux $2.43 \pm 0.90 \times 10^{-10}$ photon cm^{-2} s^{-1} in the energy band [0.8, 100] GeV. Using the measured photon index, we find the luminosity of Arp 220 to be $8.22 \pm 3.0 \times 10^{41}$ ergs s^{-1}. Independent of our analysis, Peng et al. (2016) also report a gamma-ray detection of Arp 220 ($\sim 6.3\sigma, \Gamma_{ph} = 2.35 \pm 0.16$) in the energy band [0.2, 100] GeV, reported concurrently with this work. Their gamma-ray luminosity of $L_{0.1-100\mathrm{GeV}} = 1.78 \pm 0.30 \times 10^{42}$ ergs s^{-1} is consistent with our value of $L_{0.1-100\mathrm{GeV}} = 1.57 \pm 0.58 \times 10^{42}$ ergs s^{-1}.

The detection of Arp 220 is largely in agreement with previous theoretical models, including explicitly proton calorimetric estimates (Thompson et al., 2007), and more detailed treatments (e.g., Torres et al., 2004; Lacki et al., 2010, 2011; Lacki & Thompson, 2013; Yoast-Hull et al., 2015). The implications of the detection of Arp 220 in the gamma-ray regime, with a luminosity compatible with the calorimetric limit, have been described extensively by Lacki et al. (2011). Here, we briefly summarize. The high gamma-ray luminosity implies (1) a low equilibrium energy density for cosmic rays with respect to the energy density required for hydrostatic equilibrium, (2) secondary electron/positron pairs from pion production likely dominate production of the observed GHz radio continuum (Torres et al. 2004, Rengarajan 2005, see eq. 19 of Lacki et al. 2011), (3) relativistic bremsstrahlung and ionization losses flatten the continuum synchrotron spectrum (see Thompson et al. 2006), potentially providing evidence for the "high gas surface density" conspiracy for the FIR-radio correlation described in Lacki et al. (2010), and finally (4) star-forming galaxies contribute to

the diffuse gamma-ray and neutrino backgrounds (e.g., Pavlidou & Fields, 2001; Loeb & Waxman, 2006; Thompson et al., 2007; Lacki et al., 2014; Murase et al., 2013). Gamma-rays with $>$TeV energies are expected to be attenuated (Torres et al., 2004; Lacki & Thompson, 2013; Yoast-Hull et al., 2015), producing high-energy electron/positron pairs that may contribute to the observed diffuse X-ray emission via synchrotron radiation (Lacki & Thompson, 2013).

Ackermann et al. (2012) examined correlations in star-forming galaxies between the gamma-ray luminosity and other tracers of star formation histories. Total IR luminosity (8–1000 μm) is one such tracer, as the ultraviolet light from massive stars is absorbed by dust and re-radiated as infrared (e.g., Kennicutt 1998). Another tracer is the RC luminosity that originates from CR electrons and positrons producing synchrotron radiation. With our gamma-ray flux measurements of Arp 220, we can extend the correlation to the high luminosity end. Figure A.4 compares gamma-ray luminosities to these other tracers of star formation history, RC luminosity on the left and total IR luminosity on the right. In the calorimetric limit a power-law relationship is expected in either case, represented by the dashed lines (see Ackermann et al. 2012 for details). We include *Fermi*-LAT detections from the local group (Abdo et al., 2010c,b,d), the four detections by Ackermann et al. (2012), and our detection of Arp 220. Additionally, we include our upper limits from the LIRG and ULIRG stacks. For this plot, we convert our luminosities found in the [0.8 – 100] GeV bandpass to the luminosity band of [0.1 – 100] GeV used by Ackermann et al. (2012), assuming a power-law spectral shape, $dN/dE = N_\circ (E/E_\circ)^{-\Gamma_{ph}}$ and $\Gamma_{ph} = 2$ (e.g., Lacki et al. 2011). For

Arp 220, we use the measured photon index of 2.23. Furthermore, we convert the Ackermann et al. (2012) luminosities from their adopted Hubble constant of 75 km s^{-1} Mpc^{-1} to our adopted value of 70 km s^{-1} Mpc^{-1}. The measurements from this paper are shown in red in Figure A.4. We fit the detections using χ^2 minimization assuming a simple power-law relation. The gamma-ray–IR luminosity correlation is described by the best fit line:

$$\log L_{0.1-100\mathrm{GeV}} = (1.25 \pm 0.03) \times \log L_{8-1000\mu\mathrm{m}} + (26.7 \pm 0.29), \tag{A.1}$$

as well as the gamma-ray–RC luminosity correlation with

$$\log L_{0.1-100\mathrm{GeV}} = (1.22 \pm 0.03) \times \log L_{1.4\mathrm{GHz}} + (13.3 \pm 0.58). \tag{A.2}$$

Our Arp 220 detection lies right on the line for the gamma-ray-FIR fit and above the gamma-ray-RC fit but within the uncertainties.

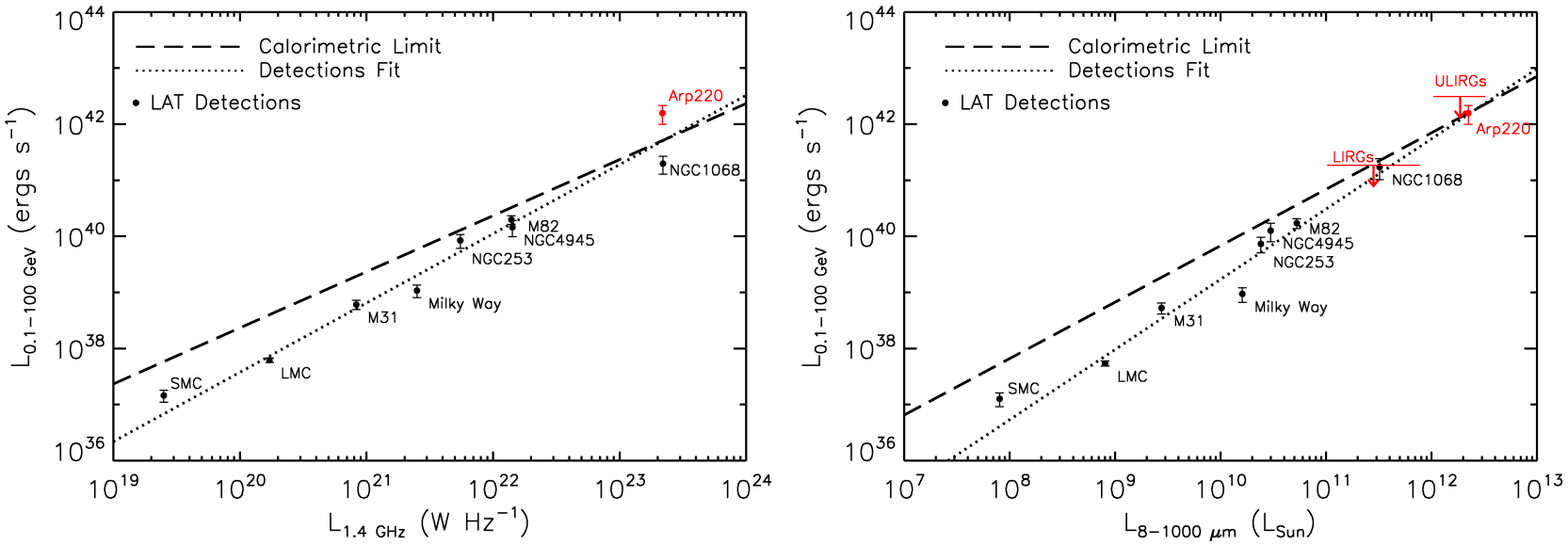


Figure A.4: Gamma-ray luminosity versus radio continuum luminosity (left) and infrared luminosity (right), based off Figure 4 from Ackermann et al. (2012). The dashed line is the expected gamma-ray luminosity in the calorimetric limit (Thompson et al., 2007; Lacki et al., 2011; Ackermann et al., 2012). The points represent *Fermi*-LAT detections, where the most luminous is our detection of Arp 220, the rest are from Ackermann et al. (2012). The dotted line is the best fit to the detections using a χ^2 best fit. Our Arp 220 detection agrees well with the expected signal based off of previous *Fermi*-LAT detections. The red arrows indicates our upper limits determined by the stack of 75 LIRGs and the stack of 6 ULIRGs (excluding the detection of Arp 220). The red horizontal stripes indicate the infrared luminosity bins used in the stacks.

As *Fermi*-LAT collects more data, we expect to see more detections of nearby ULIRGs and LIRGs. Our ULs from the LIRG and ULIRG stacks are approaching the power-law fit from the detections. If we treat this fit as a detection threshold, we would only need to improve our LIRG UL by a factor of two and our ULIRG UL by a factor of three to cross this threshold.

In this Letter, we have applied the method of Griffin et al. (2014) of making and stacking *Fermi*-LAT count maps to study LIRGs and ULIRGs. We present upper limits as well as a 4.6σ detection of the previously undetected Arp 220, the closest ULIRG. We compare these to similar studies, namely those presented in Ackermann et al. (2012). Our results place further constraints on expected gamma-ray emission from these star-forming galaxies in the more energetic regime. We show that our upper limits are close to the current detection limit of *Fermi*-LAT and expect to see more detections in the next few years.

A.4 Acknowledgements

This chapter is reproduced by permission of the American Astronomical Society from the following publication: Griffin, R. D., X. Dai, & T. A. Thompson (May 2016). "Constraining Gamma-Ray Emission from Luminous Infrared Galaxies with *Fermi*-LAT; Tentative Detection of Arp 220". In: ApJL 823, 17.

This research has made use of the publicly available *Fermi*-LAT data. We thank the anonymous referee for helpful comments. We acknowledge the financial support from the NASA ADAP programs NNX11AD09G, NNX15AF04G, and

NSF grant AST−1413056. TAT is supported by NSF Grant #1516967. TAT thanks Brian Lacki, Eliot Quataert, and Eli Waxman for discussions and collaboration.